
Magnetically actuated microrobots for polishing at unreachable sites

by
Sokratis Dimitriadis

A dissertation submitted to

The University of Sheffield



in partial fulfillment of the requirements for the degree of

Master of Philosophy

8th October 2023

Sokratis Dimitriadis

Magnetically actuated microrobots for polishing at unreachable sites

MPhil Dissertation, 8th October 2023

Supervisors: Dr Shuhei Miyashita (The University of Sheffield, UK)
Dr Anton Selivanov (The University of Sheffield, UK)
Dr Guo Zhan Lum (Nanyang Technological University, Singapore)
Dr Chun Wai Kum (A*STAR, Singapore)
Dr Kai Liang Tan (A*STAR, Singapore)

The University of Sheffield

Department of Automatic Control and Systems Engineering

Amy Johnson Building

Portobello Street

Sheffield, S1 3JD

A*STAR

Advanced Remanufacturing and Technology Centre

JTC CleanTech Two Block A

3 Cleantech Loop

Singapore, 637143

*One of the basic rules of
the universe is that
nothing is perfect.
Perfection simply doesn't
exist.
Without imperfection,
neither you nor I would
exist*

Stephen Hawking

To my beloved family

Acknowledgement

To the University of Sheffield (UK) and A*STAR (Singapore) for funding my research. To my supervisors, my colleagues and friends for their precious help, unbiased criticism and unconditional support. Special thanks to Alfred Wilmot for 3D-printing and assembling the lapper-bot platform, and helping us with the experiments, and to Quentin Lahondes for the trainings and help provided in the clean room facility of the Kroto Research Institute.

Declaration

I, Sokratis Dimitriadis, declare that the work presented in this thesis is my own. All material in this thesis which is not of my own work, has been properly accredited and referenced.

Sheffield, 8th October 2023

Sokratis Dimitriadis

Abstract

Nowadays, automotive and aerospace industry can produce more and more abstract geometries that offer special functionalities during use. Complex parts which are being produced with advanced additive manufacturing technologies need to be polished internally to obtain the surface roughness that industrial applications require. Post finishing processes are required to reduce their internal surface roughness, from around $10\mu\text{m}$ to $1\mu\text{m}$ to provide the desired performance during use as demands keep rising. Conventional technologies are being used to deal with accessibility and surface quality problems by accessing products that require further finishing on the inside. However, surface internal morphologies (e.g. turns, multiple passages of varying diameter) potentially lead to overpolished, underpolished or even areas of millimetre scale that are not polished at all.

In this research, we have designed, fabricated and tested a polishing system for removing dried correction fluid from acrylic plates. This system is comprised of two magnetically coupled plastic discs, one for removing material and an another one to actuate and transmit torque to the former one. We evaluated the performance of our methods in two ways, by using a computer vision algorithm method and by weighing the polished parts before and after the process. The results show the amount of unwanted material that has been removed from the surface during the experimental trials. The average angular velocity of the rotating disc was $\omega = 16.5\text{rad/s}$ and the shear stress produced at its circumference was estimated to be 45.5N/m^2 .

Moreover, we have developed another polishing method using untethered magnetically actuated microrobots of $\varnothing 3\text{mm}$ diameter and 1mm thickness able to deal with accessibility issues that rise in the application fields. Our soft microrobots were designed and fabricated with SU-8 photolithography and soft-lithographic technologies, including a novel fabrication

method that bonds abrasives for polishing, and magnetic particles for remote actuation. Our microrobots performance was experimentally evaluated with results showing that they can pitch inside a structure with a speed of 9 mm/s and a yaw rate of 10 rad/s. Finally, we propose a novel 1D point-to-point localisation method using vibration sensors to navigate the microrobots inside potential subject structures for internal surface polishing. The results shown that the vibration sensors can sense subjects vibrating on them showing a potential for tracking their location during polishing internal surfaces.

Contents

Chapter 1

Introduction	1
1.1 Related work	3
1.2 Challenges	9
1.3 Aims and objectives	10
1.4 Research Contributions	12
1.5 Dissertation outline	12

Chapter 2

Remote Magnetically-directed lapper-bot	13
2.1 Introduction	15
2.2 Methods	15
2.2.1 Remotely-actuated polishing with permanent bar magnets ...	16
2.2.2 Magnetic actuation of lapper	18
2.2.3 Direct magnetic coupling polishing method	20
2.2.4 Indirect magnetic coupling polishing method	22
2.2.5 Design and fabrication	22
2.2.6 Shear stress and torque analysis	23
2.3 Material removal analysis	26
2.3.1 Weighing polymer plates method	26

2.3.2	Digital image processing methods	26
2.4	Results	28
2.4.1	Shear stress estimation results	28
2.4.2	Weighing polymer plates results	28
2.4.3	OpenCV data analysis results	30
2.5	Discussion	30
2.6	Conclusion	33

Chapter 3

Magnetic field-driven polishing microrobots 35

3.1	Introduction	36
3.2	Design and microfabrication methods	36
3.2.1	SU-8 photolithography	36
3.2.2	Soft-lithography	42
3.2.3	Abrasive-bonded magnetised soft-repliche fabrication	46
3.3	Discussion	47
3.4	Conclusion	49

Chapter 4

Remote actuation and localisation methods 51

4.1	Introduction	52
4.2	Magnetic actuation with electromagnetic coil system	53
4.3	Point-to-point localisation method using vibration sensors	55
4.4	Results	58
4.5	Discussion	66
4.6	Conclusion	66

Chapter 5

Discussions and future work 69

5.1	Discussions	70
5.1.1	Magnetically actuated lapper	70

5.1.2	Polishing microrobots	71
5.1.3	Localisation method	74
5.2	Future work	76

Chapter 6

Conclusion	77
-------------------------	-----------

References

References	79
-------------------------	-----------

References

List of Figures	90
------------------------------	-----------

References

List of Tables	91
-----------------------------	-----------

References

Matlab Codes	95
---------------------------	-----------

Introduction

” *The gem cannot be polished without friction nor man without trials.*

– Confucius –

1.1	Related work	3
1.2	Challenges	9
1.3	Aims and objectives	10
1.4	Research Contributions.	12
1.5	Dissertation outline	12

Grinding and machining are processes that we, humans as a species, have been using for thousands of years to provide the proper shape, functionality, and texture to objects we use or want to use. Polishing and finishing are processes that differ from grinding and machining in terms of their major output criteria. Grinding and machining share the same output criteria, which are the material removal (MR) and/or the material removal rate (MRR). Polishing and finishing have surface roughness as the major output criterion and this is the basic reason that such processes require more delicate/precise ways, so to obtain the desired results. Based on the field of application and the available means of each era, we always used to apply material removing processes during our everyday life. Some common examples through the ages are the sharpening of tools to keep them functional, kitchenware and jewelry finishing to increase their price in markets, preserve the furniture smoothness and quality, and many more. Specifically, we can mention grinding processes during the European Bronze Age used by immigrants in Britain (Beakers) back in the third millennium BC and made them be renowned in history for their pottery and the variety of applications in their daily life [1-3]. Archaeologists also recorded a huge contribution in stone/marble carving and sculpturing in Egypt and India the same era [4, 5]. A monumental example of a series of size reduction processes during the Greek Classical period (480-323 BC) is the Parthenon (Fig. 1.1) and its sculptures, which marked the dawning of the Western tradition of sculpture [6]. These examples are only a few indications that material removing and size reduction processes played an important role in human's life since ancient times.



Figure 1.1: Split view of Parthenon showing its present and ancient structure. Snapshot was taken from an interactive photo at <https://www.visionpubl.com/en/cities/athens/parthenon-facts-history/>

In modern age, many of the above problems ceased to exist and new ones took their place. Moreover, there were faster and/or cost-effective ways to solve remaining ones, such as to obtain a desired result for everyday life objects. After the industrial age and during last century, the development in automobile industry changed the global research directions and polishing became a necessary process to various fields. Also, since 1961, industrial robots have been introduced to this area and sometimes even human intervention can be avoided

through automated/preprogrammed procedures [7].

Recently, due to new and upcoming advanced manufacturing techniques, sophisticated structures of complex geometries can be produced, but also new drawbacks, difficulties and necessities have arisen. In particular, additive manufacturing technologies nowadays offer one-step fabrication, which reduces the need for assembling components to build the final structure. Also, various combinations of materials can be used during fabrication to obtain specific characteristics of the surface (strain, hardness, corrosion resistance, etc) [8]. However, structures produced with one-step fabrication technologies do not have the desired surface roughness, and they do not meet the requirements of automotive industry [9]. Also, existing cavities at the microscale can make structures vulnerable to corrosion or affect their performance during operation. Since the demands in industry and market increase, researchers try to develop new methods/technologies to deal with the current limitations.

1.1 Related work

Robotics and automation play a really crucial role in industrial applications and research interest in our era. Usually, a device's autonomy in the applied field and its optimum remote actuation during operation are aspects that researchers seek to successfully achieve in every approach [10]. Polishing materials is an area of research for many scientists even out of the field of Material Engineering/Science due to recent higher demands in industry. Advanced Manufacturing technologies still experience some limitations, like the built surface's poor quality or high surface roughness. For instance, Additive Manufacturing technologies like Selective Laser Melting (SLM) build the structure layer after layer resulting in irregularities between them. The built surface's morphology (surface roughness and geometry) obtained after an Additive Manufacturing process, affects its quality, resistance to corrosion, final performance, and usability, so effort is put on improving existing methods or developing new ones for (post-)processing materials and structures [11]. In this section, we present the most relevant contributions in the fields involved in this project, in order to point out the currently available tools, materials, methods, in this research area, along with the existing challenges and drawbacks, and how robotics can be applied to deal with them.

In metallurgy, techniques for welding even dissimilar metals had arisen, due to the high demands in modern industrial engineering fields. Kim and Kil mention friction stir spot welding as a technique for welding metals such as Aluminium and Magnesium [12]. In terms of manufacturing, various existing metal additive manufacturing (AM) technologies deal with the above problem by fusing powders and using one-step fabrication process. The American Society for Testing and Materials (ASTM) established a classification for all the AM processes

into seven categories [13], although Flynn et al. also considered Cold Spraying in their review paper [14]. They point out that among these categories, directed energy deposition and powder bed fusion (PBF) processes are widely used in industry, with selective laser melting (SLM) being the most popular for manufacturing biomaterial metal products at the moment [15]. Guo et al. point out that this advanced manufacturing technology can provide built structures of a complex geometry without the need of an assembling phase of smaller components. However, there is still the problem of the built structures' surface roughness and its insufficiency for specific industrial applications [16].

Various size reduction techniques have been developed during last century and some of them existed since ancient times, but they have been improved in many ways due to the industrial revolution. The conventional ones that are commonly used combined with abrasives currently, are belt grinding, buffing, lapping, sandblasting, and vibratory finishing. Friction and force models that govern machining, along with the general terms used in the field of machining materials and their differences are described in more detail by Marinescu, Rowe et al. in [17] and [18], respectively. A wide class of advanced machining (and polymer-assisted) processes that are being mostly used in industry is Abrasive flow machining/finishing (AFM/AFF). In this project we mainly focus on internal surface finishing, because there is a high research interest and an abundance of challenges, that are being explained in detail later in this Chapter. Currently the main existing classes of finishing techniques applied to internal surfaces are the following:

- Abrasive flow machining/finishing (AFM/F)
- Fluidised bed machining (FBM)[19]
- Fluid jet machining (FJM)
- Electrolytic and chemical polishing (ECP) [20]
- Internal cylindrical grinding (ICG)
- Magnetic abrasive finishing (MAF)
- Variants of the above

Table 1.1 summarises the advantages and disadvantages of these categories and mentions the categories that have each one of them. Principles of AFM, MAF and FBM processes and their variants are mainly discussed by Tan et al. in their review paper [21], while pointing out that the challenge of polishing unreachable areas of complex geometries produced with additive manufacturing technologies still remains. Developed technologies of the machining

Table 1.1: Advantages and disadvantages of finishing categories

Method	Advantages	Disadvantages
Abrasive Flow Finishing	high precision, deburring, uniform surface finish, selective material removal	equipment complexity, contamination of parts with abrasives
Fluidized Bed Machining	high precision, deburring, uniform surface finish, selective material removal	equipment complexity, contamination of parts with abrasives, process control
Fluid Jet Machining	high precision, uniform surface finish, selective material removal reduced tool wear	surface damage risk
Electrolytic and Chemical Polishing	high precision, deburring, uniform surface finish, selective material removal	equipment complexity, process control
Internal Cylindrical Grinding	high precision, deburring, uniform surface finish, selective material removal	equipment complexity, limited adaptability to certain geometries
Magnetic Abrasive Finishing	high precision, deburring, uniform surface finish, selective material removal	equipment complexity, surface damage risk, contamination of parts with abrasives, process control

method named High Energy Fluid Jet Machining (HEFJet-Mach) and its aspects were summarised by Axinte et al. [22]. Wetting morphologies on microstructured grooves with varying cross-sectional area were studied and classified by Seeman et al. in [23].

Superalloys are metal compositions that are highly preferable in automotive industry due to some of their characteristics. For instance, Inconel 718 is an alloy composed of austenitic nickel (50-55%) and chromium (17-21%), and it is known for its high-strength, and resistance to corrosion and extreme environmental conditions (high temperature/pressure) [24, 25]. Kaplonek et al. in [26] demonstrate the process of internal cylindrical grinding using Inconel alloy 600 as the application's workpiece material and Nadolny et al. examined how the glass-crystalline bond can affect the grinding wheel during material removing process [27]. Song et al. used a magneto-rheological (MR) AFF technique for polishing Titanium-alloy tube in [28], by combining linear motion of the polishing head and rotational motion of the tube. Guo et al. describe the effectiveness of their approach using vibration-assisted magnetic abrasive polishing (VAMAP) in [29]. Later on, they developed another magnetic abrasive finishing (MAF) technique using a rotating workpiece of Inconel 718 attached on

actuator, and vibrating magnets to produce reciprocal motion of the magnetic abrasives on the inside [16]. In particular, they used magnetic abrasives in a double-layered tube, with a cylindrical magnet in the inner tube and two bar magnets outside the outer one. In this way, they also created a rotational motion, along with a vibrational one, of the abrasives in the space between the two layers (inside the outer tube and outside the inner tube). Their results shown that the material removal is proportional to the rotation speed of the workpiece, obtaining $70\mu m$ at $10.5rad/s$, which was their highest speed. Smaller surface roughness ($0.45\mu m$) could be obtained when the speed of rotation dropped to $3.14rad/s$, but it was tripled when the speed further dropped to $1rad/s$.

As it is stated in Section 1.2, most of the currently-used techniques for finishing internal surfaces have many limitations. Zhang et al. point out that MAF seems to be the most promising among the popular ones, although the pressure drop, the duration and the geometrical complexity are the biggest obstacles/limitations to these methods [30]. Even MAF which is excessively and widely used fails when it comes to variations in polished structures' geometry and results usually include over-polished turns/bendings or non/under-polished corners/sides. In their approach, they used a spherical magnet (of two types) inside a tube and four bar magnets to actuate it from the outside. They demonstrated the performance of this polishing method with and without the use of magnetic abrasive powders (MAP)(iron and aluminum) and slurry (diamond, silicon carbide, and water). Using a profilometer, they measured the roughness of the polished surface and compared their methods based on the use of MAPs and slurries. The results show that the use of silicon carbide (SiC) as slurry, along with the use of MAPs has an increased material removal rate (MRR) in comparison with the use of diamond (with MAPs) or even water. The best surface roughness they obtained was $0.053\mu m$, using $3\mu m$ diamond as slurry, but without using any MAPs. The presented results indicate that magnetic assisted finishing techniques seem to be really effective in polishing internal surfaces, although the limited number of materials that can be processed is a significant drawback [31, 32]. Apart from this, the duration of the processes followed to obtain the shown results was at least 60 minutes. In their recent publication, Zhang et al. achieved a polishing approach with MRR of $15\mu m/min$ and Ra surface roughness value of around $0.258\mu m$ as shown in their experimental results in [33]. Kang et al. developed a method for high-speed finishing of internal surfaces using a set of poles outside the workpiece, magnetic abrasives on a finishing tool attached on a rotating chuck [34].

A proper technique for monitoring the inside could provide feedback so that a close-loop control can be implemented during polishing. Then, making grinding processes autonomous can dramatically reduce a component's manufacturing cost as mentioned by Ramachandran et al. [35]. The problem is that robot manipulators in such complex structures or other conventional tools e.g. drills, are not applicable. However, the potentiality mentioned by the

authors in [35] is towards quality and strength improvement of the manufactured product. Also localisation plays a crucial role during operation and it is necessary not only to navigate the microrobot to the desired location inside a sophisticated structure but also to preserve its position to uniformly polish the area of interest. Son et al. presented a localisation method using a Hall-effect sensor array to estimate the position of a magnetised object [36]. A similar or the same approach can be used to help the tracking of microrobot while operating on the inside of the structure it operates. However, this method is prone to magnetic field strength and the distance between a magnetised microrobot and the sensor in order to be detected.

Along with summary of contents in friction in [17, 18], manufacturing processes such as grinding/machining in microscale need to consider tribology factors and modelings in order to obtain an efficient process as described by Jackson and Morell [37]. Moreover, Mahoney and Abbott validated experimentally and presented a mathematical modeling for managing the magnetic force of a dipole moment [38]. Based on derived equations the actuator's rotational speed can be controlled in an effective way, by managing the magnetic force. Demonstrations of a magnetic device rolling and levitating under the effect of the magnetic force, were presented. The mathematical modeling presented is the main contribution of their work, and the results presented indicate a potentiality of magnetic manipulation and the controllability of the used subject. Abbott et al. also presented a mathematical model for calculating the magnetic torque and force exerted on a nearly ideal soft-magnetic ellipsoid object [39]. A magnetisation model was developed for two different regions, preserving continuity during transition from one region to the other. Their modeling was validated experimentally, using existing measurements and a custom-made magnetometer. The obtained results indicate that the geometry of the body seems to play a crucial role in its behavior inside a magnetic field, whose developed model curves were sufficiently relevant to the existing measurements. However, other geometries were not presented as comparing examples and using this particular ellipsoid, was an almost ideal choice.

Fig. 1.2 shows a component of motor engine with complex morphology having different geometries and passages with varying diameters optimally designed by Li et al. [40]. Other engine parts e.g. engine blocks, engine intake manifolds, exhaust manifolds have shapes of high complexity that make some of their internal areas unreachable and non-polishable with conventional ways [41]. More specifically, in abrasive flow finishing where a visco-elastic polymer with abrasives flows through a passage to polish it, variations in geometry from passage to passage can lead to unpolished corners, edges, etc. due to the drop of pressure and dynamics of polymer's flow. Also, the edges of passages are potentially overpolished when the polymer flows from a larger passage to a more narrow one or underpolished in the opposite case.

To overcome accessibility issues due to narrow passages and variations in geometries of

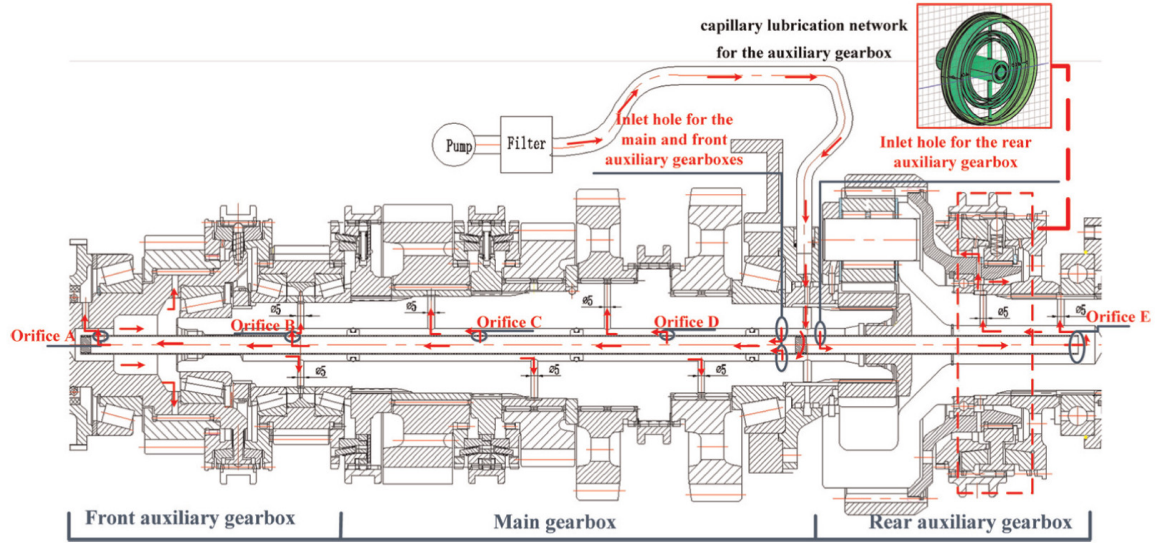


Figure 1.2: Lubrication circuit passage diameter variation where orifices diameters are $D_A = 3.5\text{mm}$, $D_B = 2.5\text{mm}$, $D_C = 3\text{mm}$, $D_D = 1.5\text{mm}$, $D_{\text{Main front}} = 5\text{mm}$, $D_{\text{Aux rear}} = 2\text{mm}$, respectively [40].

the workspace, using smaller modules/components to navigate through them is an option. Assembling the components into a larger module or operating as a swarm so to enhance their performance through collaborative behavior could be really advantageous. Reconfigurability should be more than necessary in such cases so that the applied microrobot can adjust its behaviour based on its surrounding environment. Pawashe et al. designed and fabricated assembling and disassembling micromodules they named Mag- μ Mods [42]. Fabrication techniques refer to the NdFeB magnet (Mag- μ Bots) encased in a PDMS mould and the electrostatic grid surface which was used to anchor the modules, in order to be disassembled. However, the environmental conditions used would not be that convenient in the case of operating inside metal components or if a larger amount of them collaborate and overlap, where disassembly tasks are unable to be performed.

Simultaneous multi-microrobot/swarm actuation approach might be implemented, considering the assembly of many to an adjustable larger one. Becker et al. designed ensemble open-loop and closed-loop control algorithms for swarm robot positioning tasks [43]. The focus of motion was only positioning on the plane under rotations and linear drivings, similar to unicycle. However, in case of remote actuation using magnetic field, obtaining a dissimilar behavior among many microrobots under the same field direction and strength is still challenging. Xie et al. used haematite particles to obtain swarm behavior on specific tasks in microrobotics [44], based on the work of Driscoll et al [45]. They demonstrated four types of motion, rolling, tumbling, spinning and oscillating, and they provided supplementary material of alternations between motion states by magnetic field manipulation. They measured the time needed to change motion states so to experimentally evaluate the fast

response. Although the obtained results demonstrate the high precision of motion and the low complexity during operation, there are still the limitations derived from the workspace setup and particles' small size when it comes to stress production required to overcome the yield strength of a material for polishing.

The matter of communication inside the working space is also important for monitoring the status and the progress of the operation, for detecting any unwanted behaviours or for interacting reasons between the microrobots. Corradi et al. designed and fabricated an optical system used for sensing between swarms of microrobots [46]. The main contribution of this work was the fabrication of this optical system and the communication technique demonstrated, along with the simulation results.

An innovative programming methodology was developed and described, for magnetic soft matter control by Lum et al. [47]. In particular, 2D-Fourier Series were used to compute the desired magnetisation profile and the actuating fields as a prefabrication process. The magnetisation profile was used during the fabrication process to obtain the preferable one for the material. This offers high velocities during operation, since no online calculations required, as they were made in advance. The described preprocess seems to be the time-consuming part and the fabricated beam is targeting a specific task. The authors of this paper demonstrated the use of the proposed method with various examples of beam-based robots, presenting also the opportunity for universality. Such structures may assist polishing processes of internal surfaces if magnetised properly and applied in combination with or as part of a microrobot, especially by taking advantage of the 6-DOF actuation [48, 49].

1.2 Challenges

This particular research topic and the application fields that it targets are governed by various laws of physics that affect the behaviour of the applied techniques, and knowledge and technological gaps that need to be explored further for better understanding and description of them. The most important ones are the following:

- Sufficient shear force production
- Polishing blind spots and reachability inside complex geometries [21, 30]
- Controllability/Navigation [50–57]
- Multi-components operation [58]

- Obtaining the desired roughness, surface quality [29, 34, 59, 60]

Many of the challenges, for instance the small size of the applied-to structures and consequently the size of microrobotic mechanism(s) are common to all these fields of application. Tan et al. focus on the limitations of currently used tools to structures with geometries of high-complexity [21]. In particular, in automotive/aerospace engineering applications, the obtained surface roughness requirements are really high, e.g. to preserve an engine's smooth/stable operation or reduce fuel consumption. Maintaining the balance between damage avoidance in every aspect of any field and the high polishing performance it is assumed to be the biggest challenge of this research. Finally, a very important challenge of this research is to obtain the surface roughness of the internal surface after finishing, that is required for the specific applications in the field.

1.3 Aims and objectives

The main target of this research project is to design and fabricate magnetically-actuated microrobots for controllable remote-finishing of internal surfaces of complex structures for applications in industry and medical science. More specifically, the fields of interest that the aims can be classified into and consequently be distinguished are the automotive and aerospace industry. In the following two paragraphs, the aims of this research for each one of the above fields, are being described respectively.

Increasing demands in aerospace and automotive engineering and industrial applications include post-process of the manufactured components used in motor engines. Such post-processes are grinding and polishing/finishing the internal surfaces of the produced parts after the manufacturing process (3D metal additive manufacturing). Although these components can be made in one step, it is still not feasible to obtain internal surface roughness of less than $7\mu m$, which is required for applications in the above fields [16, 61]. This research aims to develop an approach using (a) magnetically-actuated microrobotic mechanism(s) and aid the polishing process of the inside of such components in a remotely-controlled way. The reasons for using microrobotics to deal with this kind of problem are mostly the reachability they offer and the controllability of the process that is needed to overcome problems that have been experienced using conventional methods (AFM). Among others, these include having polished geometries with areas that are either excessively polished (overpolished), not sufficiently polished (underpolished), or even not polished at all (blind spots).

Blood flow in arteries of living organisms can be highly affected by the arteries' inner

condition. Usually high cholesterol levels or even plaque can be accumulated in humans' arteries (arterial plaque), which can lead to heart attacks or strokes when blood clots inside arteries. Even if the worst case scenario does not occur, such unwanted substance when accumulated on the artery wall can reduce the blood flow and affect someone's health condition, potentially increasing the danger for many other diseases to be developed. Among the aims of this research is also to develop a polishing technique to completely remove this accumulated substance from artery walls or significantly reduce its levels, so to avoid any surgical operation, use of drugs or chemical peels, and consequently reduce the waste of money and unpleasant experience for the patient in these cases. More specifically, micro-robotic mechanisms it is planned to be designed for this cause and to aid such operations or totally replace them, using the polishing methods developed and the knowledge acquired from other fields of this research. Scaling down the mechanisms planned to be used in industrial applications even more, and modifying the theoretical modeling can potentially be applied into medical applications, similar to the ones mentioned earlier in this Chapter.

With the above aims forming the axis of this research project, the objectives were planned and are described here:

- (i) Develop a polishing system with remotely-actuated components in order to have the ability to target unreachable areas.
- (ii) Study the shear stress needed to polish certain surfaces and use the developed system as a proof of concept to create a controllable microrobot able to access areas of interest.
- (iii) Develop a localisation method composed of a system able to detect the location of the microrobot inside the subject structure during operation and navigate it towards the goal area and appropriate configuration for polishing.
- (iv) Develop a control algorithm to maintain the device in place so to perform the polishing process as predicted due to absence of monitoring of the surface condition.
- (v) Evaluate the polishing methods' performance in terms of speed, material removal (rate), surface roughness (for quality), and localisation method with respect to the accurate estimation of the microrobot's position inside the subject structure being polished and the ability to efficiently actuate it and navigate it through it.

In total, a polishing system composed of a microrobot operating inside a complex manifold, and which is remotely actuated and navigated under a localisation algorithm would provide a complete approach targeting this research's problem.

1.4 Research Contributions

In this project we attempted to deal with the existing challenges in the field that we mentioned in Section 1.2. The main aspects we focused on were the reachability of targeted areas in complex geometries, controllable microrobots for polishing internal surfaces, maintaining position of the polishing microrobot for uniform polishing results and providing the required shear stress to polish surfaces of interest. The main contributions of our work can be summarised in the following:

- 1) A magnetically actuated polishing method for remote surface polishing,
- 2) Design and fabrication methods for polishing microrobot prototypes with embedded abrasives for targeted internal surface polishing,
- 3) A point-to-point (1D) localisation method using an array of vibration sensors.

1.5 Dissertation outline

Introductory terms related to this project and work done in the fields the previous years, the scope and objectives of this research, along with the challenges that will be faced towards its aims are all included in Chapter 1. Chapter 2 contains the methodology followed to demonstrate preliminary polishing techniques targeting acrylic plates used as a proof of concept. The theoretical study and fabrication of the polishing systems, the experimental setups and data analysis methods we used, along with the results of the above methodology are being presented also in Chapter 2. In Chapter 3 we present a polishing approach where magnetically-actuated microrobots are able to operate in narrow spaces under the effect of an electromagnetic coil system. Chapter 3 also contains the fabrication process of the microrobot, along with its variants and results obtained during the experimental trials of their actuation. Our localisation method using vibration sensors is presented in Chapter 4, including sensing results and the method's performance evaluation. Each chapter has its own Discussion and Conclusion section. However in Chapter 5 we included a general discussion with the challenges we faced and addressed in this project, providing some ideas for future work and what else is missing. Finally, Chapter 6 concludes with this project's content and some last thoughts.

2

Remote Magnetically-directed lapper-bot

” *Nothing has such power to broaden the mind as the ability to investigate systematically and truly all that comes under thy observation in life.*

– Marcus Aurelius –

2.1	Introduction	15
2.2	Methods	15
2.2.1	Remotely-actuated polishing with permanent bar magnets . . .	16
2.2.2	Magnetic actuation of lapper	18
2.2.3	Direct magnetic coupling polishing method	20
2.2.4	Indirect magnetic coupling polishing method.	22
2.2.5	Design and fabrication	22
2.2.6	Shear stress and torque analysis	23
2.3	Material removal analysis	26
2.3.1	Weighing polymer plates method	26
2.3.2	Digital image processing methods	26
2.4	Results	28
2.4.1	Shear stress estimation results	28
2.4.2	Weighing polymer plates results.	28
2.4.3	OpenCV data analysis results.	30
2.5	Discussion	30
2.6	Conclusion.	33

2.1 Introduction

Moving towards the aims of this research, we developed a method for grinding a poly-methyl methacrylate (acrylic) surface at a designated location to remove an amount of unwanted material. Due to COVID-19 pandemic limitations, this method was developed in two stages, leading to two different versions of it. In the beginning, we could not have access to any of the laboratories of the University, not yet a clean room facility required to fabricate microrobotic devices. This is the reason we developed a method used for proof-of-concept purposes as an initial stage using common electronics for simple circuits at home. It is considered to be a slurry-free grinding method with the use of abrasives. It mimics the lapping process which has been used in industry for machining surfaces.

When the COVID-19 regulations changed and we could have limited access to some lab facilities, we managed to improve the initial method. This specific method developed in particular for polishing surfaces by coupling two discs together using cylindrical NdFeB permanent magnets. The magnets were attached to the discs with opposite orientations, altering them in a circular pattern. In this method, one of the two disks, the so-called coupler, was screwed on a rotating shaft attached to the DC motor, which was used to generate the required torque to be transmitted to the other one performing the grinding process. The other disk, the so-called lapper, was used to perform the polishing of the unwanted material on the acrylic surface, mimicking the lapping process. The performance of the advanced version was evaluated using Open CV and digital image processing methods applied to the footage from a camera that was capturing the process. Another evaluation method was to weigh the polished surfaces with a high precision scale before and after the material removing process and calculating the material removal rate based on the duration of the process.

2.2 Methods

In this section we present the methods developed and followed to perform and study the polishing process of cured correction fluid that was solidified on acrylic plates. We classified and distinguished the methods that we developed and studied, based on the type of magnetic actuation during operation.

2.2.1 Remotely-actuated polishing with permanent bar magnets

This particular method was developed in two versions. The first one was composed of a set of six bar magnets attached to a DC motor, rotating under a plastic container. The bar magnets were magnetised through thickness, while the plastic bottle was sitting on a platform that was custom-made at home. A piece of emery cloth with 0.5mm thickness was cut in a circular disc shape of $\text{Ø}30\text{mm}$ diameter and sets of axially magnetised $\text{Ø}2\text{mm} \times 1\text{mm}$ cylindrical magnets were glued and/or taped down on it in various configurations experimenting with its polishing performance. Fig. 2.2(a)-(c) show the magnets' configurations used in trials, with blue arrows denoting the north pole of the magnets placed. Fig. 2.2(d) shows the other side of the emery cloth surface that has the abrasives for the polishing feature. Configuration in Fig. 2.2(c) also required tape to hold magnets in place because magnetic attraction could overcome super glue's strength due to their closer distance compared with the configurations in Fig. 2.2(a) and 2.2(b).

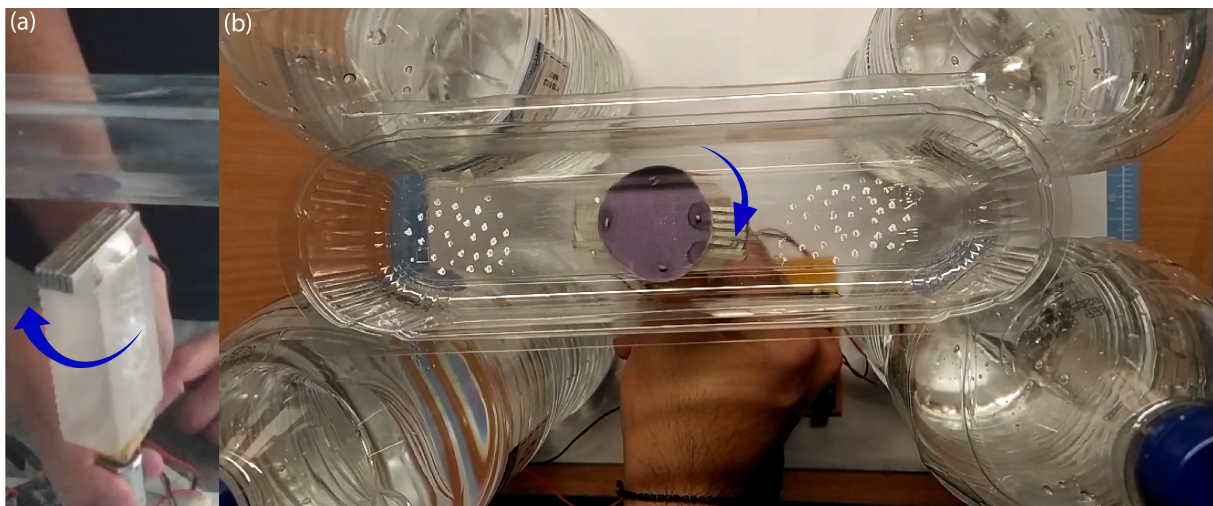


Figure 2.1: (a) Side, and (b) top view of the system setup we used during trials. The appearing arrows are pointing in the direction of rotation during operation.

An Arduino Uno microcontroller was programmed and used to actuate a DC motor that was spinning the set of bar magnets. All the electronics and the assembled components used for the purposes of this method are shown in Fig. 2.3. The depicted parts were located right underneath the surface to be polished with the discoid piece of emery cloth used every time being on top of the surface.

The evaluation parameters involved the rotational speed of the disc, the disc's stability under actuation, and material removal rate. The polished unwanted materials were ink and correction fluid, while the input variables were the motor's rotational speed and magnets'

distance from the disc, and consecutively from the magnets attached to it. We performed three trials with each configuration of magnets on the disc of emery cloth, with the actuating magnets being at distance 2cm and 1cm away from it during polishing. The rotational speed was varying as we manually applied voltage with a switch (see Fig 2.3) so to couple the actuating magnets with the magnets on polishing disc. The duration of our trials was approximately 2min since we could not manage to either couple the sets of magnets properly, or observe some material removal during polishing. Fig. 2.4 shows the condition of the plastic surface after polishing a few dots of correction fluid left to dry on it with emery cloth used by a human's hand.

During the experimental trials in all cases, the plastic surface was not scratched in a way such that the correction fluid could be removed from it. The design shown in Fig. 2.2(a) could not rotate properly on the surface since it was "skipping steps" as magnetic poles were spinning. Meaning, that the magnets were decoupled and coupled again quickly, which led to the disc wobbling or flipping upside down and not operating with stability inside the workspace. In the next design presented in Fig. 2.2(b) we added two more magnets to cover the case of "skipping steps" and it could rotate slightly better than the previous one.

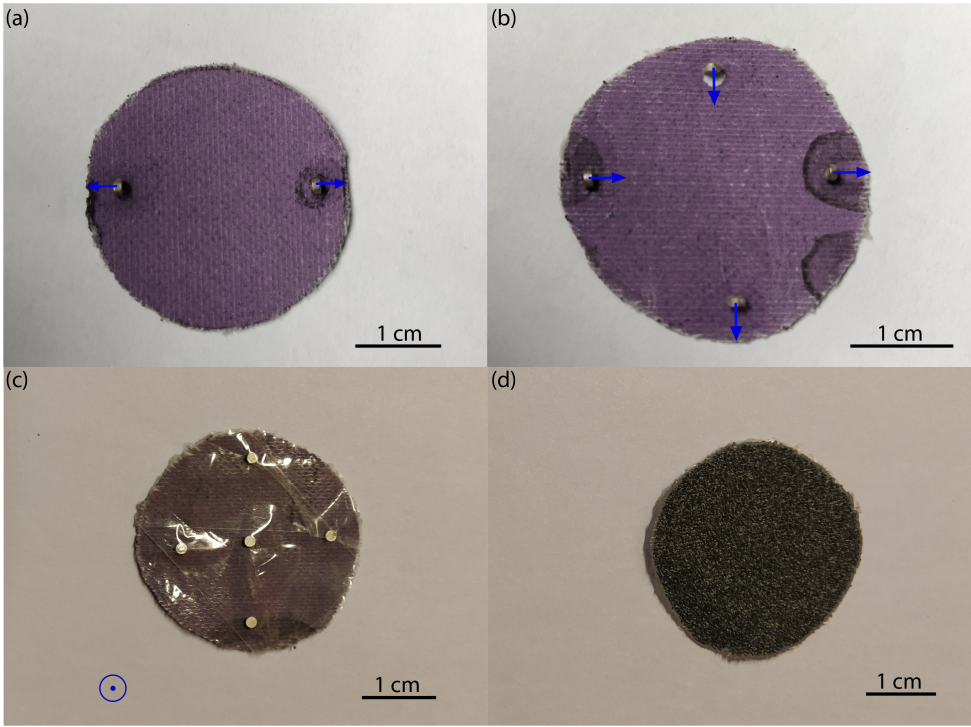


Figure 2.2: (a), (b), and (c) Configurations of $\varnothing 2\text{mm} \times 1\text{mm}$ cylindrical magnets attached to a discoid piece of emery cloth with opposing polarity, (d) side of emery cloth with abrasives for polishing

However, this was only in low rotational speed, while as speed was increasing it still experienced disturbances and similar undesired behaviour. The design appearing in Fig. 2.2(c)

had an additional magnet at its centre and the orientation of magnets was changed to potentially increase its rotational speed and overcome the unstable rotation. Unfortunately, it was going back and forth and occasionally rotating due to improper polarization between magnets. By using one bar magnet and changing the orientation of it on the actuating shaft, the disc could rotate surprisingly fast, following the rotating motion of the single bar magnet actuating it. This was due to the proper coupling between magnetic poles of the magnets. Nevertheless, the shear stress was not sufficient to remove the correction fluid stains from the surface. More precisely, the plastic surface was scratched to a degree that the scratches could be discerned, but the correction fluid was not removed from the surface. This led us to our following method presented in the next section.

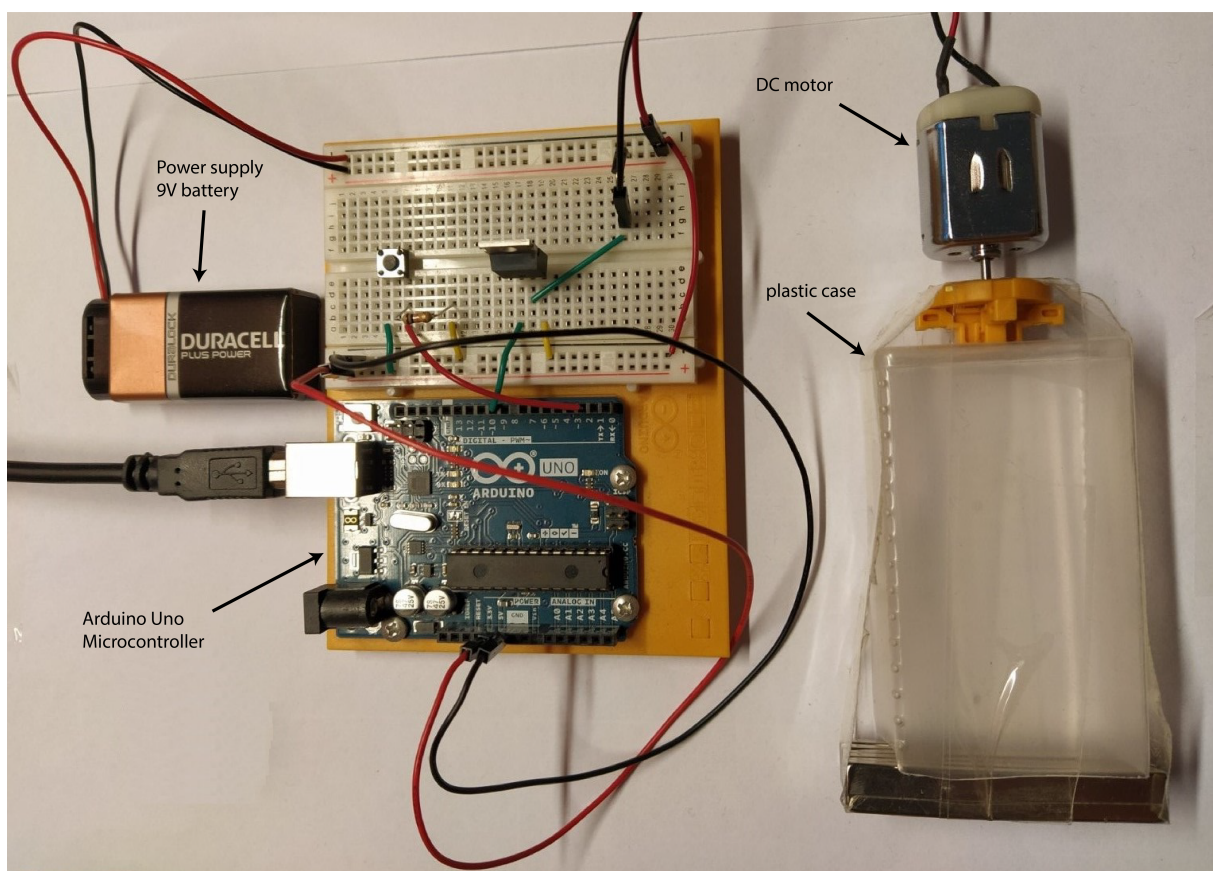


Figure 2.3: The assembled components and circuit that we used during the experimental phase

2.2.2 Magnetic actuation of lapper

The method presented here is a variant of the previous one that was developed after some limited access to laboratory facilities and better equipment had been granted. This helped a bit further with the evaluation process and the experimental setup improvement.

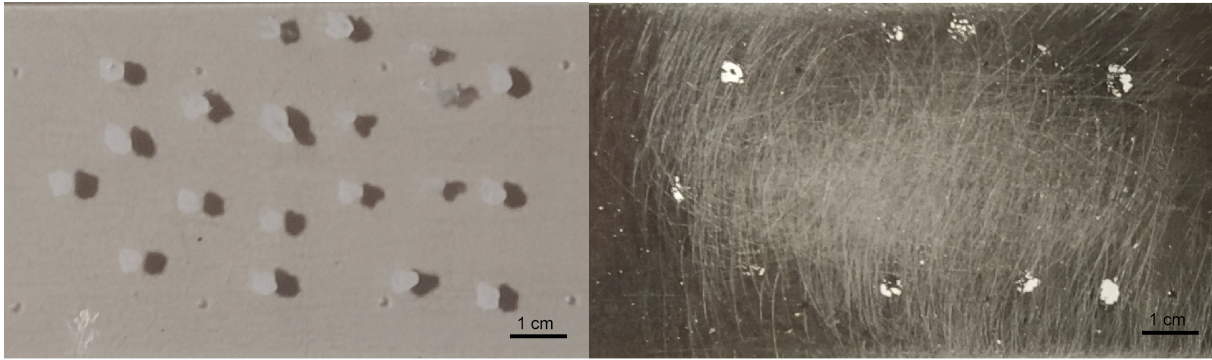


Figure 2.4: A plastic surface with correction fluid before (left) and after (right) polishing with a discoid emery cloth with hands-applied forces

Also, the developed 3D printed models helped to build a more solid and powerful station for the polishing trials, with potentially increased applied forces and produced shear stress. Both methods work by remotely actuating polishing discs using different sets of magnets that are attached to a rotating shaft.

The system presented in this method consisted of a rotating shaft mounted on a 3D-printed structure, which encased a DC motor for its actuation. The DC motor was operating with a 6A power supply unit, while the current and voltage were manually adjusted with a knob by a human operator. The applied voltage to the DC motor was within the range of 3.1 V (surpassing friction forces) and was increased gradually (approximately 0.1 V/s) up to 4.6 V. Note that going beyond this voltage, decoupling effects were experienced that required operation to restart from the beginning so to obtain back the coupling between magnets. Based on the method, at the end of the shaft there was attached one of the following:

- 1) A 3D printed disc of polylactide (PLA) with ten cylindrical NdFeB magnets ($\varnothing 2mm \times 4mm$) attached to it, the so-called 'coupler' (Direct Magnetic Coupling Polishing)
- 2) A 3D printed case of polylactide (PLA) carrying a set (six) of bar magnets ($60mm \times 10mm \times 3mm$) used to transmit torque to a variant of the 'coupler' model used in (1) (Indirect Magnetic Coupling Polishing)

In both cases, a module performing the desired task of removing the unwanted material is used on the other side of the surface. Fig. 2.5(a) shows the configuration of the system used during the method in case (1), while a close-up of the system with the variant of the method in case (2) is being shown in Fig. 2.5(b). Both methods and their parameters are further explained individually in the following sections.

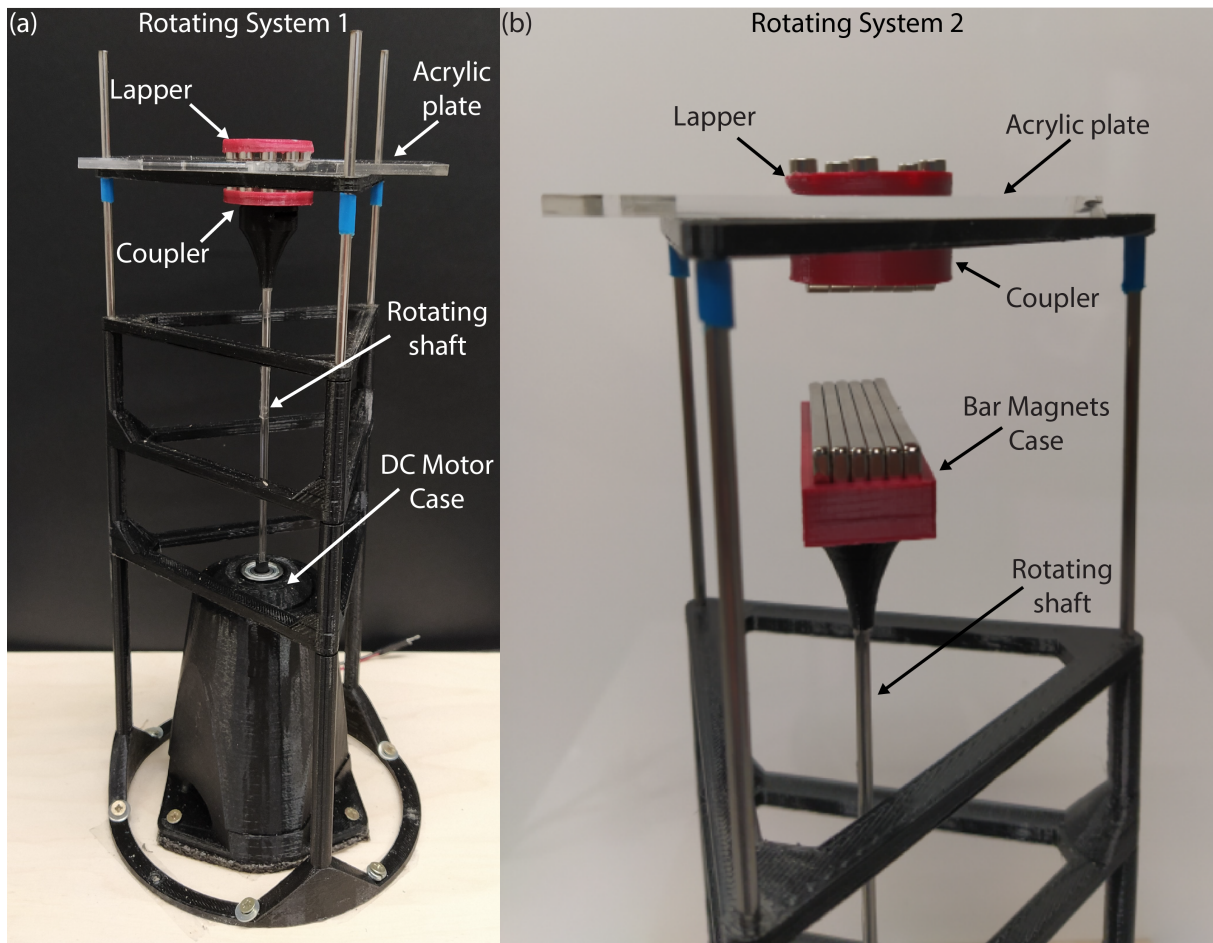


Figure 2.5: (a) Physical view of the system configuration used in case (i). (b) A close-up physical view of the system configuration used in case (ii).

2.2.3 Direct magnetic coupling polishing method

In this particular method we use two rotating discs, the so-called lapper, and coupler, because of their functionality. From now on, we will refer to the one removing the unwanted material as the lapper and the one coupling it from the other side of the surface as the coupler. Fig. 2.6(a) and Fig. 2.6(b) show the physical view of the lapper and the coupler, respectively. Ten NdFeB axially magnetised cylindrical magnets are attached to both the coupler and the lapper with their orientation alternating as shown in the schematic view in Fig. 2.6(c), where the blue and red colours denote the north and south poles, respectively. The reason for this configuration is to couple the two rotating discs with this alternating pattern and use the coupler, from one side of the polymer surface, to actuate the other (lapper) on the other side of it. The coupler in this particular method is screwed onto the rotating shaft located underneath the polymer surface at a distance of 10mm . Hence, the torque is generated by the DC motor and is directly transmitted to the lapper via the coupler attached

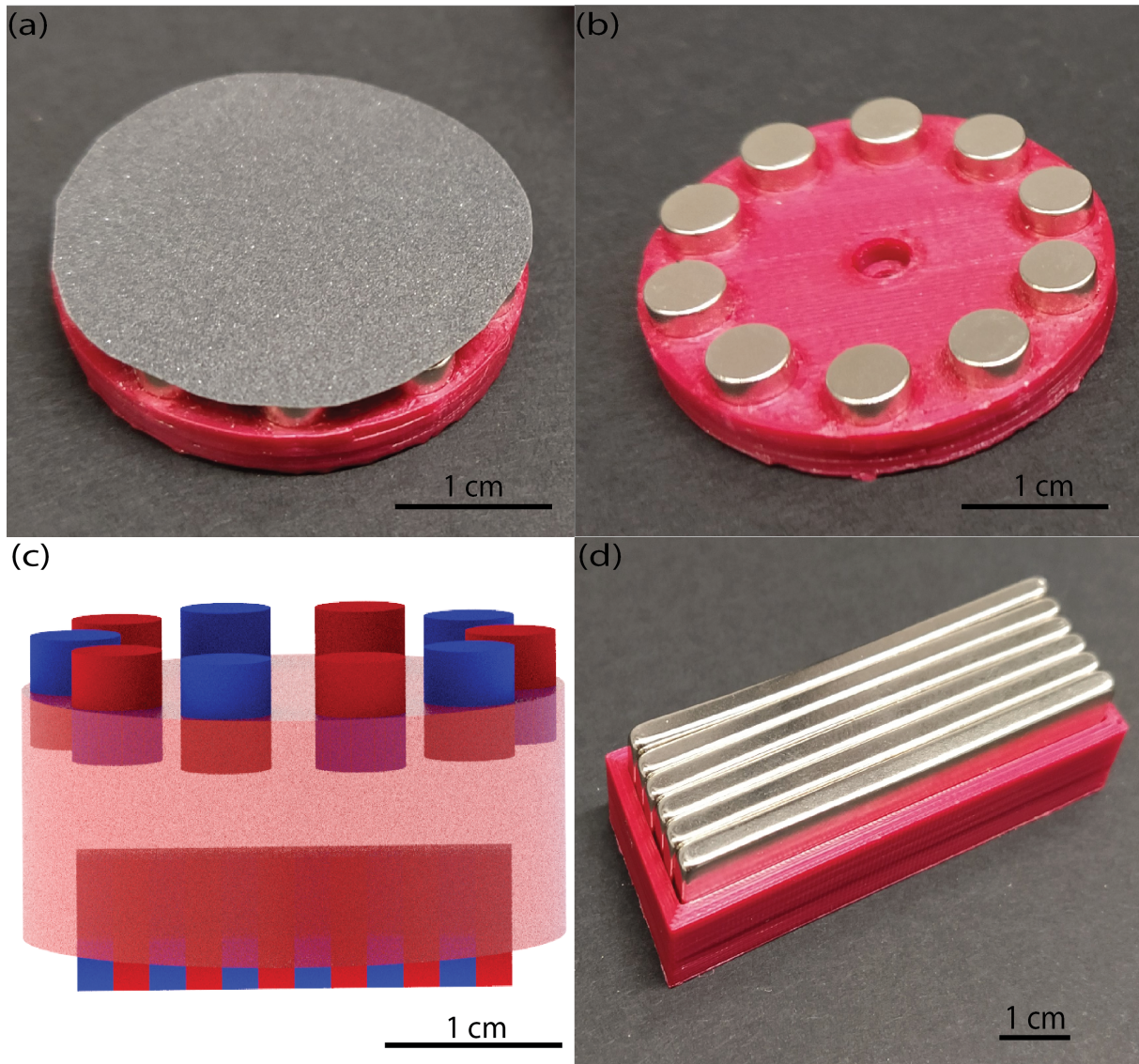


Figure 2.6: Physical designs of (a) the lapper, and (b) the coupler. (c) Transparent model design of the remotely actuated coupler in the case of using bar magnets for torque transmission, and (d) physical design of the bar magnets PLA case.

to the rotating shaft. The torque transmission is preserved as long as the magnetic coupling holds the coupler and the lapper together. The distance of 10mm has been decided after an extended number of trials and tests so to have enough normal force due to magnetic forces and consequently shear stress. At the same time, we had to reduce the friction forces generated on the surface due to magnetic attraction, so it can be relatively easy to actuate the lapper and polish the surface without interruptions.

2.2.4 Indirect magnetic coupling polishing method

This method uses an indirect way to rotate the coupler. This is obtained by adding 6 cylindrical magnets at the bottom of the coupler as shown in Fig. 2.6(c) and using 6 bar magnets at a distance 20mm away from the coupler to actuate it. We picked the distance after checking various distances until the bar magnets have no actual rotating effect to the magnets being on top of the coupler. Then we would only have the rotational motion of the coupler due to the magnets being at the bottom of the coupler. The bar magnets are encased in a PLA structure which is shown in Fig. 2.6(d). Note that the illustration in Fig. 2.6(c) is included to show the configuration of the horizontally-placed magnets and their position in the PLA structure. Compared to the previous version, the lapper in this one carries only half of the magnets to reduce the attraction forces between the coupler and the lapper, and without alternating polarity. This way, the lapper can overcome the friction forces when rotating during operation. During our trials, keeping all of the magnets as in the previous version held the coupler and the lapper coupled together and no rotation was possible. In this version, the torque is transmitted indirectly to the lapper from the actuator via the coupler's additional horizontally-placed magnets and their configuration at its bottom. This system takes advantage of the coupler's ability to simultaneously be actuated by the bar magnets and indirectly actuate the lapper. However, the attraction forces were not enough to obtain material removal results on the polished surface when we had half the magnets. We decided to include this method for future investigation, and present only the fabrication process followed and the results obtained by the direct magnetic coupling polishing method in the following sections.

2.2.5 Design and fabrication

Both the lapper and the coupler are 3D-printed designs made of PLA, using a Prusa i3 MK3S 3D printer. Table 2.1 contains the coupler's and lapper's parameters and their values, along with the N42 cylindrical magnets' properties. Note that the properties' values of the last, refer to room temperature operation.

A small variation in the lapper's weight (2.241g) occurs due to its infill density (20% in contrast to the coupler's 50%). The reason for this is that the lapper was needed to be more compact/solid/heavy, while the lapper lighter to avoid causing severe damage to the polymer surface. The infill pattern we use for both the lapper and the coupler is gyroid type, while the top and bottom ones are rectilinear. The temperature of the extruder and the bed for all the layers during the printing process are set to 215° C and 75° C, respectively.

Table 2.1: Parameters and properties of components

Component	Parameter/Property	Symbol	Value
N42 NdFeB Cylindrical Magnet	Diameter	d_m	$\varnothing 5mm$
	Thickness	h_m	4mm
	Weight	w_m	0.58g
	Residual induction	B_r	1280-1320 mT
	Coercive force	H_c	12000 Oe
	Max energy product	$(BH)_{max}$	318-342 kJ/m ³
Coupler and Lapper	Diameter	d_c	$\varnothing 30mm$
	Weight*	w_c	2.461g
	Thickness	h_c	4mm
	Number of magnets	N_c	10

The structure we use to encase the 6 bar magnets is also a 3D-printed design using the same equipment and settings with the lapper, meaning low infill density. This is because the magnets' total weight was already too much for the shaft to carry. The rest of the system, meaning the base encasing the DC motor, the rotary shaft, and the bearings were designed and fabricated by Alfred Wilmot.

2.2.6 Shear stress and torque analysis

The simplified model that describes the shear stress exerted on a rotating disc at its circumference is given by the following expression [62]:

$$\sigma = \omega^2 r^2 \rho / 3, \quad (2.1)$$

where ω denotes the angular velocity of the lapper, r its radius, and ρ its density. The relation between the shear stress and the lapper's angular velocity can be seen in Fig. 2.7. However, this model is not accurate to calculate the shear stress exerted on the polymer surface, since it is not affected by friction forces due to magnetic attraction.

There are two models to derive the magnetic torque and force exerted on the lapper. One of them is by using the models summarised by Abbott et al in [63]. The potential energy, between two sets of magnets (bar and cylindrical magnets) at relative distance r_{bc} , is given by the following formula:

$$U_{bc} = \frac{\mu_0}{4\pi} \left[\frac{m_b \cdot m_c}{r_{bc}^3} - 3 \frac{(m_b \cdot r_{bc})(m_c \cdot r_{bc})}{r_{bc}^5} \right], \quad (2.2)$$

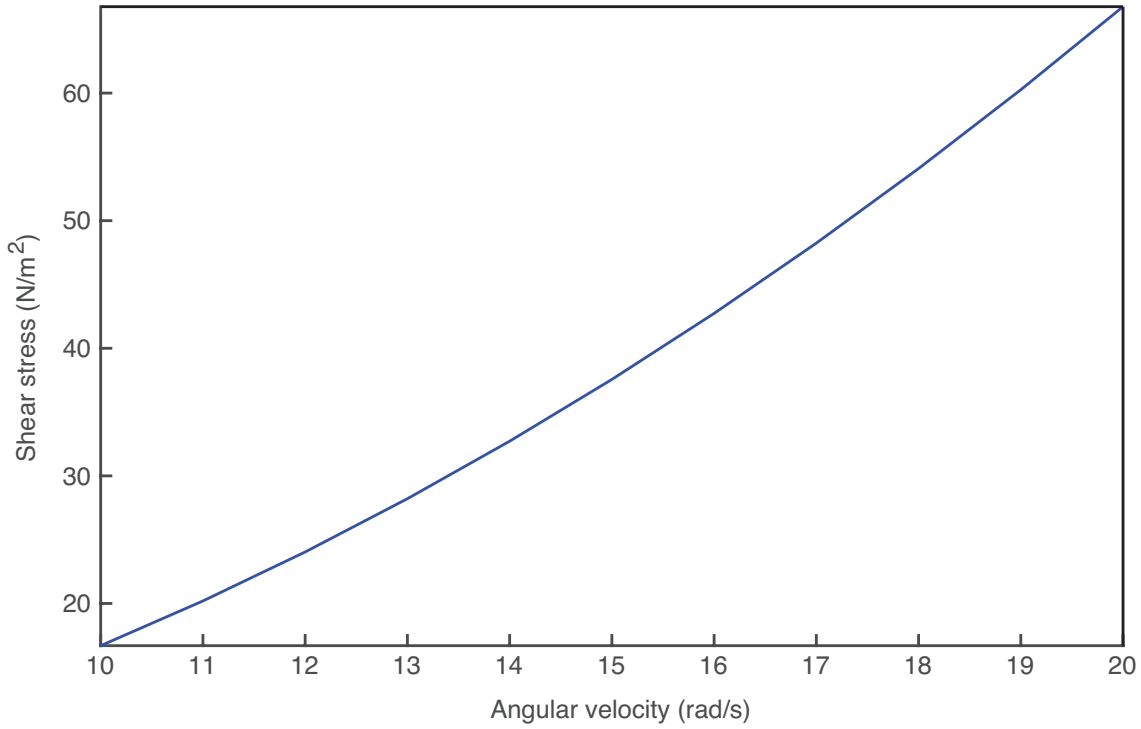


Figure 2.7: The shear stress produced at the circumference of rotating disc without friction with respect to the lapper's angular velocity based on Eq. (2.1)

where $\mu_0 \approx 4\pi \times 10^{-7} \text{ T} \cdot \text{m/A}$ is the vacuum permeability, and with m_b and m_c we denote the magnetic dipole moment of bar and cylindrical magnets, respectively. This simplified model is not taking into consideration the geometry of magnets and the relative distance was calculated from the magnets' centre of mass. Since their geometry is not complex, the magnets are assumed to be point dipoles and their magnetic fields can be represented by a single magnetic dipole moment. The magnetic force of bar magnets exerted on the coupler:

$$\vec{F}(r_{bc}, m_b, m_c) = \frac{3\mu_0}{4\pi r_{bc}^5} [(m_b \cdot r_{bc})m_c + (m_c \cdot r_{bc})m_b + (m_b \cdot m_c) r_{bc} - 5 \frac{(m_b \cdot r_{bc})(m_c \cdot r_{bc})}{r_{bc}^2}]. \quad (2.3)$$

The same model can also be used to have the cylindrical permanent magnets with the coupler instead of the bar magnets. The model is simplified in that case since all the magnets are identical. A general code was written in MATLAB[®] (see Appendix A) for calculating the magnetic force between magnets being separated by a distance r , considering their

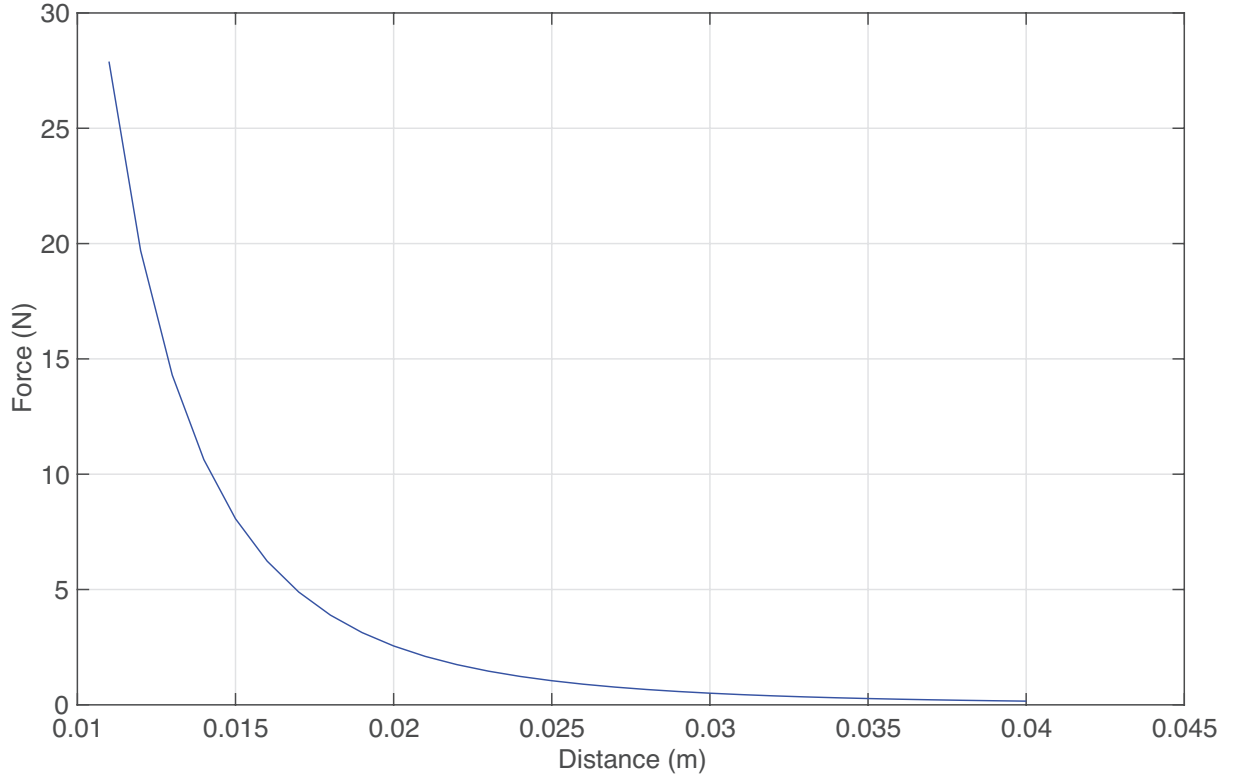


Figure 2.8: Model of the magnetic pull force between the cylindrical magnets with respect to the distance between them based on Eq. (2.3).

characteristics (dimensions, saturation magnetisation, number of magnets, etc.). Fig 2.8 shows the magnetic pull force between the 10 cylindrical $\varnothing 5\text{mm} \times 4\text{mm}$ permanent magnets placed on the lapper and the pairing ones placed on the coupler with respect to the distance between them, based on Eq. (2.3).

Another way is using the model given by Miyashita and Pfeifer in [64] for calculating the exerted force and torque from a magnet i on a magnet j :

$$\mathbf{F}_{ij} = \mu_0 \int_{v_i} (\mathbf{M}_i \cdot \nabla) \mathbf{H}_j dv \approx \mu_0 v_i (\mathbf{M}_i \cdot \nabla) \mathbf{H}_j, \quad (2.4)$$

$$\tau_{ij} = \mu_0 \int_{v_i} (\mathbf{M}_i \times \mathbf{H}_j) dv \approx \mu_0 v_i \mathbf{M}_i \times \mathbf{H}_j, \quad (2.5)$$

where M_i is the magnetisation of the i -th magnet, v_i its volume and H_j the magnetic field produced by the j -th magnet. Note that we are assuming that the magnetisation of the permanent magnets is uniform.

2.3 Material removal analysis

In this section we describe two methods that were used to calculate the material removal of our polishing method. To measure the material removal of our polishing method, we used a set of polymer plates on which we added correction fluid and left it to dry. In the first method, we used the weight of the plates before and after the polishing process to measure the weight of the material removed. In the second one, we used a computer vision algorithm to estimate the percentage of material removed from the surface. Both methods are described in detail in the following two subsections.

2.3.1 Weighing polymer plates method

In this method, we placed square-shaped acrylic plates on a high-precision scale to measure their weight. After adding approximately 16 – 17g of correction fluid, we measured their weight again. Finally, one more measurement took place after polishing for 150s to measure the weight of the polished material. All the measurements are presented in the Results section of this chapter. Slight variations in their dimensions and weight are due to their fabrication process, and they were taken into consideration based on their relevance to the results. During experimental trials, each surface was labelled with a colour and for each one of them we used sandpaper of a specific grit attached to the lapper. The colour matching was done for clarification reasons during trials. The grit sizes were chosen after trials and observations, from medium (P80) to ultra-fine ones (P3000).

In this method, the material removal rate was calculated using the following expression [65]:

$$MRR = \frac{w_b - w_a}{t} \quad (2.6)$$

where w_b and w_a denote the weight of the surface before and after polishing, respectively, while t is the polishing duration.

2.3.2 Digital image processing methods

In order to evaluate our polishing methods described above, we developed a method to estimate the amount of removed material with respect to the time of polishing. In this section, we describe the method we used to collect all data regarding the process, i.e. material removal and material removal rate. We added approximately 16mg of correction fluid on

acrylic plates and let it cure before polishing. Then, we used one fixed camera on top of the system configuration to capture the amount and distribution of unwanted material on the polymer surface during polishing, while a second camera was capturing the process from the side. After every 5s of polishing the lapper was removed to allow for a clear view of the surface condition. Captured footage was processed using the OpenCV algorithm that Alfred Wilmot found and modified appropriately for this method [66], while screenshots of the result during every pause provided the measurements of quantifying the process performance, meaning the percentage of material removed due time. Fig. 2.9 shows snapshots of the method before and during the polishing process, respectively, along with the parameters' setup we used. Note that a dark piece of paper was used under the polished surface to create the proper contrast for the Open CV algorithm to work.

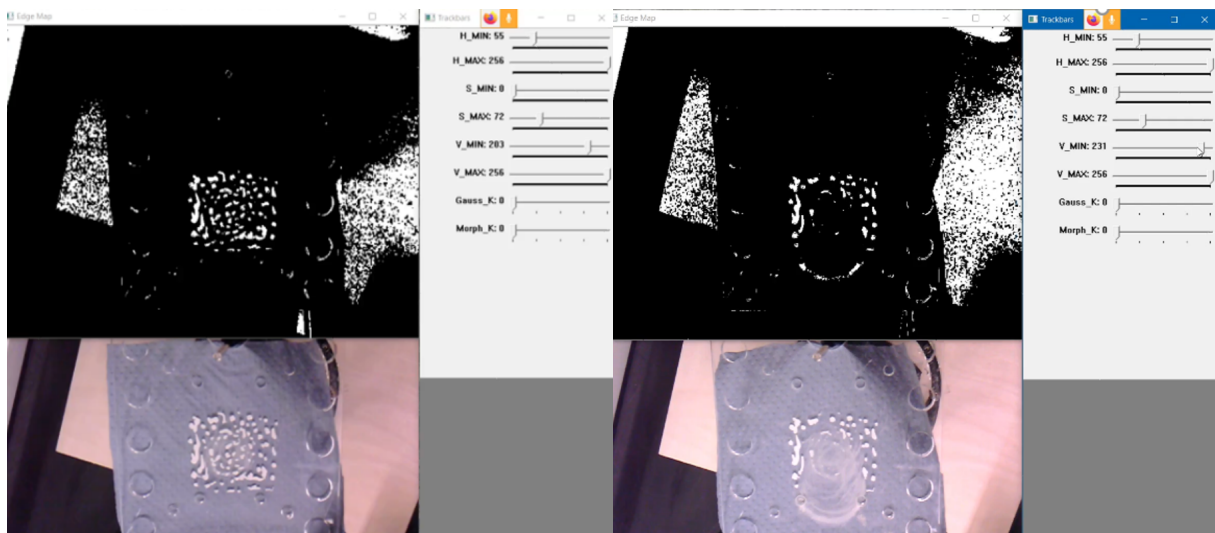


Figure 2.9: Snapshots from the camera input using the OpenCV algorithm before (left) and during (right) the polishing process.

Using the video footage captured and processed with this method, we could estimate the material removed per time interval. More specifically, black and white images were cropped to 80x80 pixels images and fed to a MathWorks MATLAB code developed for calculating the percentage of black pixels per image (See Appendix A). We post-processed the greyscale images by binarising their pixels values to 0s and 1s so to obtain black and white images. Finally, the percentage of black pixels in every image was calculated to derive a graph showing the material removed at any given time within the polishing phase.

2.4 Results

This section includes the results acquired during our experimental trials and the digital image processing methods. All the results presented in this section refer to the direct magnetic coupling polishing method.

2.4.1 Shear stress estimation results

To estimate the shear stress produced by the polishing component on the acrylic surface while polishing, a slow-motion video from a top view of the workspace was initially captured. Using motion tracking software (Tracker), we recorded the angle of rotation of an arrow we marked on its top, pointing in a fixed direction of the polishing component. The time frame we used was 10s, after the rotational motion during the polishing process was stabilised. In order to reach this point it takes approximately 15s, which is the time required for gradually increasing the applied voltage from 3.1V to 4.6V as described in Section 2.2.2. The recorded values of the angle of rotation and the derived angular velocity with respect to time are shown in Fig. 2.10(b). The angular distance θ presented in Fig. 2.10(a) describes the absence of disturbances during the process, since it is linearly proportional to the time.

We found the average angular velocity during this time frame to be $\omega = 16.5\text{rad/s}$, meaning it rotates around its z-axis approximately 2.6 times per second. Using the general model (Eq. 2.1) that calculates the shear stress produced by a rotating disc at its circumference, we found that the shear stress of the rotating disc was $\sigma = 45.5\text{N/m}^2$.

2.4.2 Weighing polymer plates results

Here we present the weights of the polymer surfaces that were put on a scale with a resolution of three decimal places. Approximately 16 – 17mg of correction fluid was added to all the polymer surfaces after weighing them. The weights of the polymer plates that were polished for 150s with emery cloth of the respective grit size are shown in Table 2.2. We use w_b to denote the weight before the polishing process, and w_a the weight after the polishing process. Using these weights and the expression in Eq. (2.6), we found that the average MRR of our method is $49\mu\text{g/s}$.

Fig.2.11 shows the surface condition of polymer plates after polishing and the amount of correction fluid remaining.

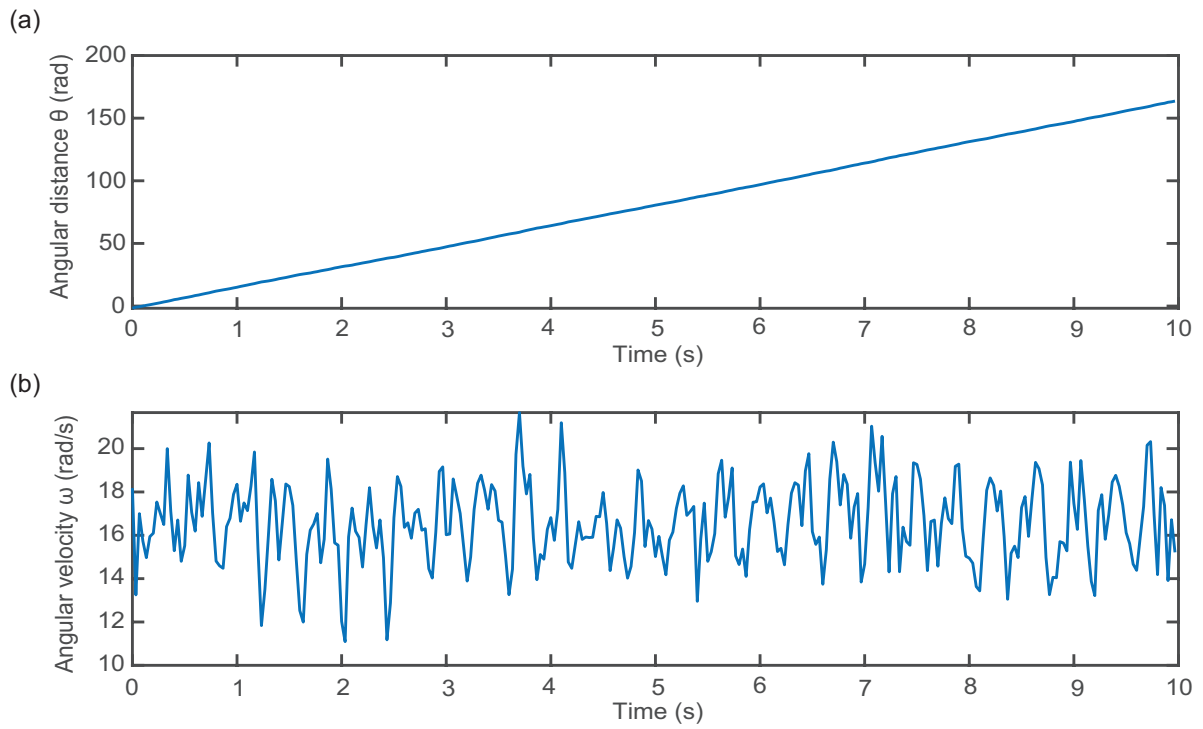


Figure 2.10: (a) Angular distance and (b) angular velocity of the rotating disc with respect to time

Table 2.2: Polymer plate weights

Emery cloth grit size	w_b	w_a
P400	23.781g	23.775g
P600	23.506g	23.500g
P800	23.446g	23.436g

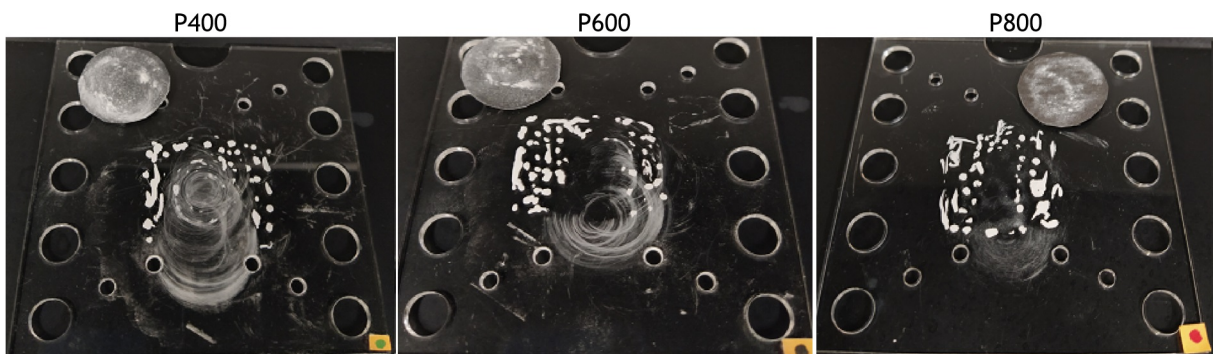


Figure 2.11: Polymer plates after polishing with emery cloth of the respective grit size

2.4.3 OpenCV data analysis results

In this section we present the obtained results from the digital image processing method we described in Section 2.3.2, in order to evaluate only the method described in Section 2.2.3. The duration of the trials was approximately 2.5min and it had been predetermined by trials and observations.

Fig. 2.12 shows the percentage of black pixels in each of the photos obtained by the digital image processing algorithm, that indirectly express the material removed during polishing trials. We would like to emphasise on the fact that this does not represent the percentage of material removed from the surface, but only the black/white pixel ratio. Also, note that a drop in the percentage of black pixels at around 125s is due to lighting effects during the footage capturing that have an impact on the data due to the algorithm's sensitivity. This sensitivity can be further adjusted along with the lighting environment to obtain more reliable footage and consequently more accurate measurements and evaluation of the method. Here, to estimate the material removal, we need to estimate the percentage of white pixels removed during the process. Note that 16mg of added material before polishing are reflected in Fig 2.12 as approximately 11% of white pixels, while when the process ended, this percentage dropped to approximately 4%. Hence, we can claim that we had approximately 7% of the appearing material removed over 2.5min . Alternatively, we can estimate that 4% of white pixels were approximately 5.8mg of correction fluid, meaning that the material removed was around 10.2mg . So the material removal rate can be estimated to be $68\mu\text{g/s}$.

2.5 Discussion

In this chapter two methods for removing correction fluid from acrylic plates were presented. All of the developed systems in the presented methods use magnetic actuation to rotate a polishing component (lapper) on top of the plate and an actuating component (coupler) operating under the plate and only used to actuate the one on top. For the first method we used a set of bar magnets as the actuating component and an emery cloth disc as the polishing component carrying small cylindrical permanent magnets in various configurations, most of them shown in Fig. 2.2. The actuating component was attached to a plastic case fixed on a DC motor transmitting the necessary torque for the remote actuation. However, the set of six bar magnets on the component added a lot of weight to the carrier and DC motor leading to a drop in rotational speed, and a wobbling motion to the main axis of rotation. As a consequence, the observed effect facilitated a smoother motion of the polishing component, resembling the natural kinematics of a human applying circular motions with

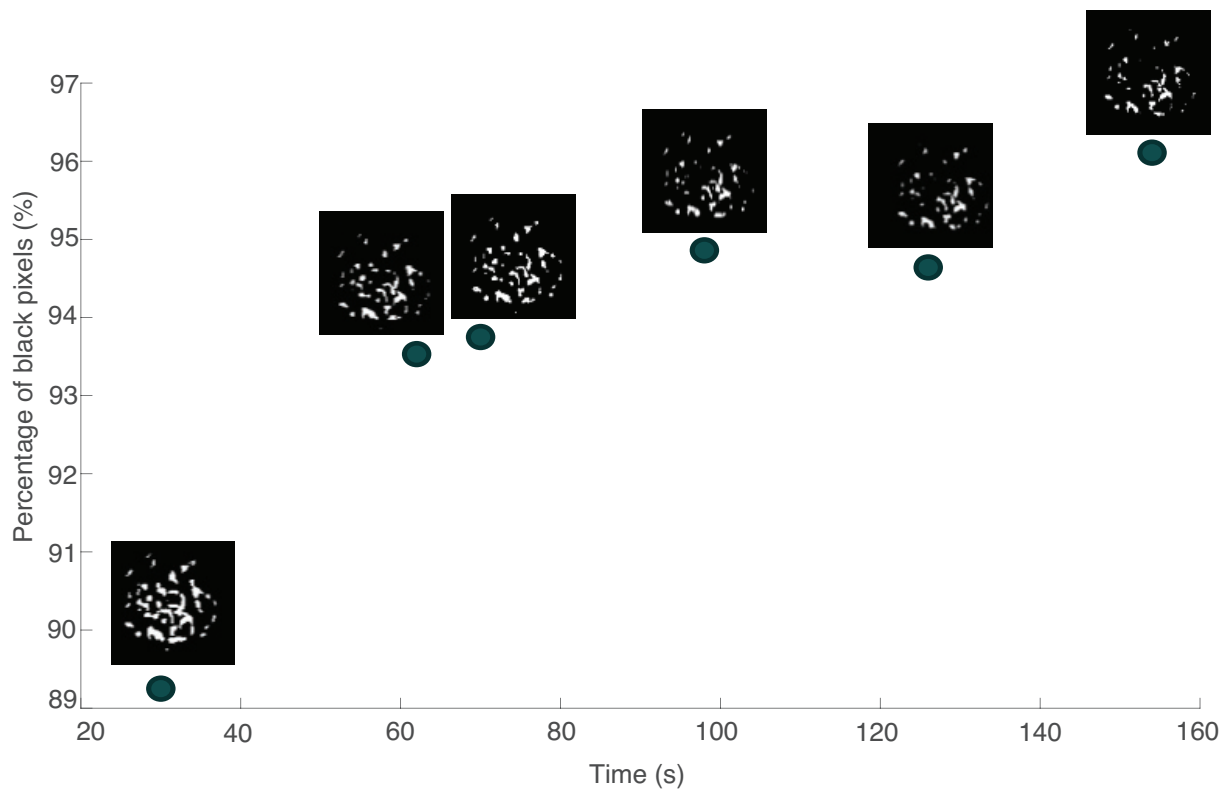


Figure 2.12: Percentage of black pixels with respect to the time passed

a sponge onto a surface. However, it failed to provide precise control over the polishing process within a specific region. This means that the operator had not only to carry the DC motor in place at an appropriate height and distance from the polishing component, but also to monitor its position and correct accordingly the actuating component so as to preserve the rotation and polishing. Removing most of the bar magnets and keeping only one in a vertical or horizontal position reduced significantly the weight of the carrier, but the magnetic torque transmission was reduced or lost, respectively, due to the drop of magnetic forces or the unsuitable configuration of the magnets on the polishing component. With respect to the performance of this method, removing correction fluid using fingers or even nails did not seem to be a more effective way, although it could be considered as an easy-to-do task. Rubbing emery cloth with the operator's hand over the plastic surface, removed almost all the stains, however the normal and tangential force, and shear stress applied using hands were much larger than what the forementioned setup could ever obtain. Also, an undesired blurring was left on the polished surface, along with some remaining stains, while the emery cloth's surface got smoother after the abrasives were worn out during polishing.

The above issues were targeted in the next method and its variant by encasing it in a 3D printed holder for the DC motor with a rotating shaft and a place for the subject surface to sit on at an adjustable height. In this way, the distance between the actuating component

(coupler) and the polishing one (lapper) could be adjusted, and after experimental trials to find an appropriate setting for optimised performance. Moreover, the coupling of the two components of the system was possible via magnetic forces exerted between permanent magnets placed on each component with an altering polarity. The direct coupling method presented in Section 2.1.3 had an operator handling a power supply unit controlling the voltage input to the system and another operator handling the polymer plates' position, since the coupled components could only rotate around the z-axis and no other motion was allowed on the XY-plane.

Apart from the necessity of two operators for the purpose of the proper system functioning, there were other limitations during experimental trials. First, the decoupling effect while handling the voltage input during operation. In particular, the polishing speed could not be increased above a threshold, because the two modules would lose attraction due to the inability of the polishing component to catch up with the actuating component's speed. Another reason that caused the "decoupling effect" was the inertia during accelerating from the initial (zero) speed to the polishing speed. That was occurring for the same reason we had the decoupling effect but at low speeds, with the polishing component being unable to start rotating synchronously with the actuator and eventually losing magnetic attraction to it. Altering the polarity of the permanent magnets was selected in the design phase to offer a chance of recoupling after a potential decoupling of the two components. Although altering polarity was the decided design scheme for both methods presented in this chapter having the above reason in mind, it did not show a proven result in the behaviour of the system with respect to the decoupling effect. Also, the shaft's length might have been suitable for keeping the magnets away from the DC motor, but it created small fluctuations in motion of about 2-3 degrees away from the axis of rotation.

Finally, the OpenCV algorithm we used to edit our live footage and the image processing algorithms to evaluate our methods' performance do not calculate the actual material removal. The OpenCV algorithm could help to estimate the material remaining on the surface, although in some cases it was affected by lighting disturbances (shadows of people passing by, flickering lights) and it required proper adjustments to the settings for optimised filtering of pixels. The image processing algorithms require data preparation that includes proper cropping of images, which means the components of the experimental setup (camera holder, polished surface, polishing base) have to be stable to avoid taking false measurements into consideration. Weighing the polymer plates before and after the polishing process to estimate the material removal rate may offer a more realistic performance evaluation of the method. However, observing the scratches on the polished surface indicates that we can not be absolutely confident that the material removed is the correction fluid and not the polymer plate itself.

2.6 Conclusion

In this chapter, we presented two methods that we developed for remote polishing and they are based on the lapping process used in industry for polishing surfaces. Both methods use remote magnetic actuation to offer the polishing components that we used for this purpose the ability to operate wirelessly. The methods were developed as a proof-of-concept that this is possible and to study the parameters that affect the process's output, finding that the polishing component being able to rotate around its z-axis at $\omega = 16.5rad/s$. The performance evaluation methods shown that they have a potentially high material removal rate, with the weighing method finding $49\mu g/s$, and the OpenCV method $68\mu g/s$, but obtaining a poor surface quality. The instability of polishing components and the difficulty of operation are added to their limitations. In Chapter 3, we present a different method that we have developed to deal with these major issues that were discussed in detail in Section 2.5.

Magnetic field-driven polishing microrobots

” *We are what we repeatedly do. Excellence, then, is not an act, but a habit.*

– Aristotle –

3.1	Introduction	36
3.2	Design and microfabrication methods.	36
3.2.1	SU-8 photolithography	36
3.2.2	Soft-lithography	42
3.2.3	Abrasive-bonded magnetised soft-repliche fabrication.	46
3.3	Discussion.	47
3.4	Conclusion.	49

3.1 Introduction

In this chapter, we describe and present the microfabrication process, and the theoretical modelling of the microrobots we designed for polishing targeted areas of internal metal surfaces. In particular, we describe in detail the mask-making processes, SU-8 photo-lithography and soft-lithography techniques that we used during the fabrication steps for making the microrobots. Finally, we present the fabrication process of microrobots' repliche and composite prototypes that have magnetic and polishing properties.

In contrast with the previous methods shown in Chapter 2, for the prototypes presented in Chapter 3, we used an electromagnetic coil system to produce a magnetic field for the remote actuation of microrobots and the torque transmission. Furthermore, we show demonstrations of their movement in various surface morphologies and we included a further analysis of this method.

3.2 Design and microfabrication methods

In order to access our research's targeted areas, i.e. inner complex manifolds and surface geometries, a different approach was required. We fabricated downscaled models of the previous approaches made of SU-8 (photo-lithography) and Smooth-Cast 327 (soft-lithography) for micro-polishing processes. These models would have the ability to be remotely actuated under an electromagnetic field and navigated through enclosed spaces of complex geometries.

3.2.1 SU-8 photolithography

We used SU-8 photo-lithography techniques for fabricating the microrobot's parts that composed its chassis. SU-8 is a negative photoresist (material sensitive to light) widely used in microfabrication processes because of its properties [67]. Fig. 3.3 shows a schematic of a microrobot model as it would appear with assembled parts of SU-8 encasing a cylindrical NdFeB permanent magnet. This was the initial design, having a shape to fabricate a layer-by-layer chassis encasing a millimetre-scale permanent magnet at their centre. The shapes we used for the initial attempt were discoid, squares, and triangles (see Fig. 3.3) so to try polishing areas of various geometries.

This microfabrication process was selected as the most preferable because it provides high precision of the microscale parts. At the same time, it involves a risk of fabrication failure

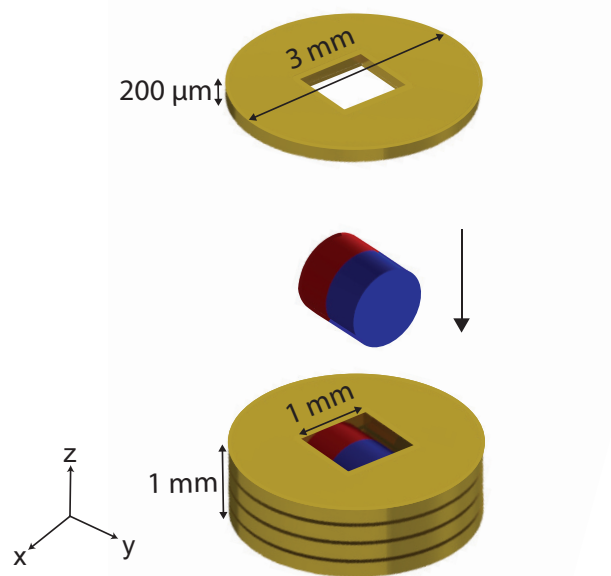


Figure 3.1: Illustration of the assembly process of the microrobot SU8 parts and 1mm cylindrical magnet at its centre

and requires a clean room facility with specialised equipment and training to use. The SU-8 photo-lithographic microfabrication steps were the following:

1. Prepared a lab glass slide by cleaning it with isopropyl alcohol (or isopropanol) (IPA) and dried it by blowing compressed air on it.
2. Cleaned glass slide with distilled water and dried it once again in the same way.
3. Used other cleaned glass slides as aligners of a certain thickness ($200\mu m$) to obtain the preferred thickness for the layers (see Fig. 3.2).
4. Added a suitable amount of SU-8 on the glass slide with a glass rod (see Fig. 3.2).
5. Carefully scraped off the excessive amount of SU-8 with a razor blade along the aligners (see Fig. 3.2).
6. Soft baked on a hot plate at $65^{\circ}C$ for 4 min. Increased at $95^{\circ}C$ and baked for an additional 5 min. Stopped baking and let it cool down.
7. Put the glass slide with SU-8 into UV-KUB 2 (KLOE) tray, covered by a glass plate with the photomask for the exposure (see Fig. 3.3).
8. Exposed sample to UV light using the UV-KUB 2 (KLOE) for 7 cycles of 10s each at full

power with the light source placed at the minimum distance ($10\mu\text{m}$) away from the plate.

- Cleaned out uncured substance on glass slide by putting it in a beaker with SU-8 developer, placed on a shaker at 70 rpm (observing it until the uncured substance was washed away).
- Hard baked at 140°C for 20 min and let it cool down afterwards before removing from the hot plate (see Fig. 3.4(a)).
- Carefully detached the final parts from the glass slide with a tweezers.

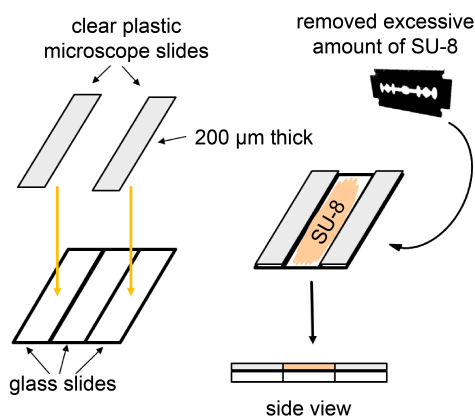


Figure 3.2: Illustration of the process followed for adjusting SU-8 thickness on glass slide

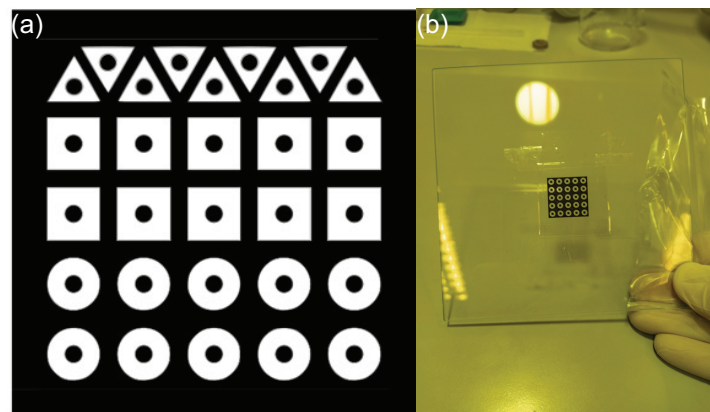


Figure 3.3: (a) The designed mask pattern for trial UV exposure. The outer diameter of discoids and squares'/triangles' edges have a length of 3mm , while the diameter of the inner circular slot is 1mm . (b) The final mask design taped down onto the glass plate

Note that for the preferred thickness of the final parts, alternatively, one can drop a certain amount of SU-8 on a spin coating device. A drawback of the spin-coating procedure is the

excessive amount of material waste per fabrication (approximately 80% of the total amount used [68–70]). Our approach reduced this waste of material, to just 15 – 20% which was only the remaining SU8 on the lab glass rod we used for spreading the SU8 on a glass slide, on the aligning slides and on the razorblade we used for levelling and scraping off the excess amount of SU8. During UV exposure, the use of mask is essential in order to block the light from the areas that we do not want to cure. Hence, while UV exposure only the SU-8 that is not covered will be activated. Fig. 3.3 shows the mask pattern designed and used to activate the SU-8 for the parts fabricated and used to make the microrobot prototypes presented in this chapter. In later designs, the inner circle in the pattern of the discoid was replaced by a square and the orientation of the magnet changed from vertical (poles being parallel to the z-axis) to horizontal (poles being parallel to the xy-plane). Since the polarisation of the magnet was axial, this change of orientation would potentially increase the torque produced by the electromagnetic coil and applied to the encased magnet of the microrobot. Consequently, it would increase its rotational speed and stability on the operating surface (better traction, less shaking behaviours). This improvement in the microrobot's motion was observed during the experimental trials in comparison with the previous arrangement.

We designed the mask patterns used in this project with mask-creating (KLayout) and

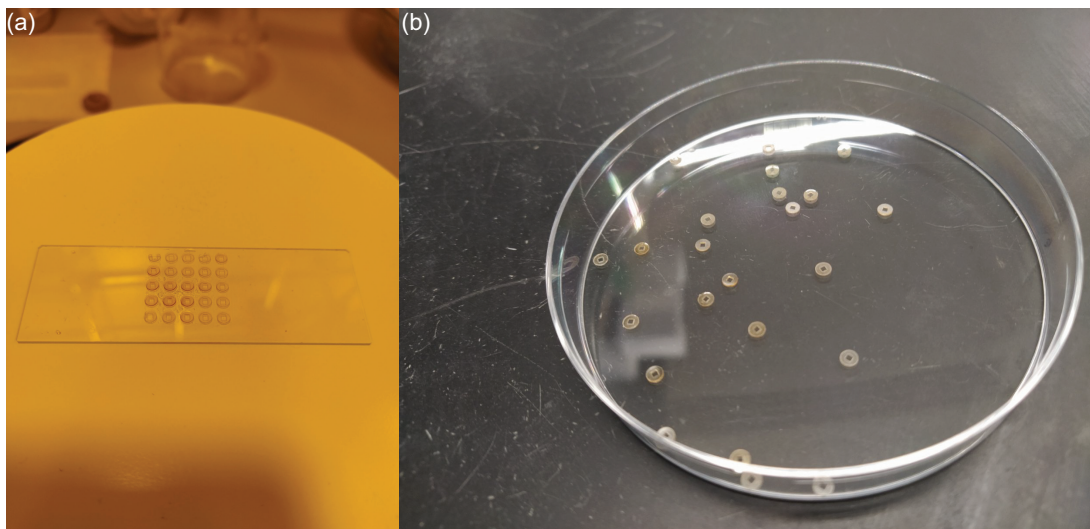


Figure 3.4: SU-8 parts (a) before (on glass slide), and (b) after (in Petri dish) removing phase.

CAD (Autodesk Inventor) software. Then, we edited the designs using image editing program (Adobe Illustrator). Finally, we printed the designs on the harsh side of a printable transparent sheet using a SHARP MX-5141 laser printer with resolution of 1200×1200 dpi. The most important and crucial part of this process is to preserve the dimensions of the desired design for the fabricated parts and final prototype. Even the slightest variations either in the design (dimension inconsistencies), image editing (quality loss during format change or exporting), or printing (low-resolution printer) of the pattern can cause large variations in the final parts'

dimensions in this scale.

After the design and printing stage, we manually cut the final pattern as a small region of the transparent sheet leaving a margin for handling purposes and taped it down on the glass plate. Since the printing phase to the taping down step, everything needed to be done with precision and without touching the pattern at all. We put the glass plate into the UV-KUB 2 tray above the glass slide with SU-8 for exposure to UV light, as described in step 5 of the fabrication process above. Fig. 3.6 shows a microscope image with the top view of the SU-8

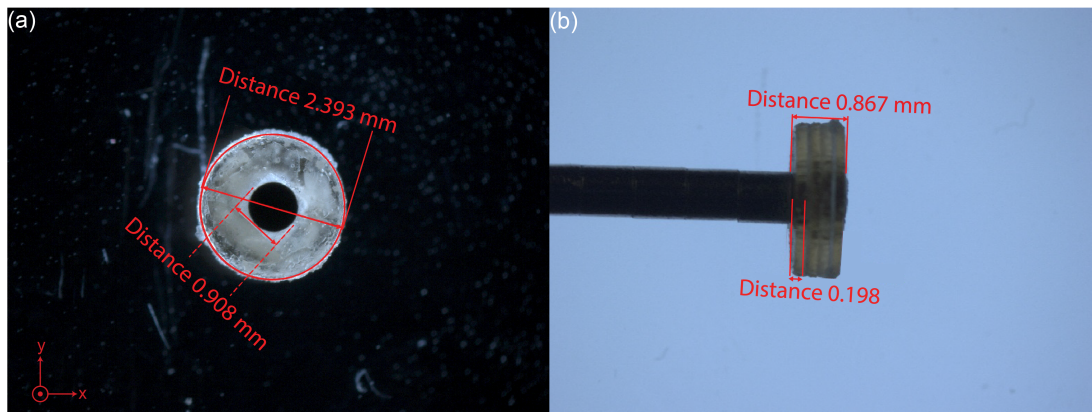


Figure 3.5: (a) Top and (b) side view of the microrobot made of SU-8 parts under the microscope with annotated dimensions.

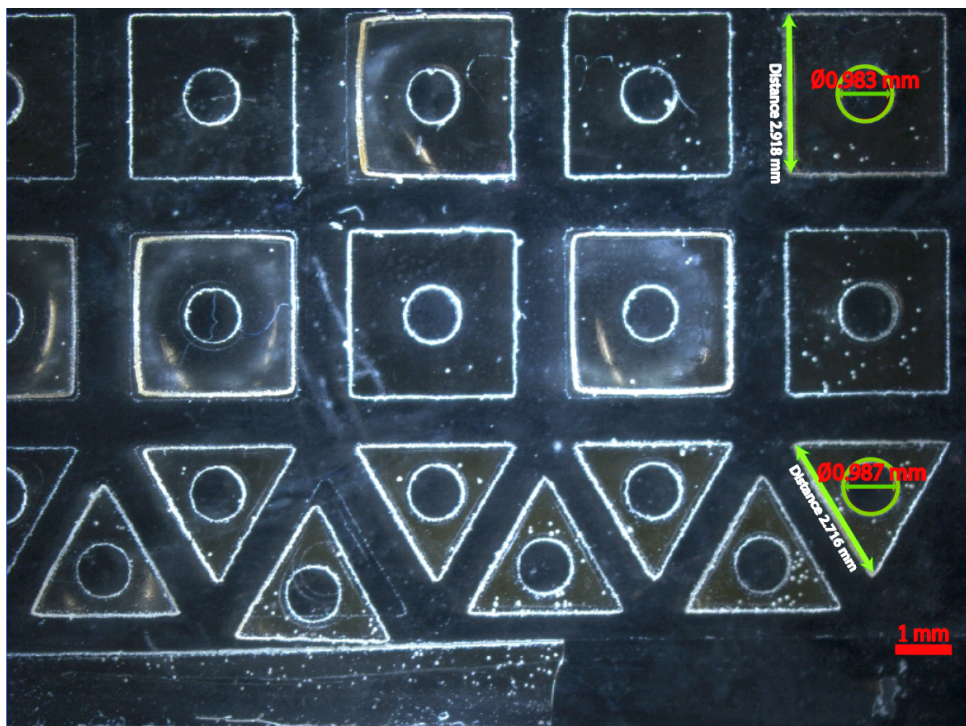


Figure 3.6: SU-8 fabricated parts under the microscope (with annotated dimensions), before being removed from the glass slide.

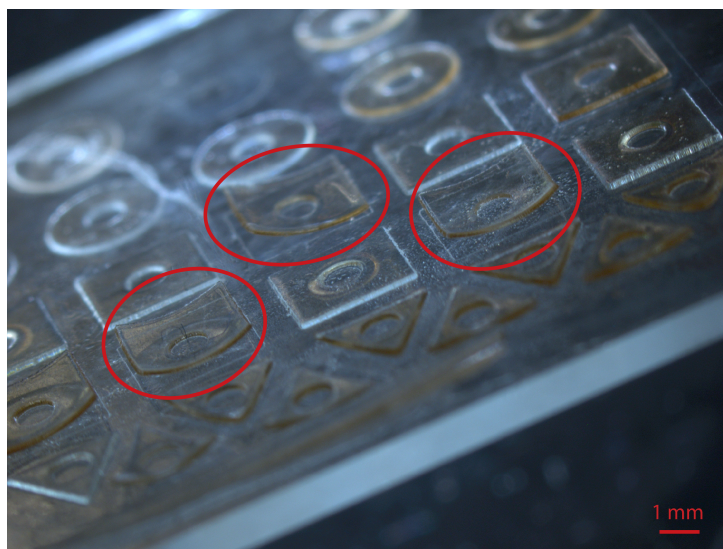


Figure 3.7: Angled view of the warped SU-8 parts before being removed from the glass slide.

parts on the glass slide, while Fig. 3.7 shows an angled view of the glass slide and SU-8 parts under the microscope, presenting the warping effect during baking steps.

For the microrobot's final prototype model, we mainly used discoid parts and we fabricated them solely in the same way as presented above for fabricating various shapes. Fig. 3.4(a) shows the SU-8 parts of the microrobot on the glass slide before removal, while Fig. 3.4(b) shows them after being detached from the glass slide and lying in a Petri dish. Fig. 3.5(a) and Fig. 3.5(b) show the top and side view of the assembled microrobot under the microscope with annotated dimensions, respectively. Finally, Fig. 3.8(a) shows a microscope image of the microrobot after the assembly phase of the SU-8 fabricated parts attached to a rod of cylindrical magnets $\varnothing 1\text{mm} \times 1\text{mm}$, while Fig. 3.8(b) shows it in its physical form sitting on a human finger for comparison.

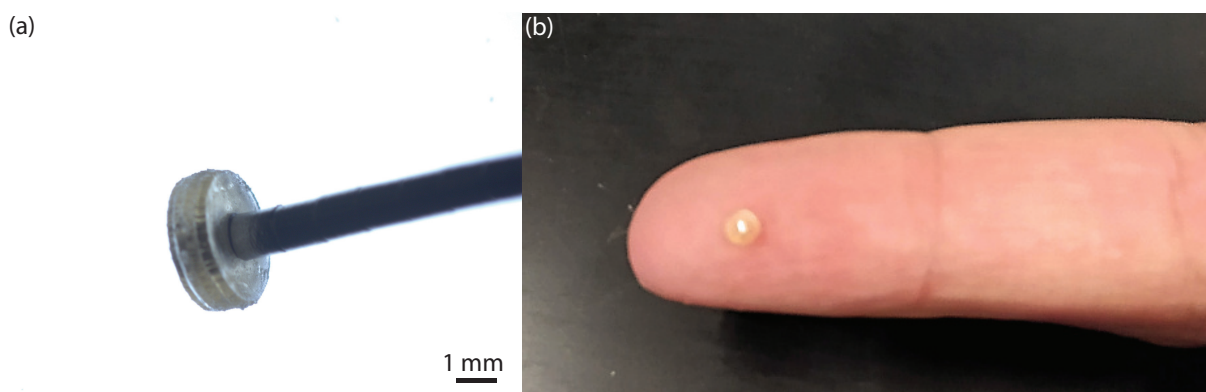


Figure 3.8: (a) Angled view of the microrobot with assembled SU-8 parts and cylindrical magnet $\varnothing 1\text{mm} \times 1\text{mm}$ placed in their centre attached to a rod of magnets for presentation purposes. (b) Final prototype microrobot sitting on a human finger.

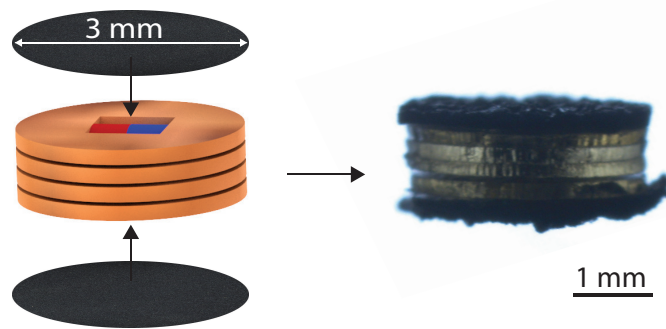


Figure 3.9: Schematic view of the assembly process and physical view of the final microrobot under the microscope. Discoid emery cloth parts are shown as they were glued at the top and the bottom of it.

3.2.2 Soft-lithography

In this section we describe the soft-lithographic techniques we developed and followed to fabricate replicas of the microrobots made of SU-8. The reasons were that soft-lithography offers a shorter duration of fabrication process with a lower failure rate, while it does not necessarily require access to a clean room facility. Moreover, soft-lithography offers fast reproduction of microstructures without the limitations of optical diffraction and with a lower fabrication cost [71]. The main reason in our case was that we could add abrasive powders to the mixture without affecting the final result of the pattern, which is something that can occur in photo-lithography during UV exposure. In this way, we managed to obtain a new composite microrobot prototype made of abrasives and magnetic materials, so to provide our microrobot with polishing properties, while preserving the actuation with electromagnetic coil system. In our fabrication process, we used Mold Star for making a soft mould out of the SU-8 parts or a 3D-printed resin mould. Soft mould was used to replicate SU-8 parts and Smooth-Cast 327 as material for the final composite parts. In the next section, we describe how we mixed Smooth-Cast 327 with Silicon Carbide (SiC) or Aluminium Oxide (Al_2O_3) as abrasives for polishing feature, and Magnetite (Fe_3O_4) or Neodymium ($Nd_2Fe_{14}B$) as magnetic materials for remote electromagnetic actuation. First, we present the techniques we followed during mould-making with the SU-8 parts and the 3D printed resin moulds, and the steps during soft-lithography using the produced soft moulds from the previous fabrication processes.

The steps of the mould-making fabrication process using SU-8 parts were the following:

1. Pour half of the desired amount of Part A component of Mold Star into a lab mixing dish that sits on a high-precision scale (see Fig. 3.10(b)).
2. Pour an equal amount of Part B component of Mold Star into the dish and mix the two

components away from the scale.

3. Slowly pour the mixture onto the glass slide with SU-8 parts (parts were not detached from the glass slide after the photo-lithography process for this purpose) (see Fig. 3.11(a) as an example of illustration).
4. Let the mixture slowly spread across the glass slide and over the parts as uniformly as possible (to obtain a stable base on the top).
5. Used a desiccator to remove enclosed air (as bubbles) from the mixture.
6. Let it stand until it is cured (time varies with sample size).
7. Remove from the glass slide by carefully cutting the edges with a razor/cutting blade and slowly peeling it off.

For ease during Steps 3-5, we could have used a 3D-printed frame around the glass slide to set the mould's boundaries. In this way, the mixture would have been uniformly distributed on top of the parts to replicate and obtain a more decent mould. Finally, by removing the frame, Step 7 would have also been performed more easily and less possible to accidentally break the mould.

Following are the steps of the mould-making process using high resolution 3D printed resin moulds, which we designed and fabricated for this purpose:

1. (Optional) To avoid unnecessary waste of materials during fabrication, it is suggested to measure/estimate the final volume of the mould by calculating the empty/inner part of the 3D printed design to be used for moulding (see Fig. 3.10(a)).
2. (Optional) In case a weighing scale is used for measuring, it is necessary to calculate the total mass of mould needed using the density of the material that is going to be used for the fabrication. Alternatively, a volumetric pipette can be used knowing the total volume from the previous step.
3. (Optional) Spray the inner surface of the mould with a release agent (e.g. Ease Release 200) so the soft mould can be easily removed from the mould after curing.
4. Pour half of the appropriate amount of Part A component of Mould Star into a lab mixing dish that sits on a high-precision scale.

5. Pour an equal amount of Part B component of Mould Star into the same lab mixing dish and mix the two components away from the scale.
6. Slowly pour the mixture into the mould letting it spread uniformly from its centre.
7. Use a desiccator to remove enclosed air (forming bubbles) from the mixture.
8. Let it cure for approximately 4-6 hours (time varies with mould size, surface area, and air ventilation).
9. Carefully remove the cured mould by slowly rubbing its surface with your fingers while wearing Nitrile gloves. Occasionally, it might be necessary to cut through the edges with a razor/cutting blade to make a gap or detach it from the 3D printed mould's inner surface.

Note that using release agent during Step 3, made our parts lose their shiny glossiness that they normally had on the upper surface. In our case, we decided not to use it in our fabrication, due to this complication. Not applying release agent, does not necessary lead to moulds being stuck in resin, not being removable easily or breaking during removal process. However, depending on the 3D printed mould design used, similar unwanted scenaria are possible to occur.



Figure 3.10: (a) 3D printed mould used for mould-making using soft-lithography.(b) Mold Star Parts A & B prepared to pour into mixing dish placed onto a precision scale

Finally, we used Smooth-Cast 327 for the soft-lithography process, using soft moulds to fabricate our repliche, following the next steps:

1. Poured an appropriate amount of Part A and Part B components of Smooth-Cast 327

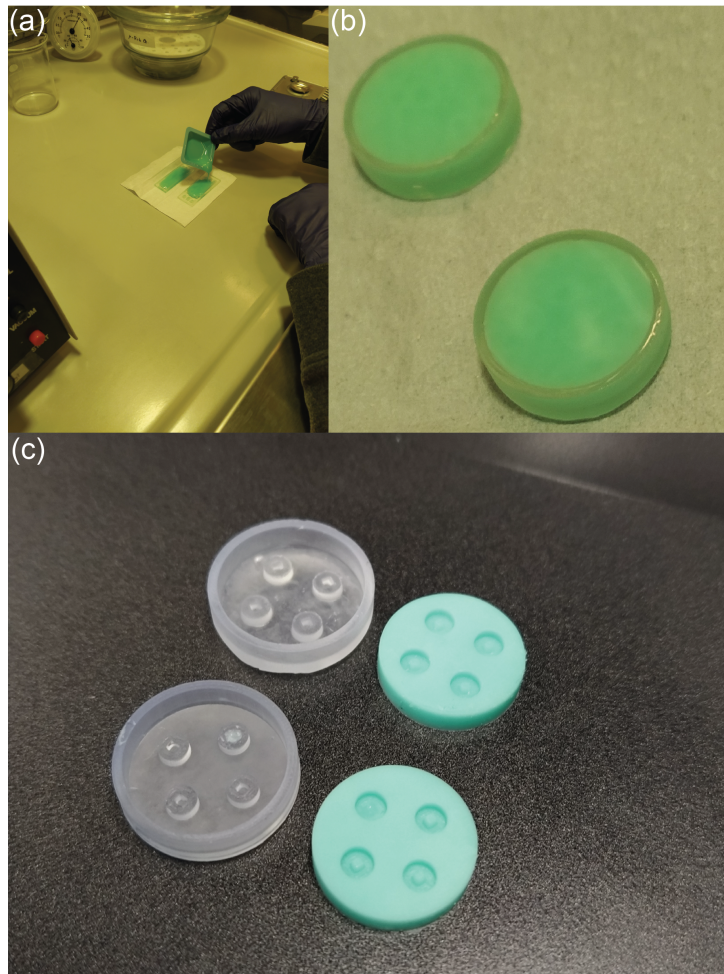


Figure 3.11: (a) Fabrication process that demonstrates how Mold Star mixture was poured into a 3D printed resin sample mould. (b) Mold Star moulds let to cure, and (c) soft moulds after removed from 3D printed resin moulds.

into a lab mixing dish and softly mix them together.

2. Filled up the soft mould made by following the previous process and scraped off any excess amount from the top of the mould using a wooden tongue depressor.
3. (Highly recommended) Used a desiccator to remove enclosed air (as bubbles) from the mixture.
4. Let it cure (usually 2-4 hours, depending on the mould size, surface area in direct contact with the air, and air ventilation).
5. Carefully removed parts from mould by folding/bending the mould and/or using a tweezers.

After the above fabrication process, we could place a magnet inside the replica since it was a solid part having a slot identical to the one in the design composed of the SU-8 layers (see Fig. 3.13). The placement process is trivial, unlike the hard and delicate process of the layer-by-layer assembly of SU-8 parts, which also involves a high risk of breaking the parts.

3.2.3 Abrasive-bonded magnetised soft-repliche fabrication

In this section we present a novel fabrication process for creating composite repliche with abrasives and magnetised particles. Smooth-Cast 327 was mixed with either Silicon Carbide (SiC) or Aluminium Oxide (Al_2O_3) as abrasives for the polishing feature, and either Magnetite (Fe_3O_4) or Neodymium ($Nd_2Fe_{14}B$) as magnetic materials for remote electromagnetic actuation. Every replica we fabricated with Smooth-Cast 327 and Aluminium Oxide abrasive powders is very hard and durable compared to the layers made of SU-8 and also has the ability to be used for polishing since one of their surfaces is not smooth plastic. Finally, the repliche we made of Silicon Carbide have an even more rough surface than the ones made of Aluminium Oxide making the abrasive type the preferable option for later fabrication processes.

The steps of this fabrication process were as follows:

1. Poured equal amount of Part A and Part B components of Smooth-Cast 327 into a lab mixing dish and softly mix them together.
2. Using a small tool with a wide tip like a wooden tongue depressor, we added abrasive powders (SiC or Al_2O_3) three times the weight of the Smooth-Cast 327 mixture, and then we mix them all together until it forms a dense paste.
3. Applied the paste on the soft mould with the wooden tongue depressor in a way similar to a building trowel.
4. Used a desiccator to remove enclosed air (as bubbles) from the mixture.
5. Scraped off excessive amount using the wooden tongue depressor or a razor blade.
6. Let the mixture cure (normally around 4 hours).
7. Carefully removed parts from mould by folding/bending the mould.

Fig. 3.12(a) shows the repliche parts cured in the soft Mold Star moulds before removal and Fig. 3.12(b) the part after removal sitting on a human finger for size comparison.

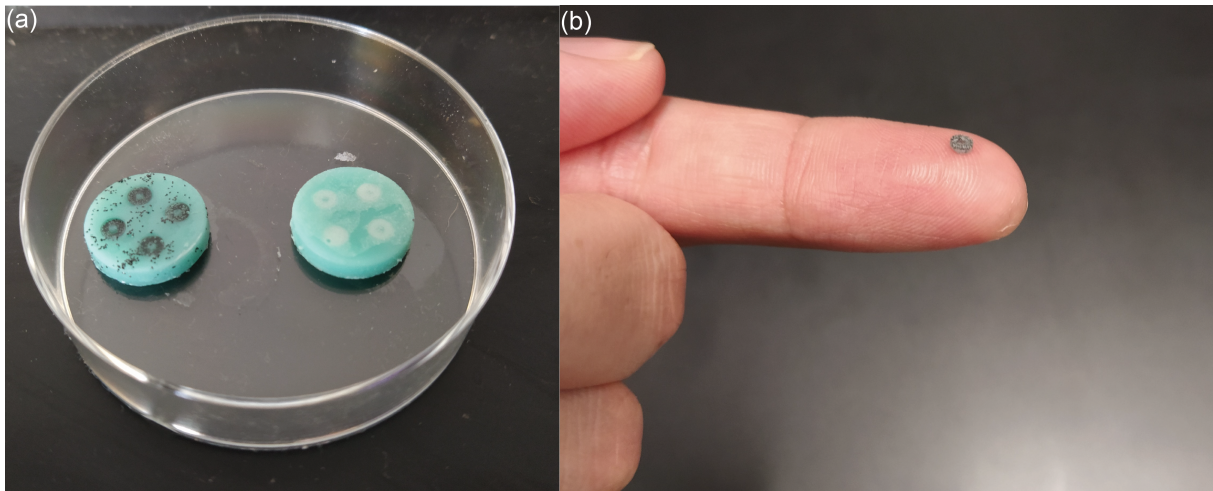


Figure 3.12: (a) Soft microrobots' chassis repliche carrying abrasives bonded with Smooth-Cast 327. Parts in the left mould have Silicon Carbide (dark grey abrasive particles), while parts in the right mould have Aluminium Oxide (white abrasive powder). (b) Removed part sitting on a human finger

Microscope images shown in Fig. 3.13 present the square-shaped microrobot made of Smooth-Cast 327 parts fabricated with the process described above in comparison with the one made of SU-8. Variations in the dimensions are due to the soft-moulding fabrication.

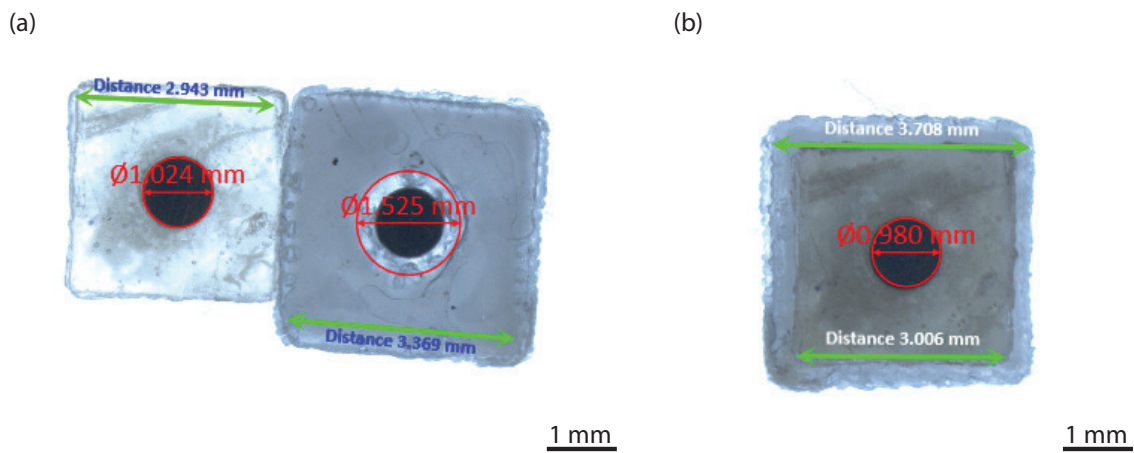


Figure 3.13: Replica microrobot made of Smooth-Cast 327 sitting (a) on the right to and (b) below the one made of SU-8 for comparison.

3.3 Discussion

In this chapter we presented the microfabrication processes followed to obtain the microrobots for electromagnetic remote actuation. Trying to overcome the limitations of the

systems presented in Chapter 2, we designed various shapes for SU-8 microfabrication of microrobots. Although the fabricated structures were able to be remotely actuated using an electromagnetic coil system, their microfabrication process has many drawbacks and requires extreme care during all steps to obtain the desired result.

In particular, during the spin coating or manually spreading the desired SU-8 quantity on the working substrate (e.g. glass slide), its uniform distribution is really important so the fabricated parts can be identical in the end. Also, during the soft-baking phase, selecting the appropriate temperature to evaporate most of the solvents in the SU-8 and prepare it for the hard-baking step. In our case, the first microfabrication process went smoothly with the final parts being relatively solid after all steps. Unfortunately, further repetitions of the process for fabricating more parts did not go as expected, because our SU-8 layer was warping during the hard-baking step. Parts were curving even halfway through the baking phase, being detached from the glass slide, and breaking, even though we were following the same steps as in the first time. Later on, it came to our realisation that during the first fabrication, the only difference was that the glass slide we had used had been plasma treated prior to its use by another user. This led us to the assumption that SU-8 was attached to the glass slide and could not be detached during baking to warp. However, we have not validated this assumption because it required further training of using the plasma coater and we already started working on fabrication of repliche with soft lithography. Other reasons that the warping could have been occurring are that the SU-8 amount was not enough or uniformly distributed on the glass slide surface, the temperature or the duration of soft baking had to be increased (suggested 95°C), or even the UV-exposure time had to be increased too.

Changing the orientation of the encased cylindrical magnet increased the rotational speed and reduced the wobbling motion of the microrobots, due to better alignment of magnet's poles with the electromagnetic field. However, this involved many difficulties during the assembly process of the microrobot's SU-8 discoid parts. Since the whole assembly process was handcrafted required patience and precision in motion. In order to place the parts into place encasing the cylindrical magnet, we made a rod of magnets as a guiding axis for the discs. Evaluating our method we could have used just a single rod of magnetic material with a single magnet on its tip instead. With our method, we had difficulties holding a series of magnets in place due to their geometry, because they were slipping off due to magnetic forces between them.

In the fabrication of the SU-8 parts, selecting the proper settings during the UV exposure phase was the most crucial step. More specifically, the short distance of the lens from the mask (10 μ m) led to high precision in the dimensions of the final parts, so the \varnothing 1mm cylindrical magnet could not fit at their centre. Hence, for the purposes of repeatability, either some tolerance in dimensions during design needs to be provided, or a greater distance

from the mask needs to be set during UV exposure to balance the precision in a "strict-to-dimensions" design. To deal with these small imperfections in the parts we used a model-craft mini rasp to carefully trim their centre, by softly rotating the tool inside them until the magnet can fit through them.

Making soft repliche with abrasives involved some problems as well. Specific steps during fabrication led to unwanted results (cavities, non-uniform structures, uneven surfaces) and the process had to be redone from the start. The step that caused most of the inconsistencies to the fabrication process was desiccating the parts in the mould after pouring the Smooth Cast 327 and adding abrasives. The desiccator was dragging the air/bubbles to the top of the mould to be released, causing also a raise/removal to an amount of abrasives. More specifically, almost all of the mixture was coming out of the mould wells in the form of foam, leading to parts with cavities and holes after curing. To deal with this problem eventually we stopped using the desiccator during the fabrication process, but let the particles sit in the mixture and the air be enclosed in the final parts.

Another issue was keeping the exact dimensions of parts during the design phase of the moulds, which led to no proper fitting of the permanent magnet at their centre. The SiC parts were made using a new mould design (1.2mm thickness) in a clean room facility adding release agent, while the Al_2O_3 parts were not made in a clean room facility and we used the old mould (1mm thickness) without the use of any release agent. Finally, the fabrication processes of composite microrobots with abrasives (SiC , Al_2O_3) and magnetic particles ($Nd_2Fe_{14}B$, Fe_3O_4) did not include use of any release agent, nor use of desiccator and the final parts could be easily removed by folding the moulds and picking them out or just letting them fall.

3.4 Conclusion

In this Chapter, we presented another approach we developed for remotely polishing unreachable areas using magnetically actuated microrobots able to access, reach, and perform the polishing process at a desired location. We fabricated the microrobots we used for our experiments following various existing technologies and others developed for the purposes of this project, and we presented them all in detail. The fabrication steps of every technology, their settings, and the parameters that we picked were all described and their effects were explained in the Discussion section of Chapter 3. The results shown that our fabricated microrobots can access unreachable areas with passages of diameter down to 4mm and travel rolling through them. However, square and triangle microrobots experienced difficulties moving on surfaces with cavities. We decided to present these findings in Chapter 4 along with

the actuation and localisation methods.

Remote actuation and localisation methods

” *Speculation and the exploration of ideas beyond what we know with certainty are what lead to progress.*

– Lisa Randall –

4.1	Introduction	52
4.2	Magnetic actuation with electromagnetic coil system	53
4.3	Point-to-point localisation method using vibration sensors	55
4.4	Results	58
4.5	Discussion	66
4.6	Conclusion.	66

4.1 Introduction

Using microrobots to access and operate in complex geometries can offer a controlled polishing process, to obtain the desired result in terms of surface quality and morphology of the inner structure. To preserve a smooth operation and obtain a uniform result, the microrobot needs to be constantly controlled during polishing. This means efficient control algorithms handling the operation should require online unceasing feedback of the microrobots' configuration inside the structure at the specific point of interest. Microrobots that can not be localised efficiently to preserve their functionality, can not consequently show great polishing performance when applied in complex manifolds. At unreachable areas targeted by the polishing microrobots proposed in this project (confined spaces and passages of $\varnothing 7 - 10mm$), visual feedback can not be currently achieved by any means or it is limited to cable cameras that cannot easily or fully inspect confined morphologies having sharp turning points and passage edges, corners, hidden or blind spots and any other structure with similar geometrical constraints due to morphological complexity [72].

Localisation methods played a significant role in robotics development over the past decades and improved their performance during operation. Feedback from a robot's environment helps an operator to guide the robot to a desired location and perform desired tasks itself or remotely through the operator, based on the environment's condition and morphology. Visual and acoustic feedback have been used by simultaneous localisation and mapping (SLAM) algorithms to localise robots exploring dangerous/hazardous areas humans should avoid accessing (e.g. destroyed nuclear power plants, contaminated areas, collapsed buildings due to earthquakes or actions of war, etc), in the modern automotive industry (self-driving cars), and in not-necessarily-hostile environments (air, underwater). In microrobotics, localisation is also of great importance for the proper and effective/successful operation, since the tasks that are carried out usually require extreme precision in sub-centimetre scale environments.

Nevertheless, localisation methods in robotics can not be directly applied in microrobotics research or applications due to the challenges they face when applied. In particular these challenges can be classified in the following categories:

- Down-scaling sensors used for localisation, because their functionality or performance can vary due to their size change. At the same time, reducing their size is crucial for the microrobots' operation in the environment of application [73, 74].
- Computing power of microrobots can be prone to computationally complex localisation

algorithms due to size limitations, especially during online data transfer and computations for better accuracy.

- Navigation inside environments of sophisticated geometries that are used in automotive/aerospace industry, where GPS or external sensors for localisation may not be applicable, is also a challenging obstacle to overcome.
- Algorithmic design of localisation techniques should be really efficient to deal with the power consumption of the microrobot because there are potential limitations due to its size. This may involve trade-offs between accuracy, computational complexity, and power efficiency [74].
- Limited bandwidth or poor communication while the microrobot is receiving and transmitting data can also cause trouble during localisation and significantly affect their operation.
- Errors due to sensor inaccuracies, calibration errors, drifting over time, sensors' sensitivity can lead to a dramatic drop in localisation method's accuracy [75]. Additionally, implemented electrical noise to sensors' readings during sensing is another obstacle, e.g. hall-effect sensors or compasses inside magnetic fields [76].

The localisation methods that were developed for this particular project had also some critical challenges to overcome, but some of the above challenges were avoided because of our approach advantages. By using magnetically actuated microrobots with no sensors onboard we managed to overcome the challenges of power consumption, computational complexity, miniaturisation of sensors, and communication problems. Nevertheless, we had to deal with the challenges of obtaining reliable localisation data (spatial and temporal resolution) and localising despite the varying speed of the microrobot when needed.

This chapter presents the results obtained using our magnetic actuation method and a localisation method using vibration sensors to locate and navigate the microrobots that were fabricated and presented in Chapter 3.

4.2 Magnetic actuation with electromagnetic coil system

In order to actuate our microrobots under a magnetic field, we magnetised the NdFeB composite parts passing them through a strong magnetic field (radial magnetisation), using a custom 3D printed case we designed to keep them in the desired orientation during

magnetisation. We used a Gaussmeter to measure the magnetic field strength produced by every coil: approximately $1.3 \pm 0.05 mT$, while the NdFeB composites' magnetic field strength was measured $3mm$ away from the pole and found to be $0.140 mT$. Hence, the maximum magnetic torque that can be produced is $\tau \approx 2.08 \times 10^{-9} Nm$.

All the fabricated microrobots we presented were able to operate remotely using electromagnetic actuation means. In particular, we used an electromagnetic coil system with four inclined (45°) coils and one parallel to the horizontal plane, all lying beneath the workspace (see Fig. 4.1). The electromagnetic coil system uses Sabertooth $2 \times 32A$ (dual channel) motor drivers, each one of them powering two coils. An Arduino Esplora was used to control the motor drivers and navigate each of the microrobots on the workspace. The actuation algorithm was pre-written in Arduino Integrated Development Environment (IDE), but modified based on the Supplementary Material for the work presented in [77] by Miyashita et al.

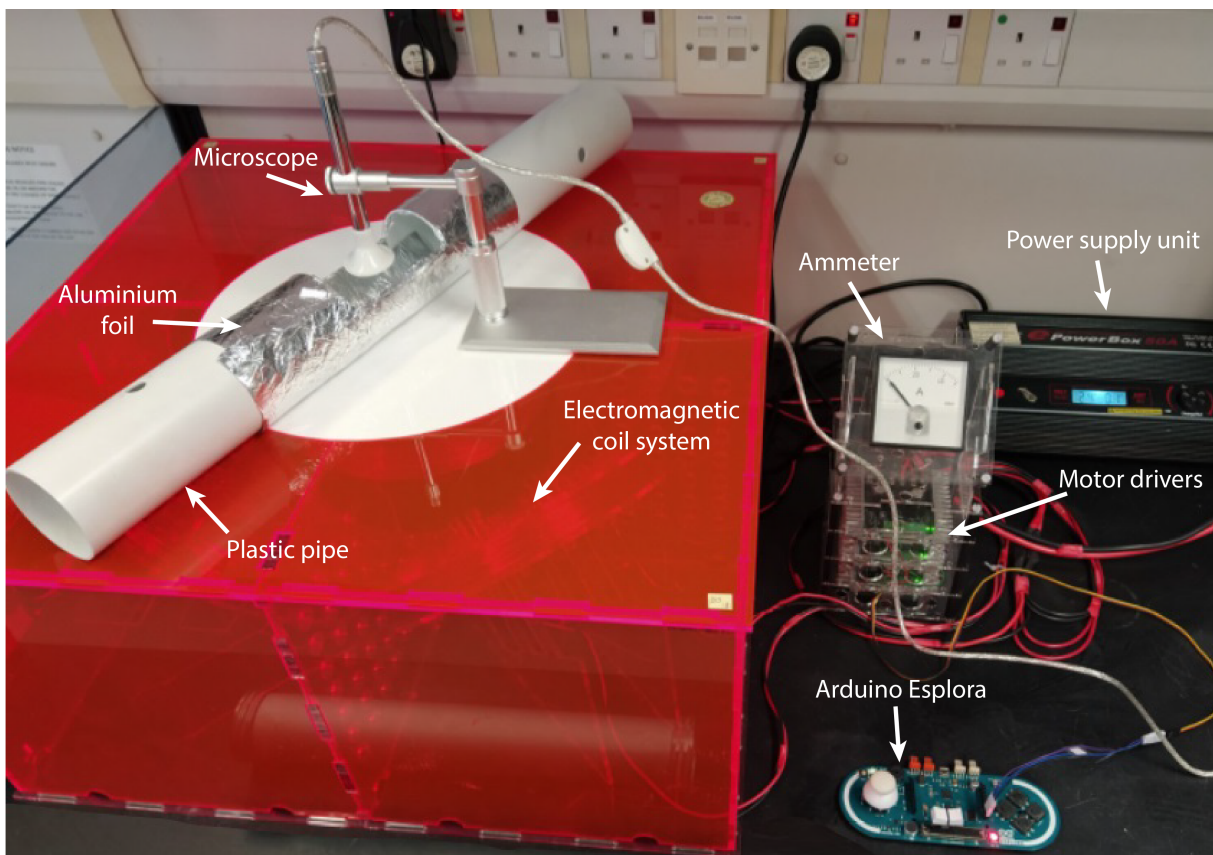


Figure 4.1: Physical view of the experimental setup used during trials on metal parts

We tested the microrobots' behaviour on metal parts such as aluminium plates (circular-shaped microrobot), copper plates (triangular-shaped microrobot) and melted aluminium with cavities (square-shaped microrobot)(see Fig. 4.2). This was to conclude that the corners of triangular and square-shaped microrobot designs would cause problems in motion inside

structures with surface anomalies (getting trapped into cavities, or stuck in obstacles). Although their geometries could be appropriate for polishing corners or edges with oscillating motions, our prototypes can not produce enough shear stress to perform such a task.

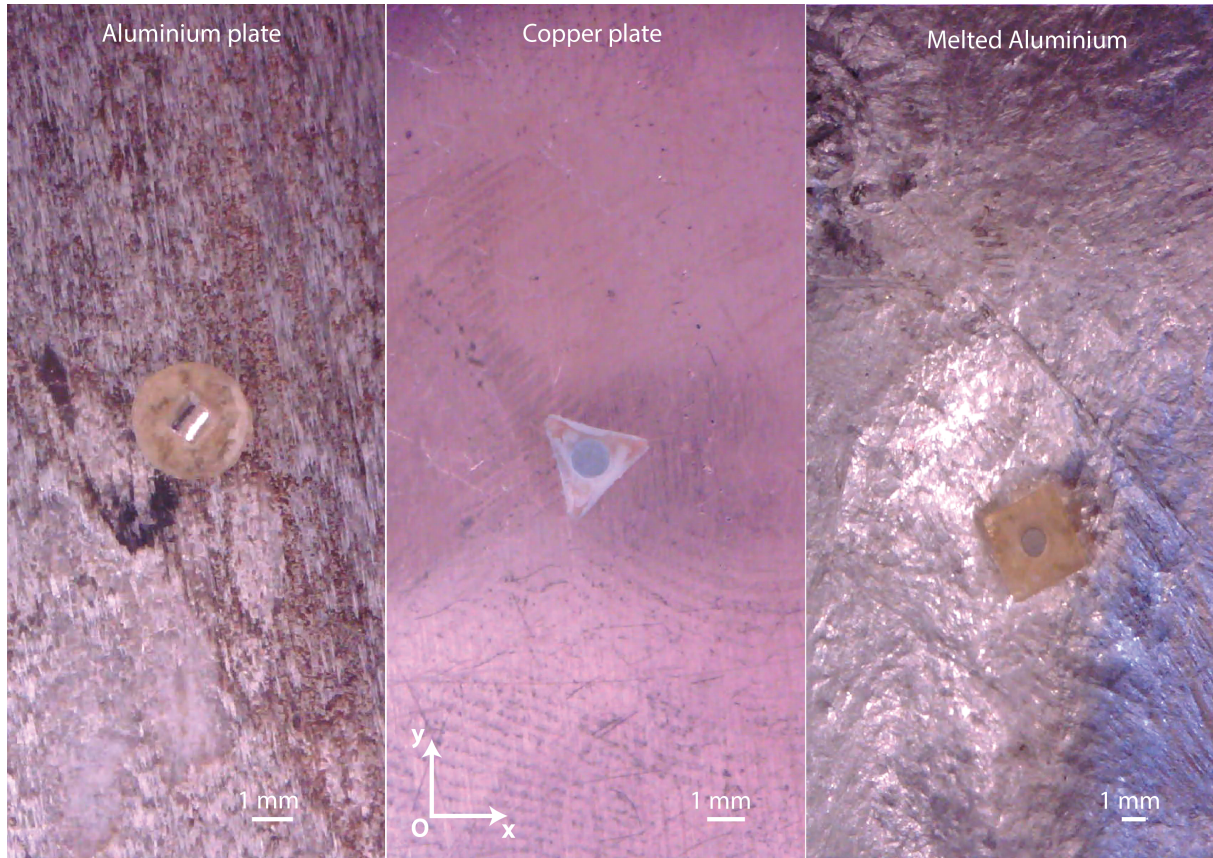


Figure 4.2: Microscope snapshots of different microrobot variants during operation on metal parts

4.3 Point-to-point localisation method using vibration sensors

In this particular method we used an array of ceramic piezoelectric vibration sensors attached to the subject structure to detect the presence of our microrobots on the inside. In order to calibrate the sensors and test their accuracy, we used them in pairs placed 10cm apart on an aluminium sheet and we recorded the sensors' readings from a vibrating motor device applied on the other side of the plate. Analysing the readings from the sensors we estimate the position of the motor on a single line (1D-localisation). Fig. 4.3(a) shows a top view of the microrobot placed on the aluminium surface on the 10 cm line we used for trials. Fig. 4.3(b) shows the side view of the experimental setup we used to actuate the microrobot. We used a 4-Phase Stepper Motor actuated by a ULN2003 motor driver board connected

to an ELEGOO MEGA board. The motor was used to rotate a circular magnet attached to a pencil and this was rotating the microrobot around its y-axis (pitch motion) on the aluminium surface. The range was picked so the microrobot could be inside the magnetic field of the circular permanent magnet. Rotating to one direction could pull the microrobot to one end of the line, while the opposite was pushing it to the other end.

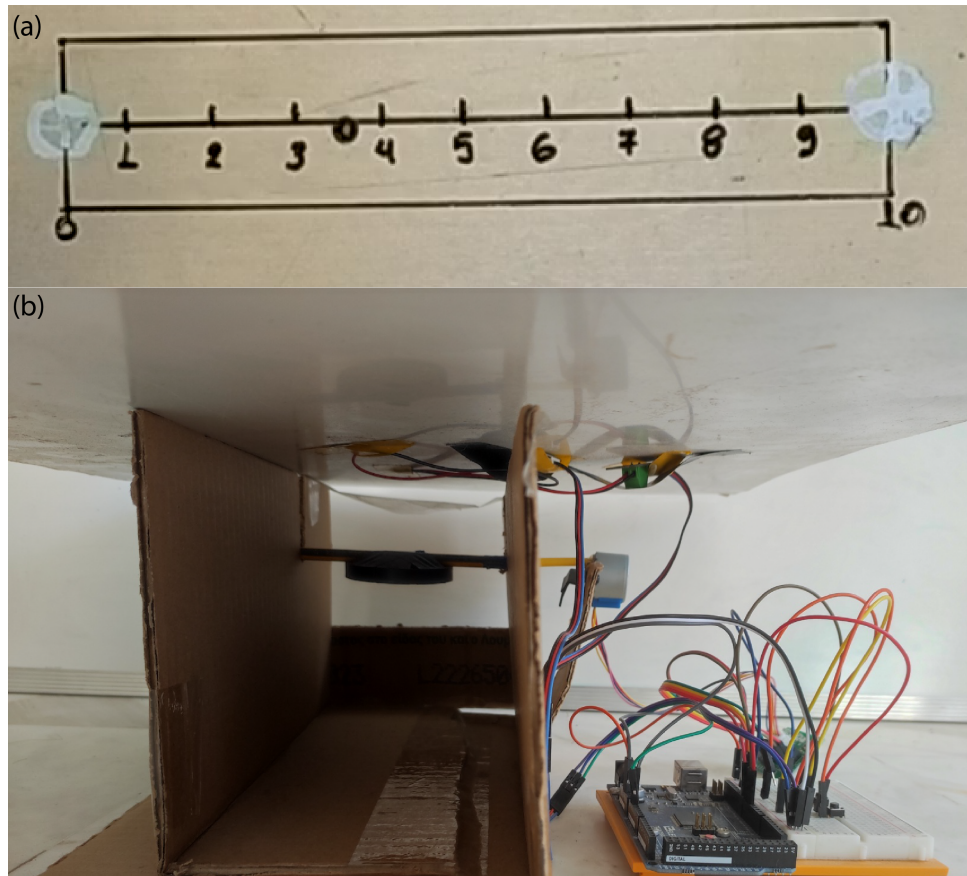


Figure 4.3: (a) Top and (b) side view of the setup we used to calibrate the two vibration sensors attached on an aluminium sheet.

The experimental setup we used in this method with the vibration-sensors array is shown in Fig. 4.4. We used five analog piezoelectric ceramic vibration sensors (Keystudio KS0272) to make the array. The ceramic plates of each vibration sensor had a diameter of were passed through a Dura-Lar sheet that was cut using a vinyl cutter. The pattern we used to cut it was designed in such a way to hold the sensors without using any glue or tape to keep them in place. That was to decrease the probability of breaking or harming the ceramic plates during use, but preserve their sensing ability wherever the Dura-Lar sheet is attached to. A close-up of the sensor array is shown in Fig. 4.5, demonstrating its functionality. The Dura-Lar sheet was then attached to a plastic pipe of 0.5cm thickness, to test the sensors' capabilities while a magnet is moving on the other side of the pipe.

Fig. 4.6 shows snapshots of captured footage of a 4mm cylindrical magnet rolling inside

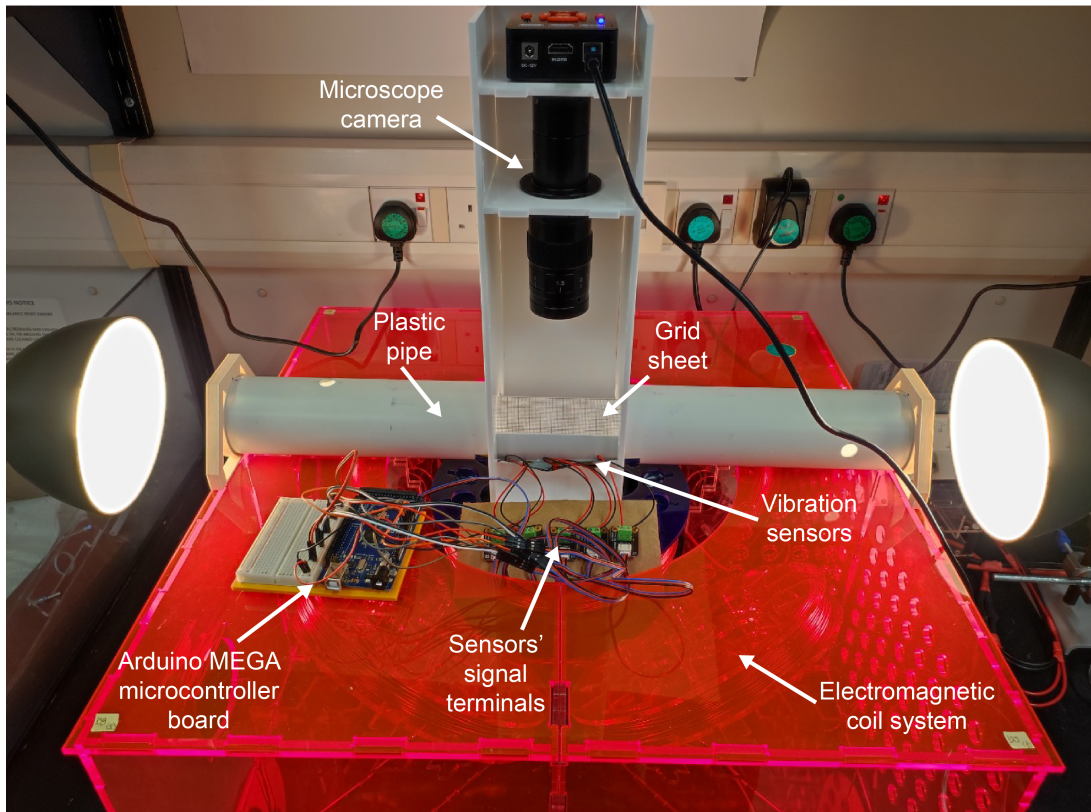


Figure 4.4: Experimental setup with vibration sensors attached to the plastic pipe where a permanent magnet was rolling in

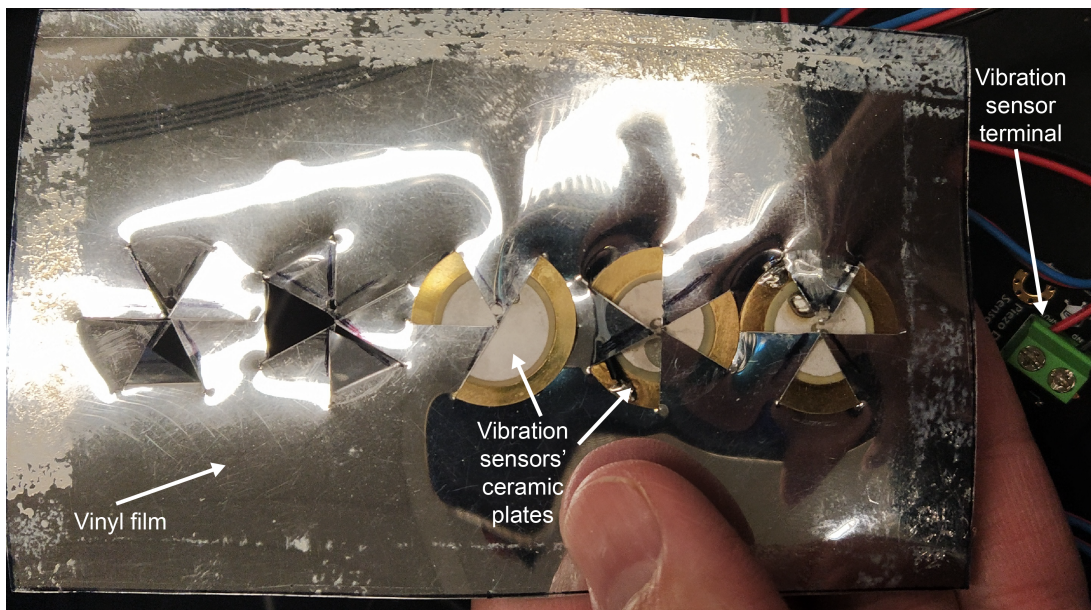


Figure 4.5: Vibrations sensors placed on a Dura-Lar sheet cut with a pattern to hold the sensors in position

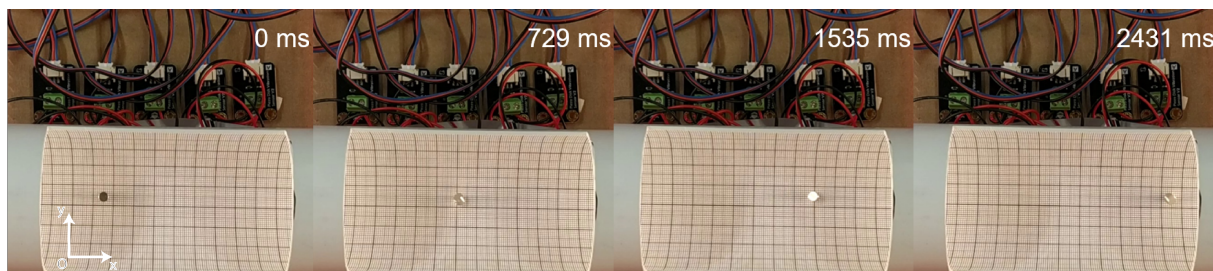


Figure 4.6: Snapshots of a 4mm cylindrical magnet rolling inside the plastic pipe to calibrate the vibration sensors

the plastic pipe we used in our experimental setup to calibrate the vibration sensors and test their sensitivity. With the experimental setup and equipment used we could have 20 readings per second via the Arduino IDE serial monitor. However, this frequency dropped when we used Mathworks MATLAB interface for communication with the microcontroller.

4.4 Results

We gathered all data by analysing footage captured during experimental trials with a motion tracking software. In particular, we measured the angular velocities (rotation around their z axis) and pitching speed (rotation around their y axis) of our microrobots that we fabricated with the process described in Subsection 3.2.3, and they are shown in Table 4.1. The SU8 discoid microrobot was operating on an aluminium plate, its triangular variant on a copper plate, and our magnetised soft microrobot with abrasives on an acrylic surface covered with soaped water to overcome friction forces exerted due to their materials' adhesion. The angular velocity of the discoid could not be measured precisely with the captured footage, because it was not captured with a high speed camera and the angle of rotation could not be identified in each frame to track it using the same method. However, we could provide a rough estimation of it, by observations, being around twice as large as the triangular one. We have also provided the measured values of the lapper's angular velocity and a 3mm cubic magnet's pitching speed for comparison.

We see that the highest rolling speed was 16.6mm/s and it was obtained by the SU8 discoid microrobot, being close to 66% of the speed obtained by a rolling 3mm cubic magnet. This is reasonable since our discoid SU8 microrobot is lacking magnetised mass, which would potentially increase the magnetic forces applied to it under a magnetic field and consequently its speed. The triangular shaped microrobot did not have a suitable geometry to assist its movement and we notice a drop of 33% to its speed compared to the discoid shape.

Table 4.1: Angular velocity and rolling speed of microrobots

Prototype model	Angular velocity (rad/s)	Rolling speed (mm/s)
SU8 discoid	N/A	16.6
SU8 triangular	14.2	11.0
Abrasive microrobot	10.0	9.0
Lapper	16.5	N/A
Cubic magnet (3mm)	N/A	25.0
Cylindrical magnet (4mm)	N/A	38.5

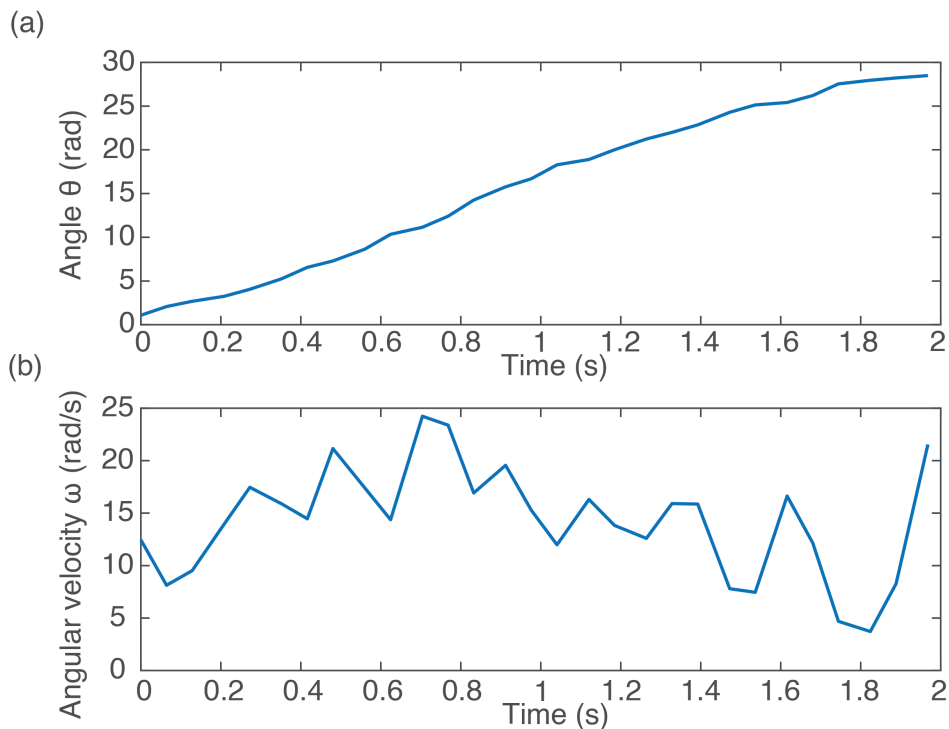


Figure 4.7: (a) Angle and (b) rotational speed of the SU8 triangular microrobot with respect to time

Finally the abrasive-bonded magnetic microrobot could not achieve a greater speed due to its poor magnetisation of its particles, unlike the permanent magnets that were placed in SU8 microrobots. In terms of the angular velocity, we can see that the one obtained a value close to the lapper was the triangular shape with 14rad/s and the minimum one being again the abrasive-bonded microrobot.

Fig. 4.7 and Fig. 4.8 show the rotational speed of the SU8 triangular microrobot and the abrasive-bonded soft microrobot, respectively, derived from the angular distance travelled over time. We decided to include the angular distance θ for better visualisation and understanding of the microrobot's motion.

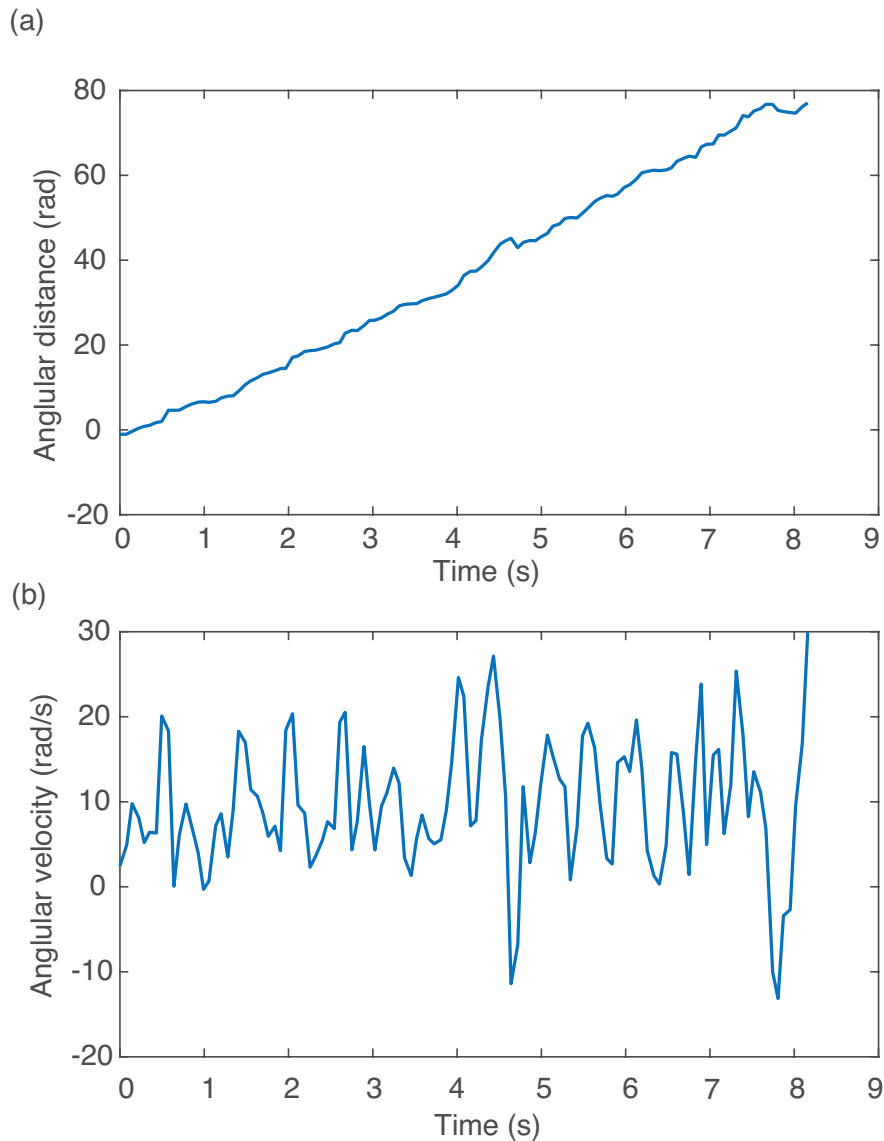


Figure 4.8: (a) Angle and (b) rotational speed of the abrasive-bonded microrobot around its z axis with respect to time

The results shown that our fabricated microrobots can rotate around their y axis to move through narrow passages with minimum average speed of 9mm/s carrying abrasives and access unreachable sites and blind spots. Additionally, they can rotate around their z-axis with angular velocity of more than an average of 10rad/s . Finally, Fig. 4.9 shows the position of the soft microrobot on the XY-plane by tracking its motion for about 12s, while Fig. 4.10 (a) and (b) show its displacement on x and y axis with respect to time, respectively.

During experimental trials we tried to check the accuracy of the vibration sensors by testing their readings when a vibrating motor was standing on each of the sensors and when it was moving from one to the other. Vibration sensors' readings during 1D point-to-point

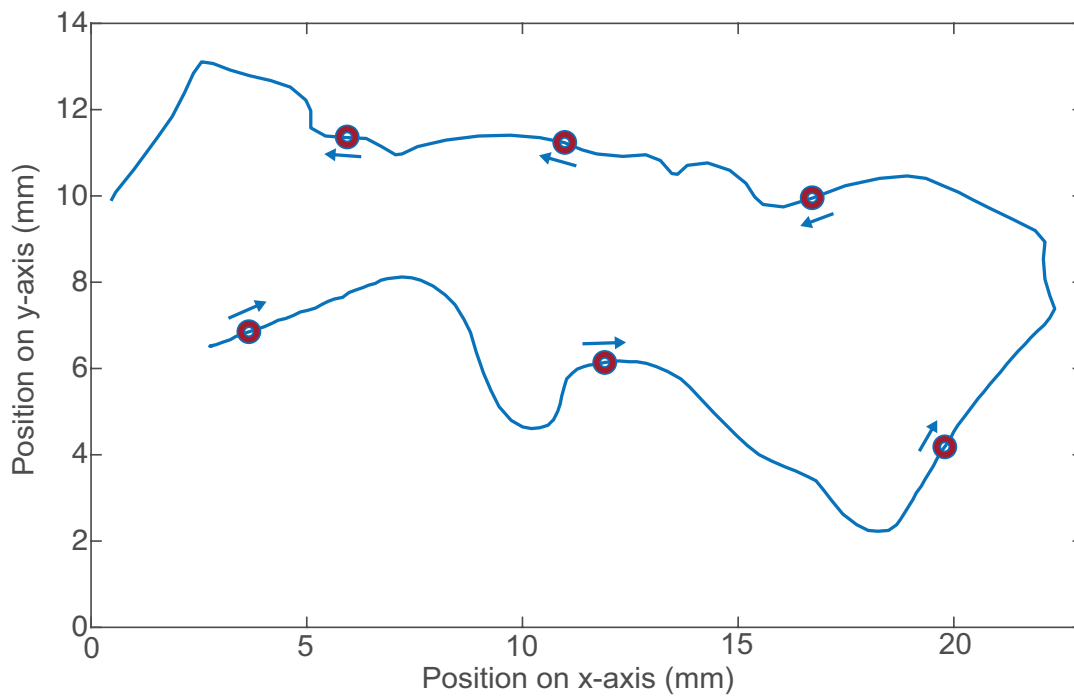


Figure 4.9: Position of microrobot on the XY-plane

localisation with two sensors can be seen on the right y-axis of Fig. 4.11, where a vibration motor was moving with varying speeds from the initial point A to destination point B in four different trials. The position of the motor during the trials can be also seen in Fig. 4.11 on its left y-axis. We marked with the respective colour the regions with the dominant average sensor readings. Note that there are regions that some sensor readings may be larger than the other sensor. However, we need to take into consideration a few more readings in their neighbourhood of samples to decide which region it belongs to.

Moreover, in order to increase the resolution of our sampling rate we used a data acquisition board (DAQ) with five channels, one for each sensor and we actuated the microrobot inside the plastic pipe. We used a Python-based software (PyDAQ) for interfacing with our hardware and for plotting the readings from the sensors with a sampling frequency of 66.7kHz .

Fig. 4.12 shows the channel outputs we obtained while testing the sensors by tapping a finger on each one of them with a pause of 1s between tapings. Fig. 4.13 shows the respective readings when a vibrating motor was operating and moving from one edge of the sensor array to the other, and Fig. 4.14 when the cylindrical magnet was rotating around its y axis inside the plastic pipe. Note that the output of the sensors is not expressed in voltage, but as digital output of an Analog-to-Digital converter (ADC). Then the relation to calculate

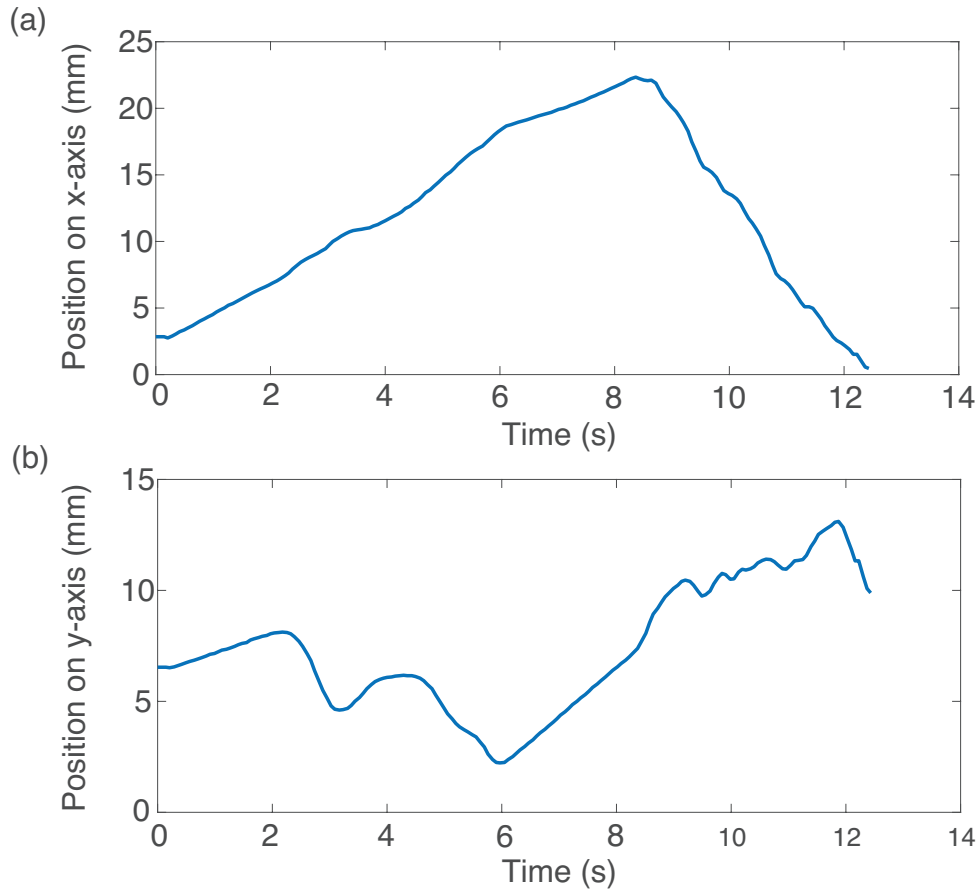


Figure 4.10: Displacement of microrobot on the (a) x-axis and (b) y-axis due time

the corresponding voltage is given by the following equation [78]:

$$\text{Voltage} = \frac{\text{Digital Output} \times \text{Reference Voltage}}{\text{Maximum Digital Value}}, \quad (4.1)$$

where our reference voltage was preset through the DAQ settings to $\pm 2.5V$.

Compared to the results obtained without a DAQ (Fig. 4.11), the sampling rate is greatly increased, capturing more readings from the sensors. However, this sampling includes also all the disturbances of neighbouring sensors and the vibration waves travelling through the material. This can be observed in Fig. 4.13 during the period of 5s – 25s while the motor was operating from Sensor 1 to Sensor 5, but Sensors 4 and 5 were already strongly affected by the vibrations. This phenomenon was not that obvious in the case of the cylindrical magnet moving (pitch motion) inside the plastic pipe (Fig. 4.14) from Sensor 1 to Sensor 5 (13s – 23s) and back (33s – 43s).

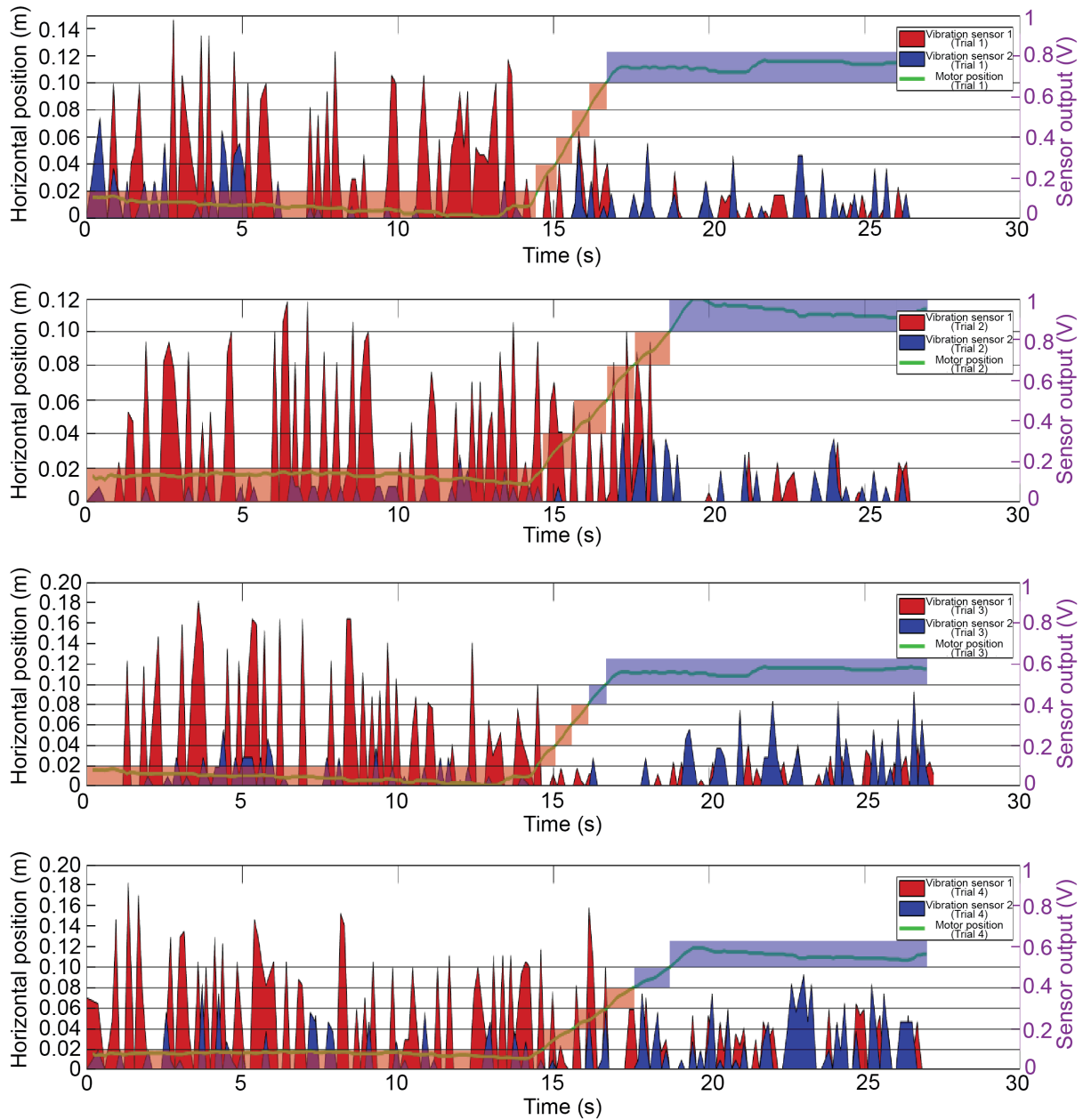


Figure 4.11: Vibration sensor output (right coordinate) and horizontal position (left coordinate) of vibrating motor with respect to time while moving from point A to point B at different speeds. Coloured areas indicate which sensor is having the highest output in the region

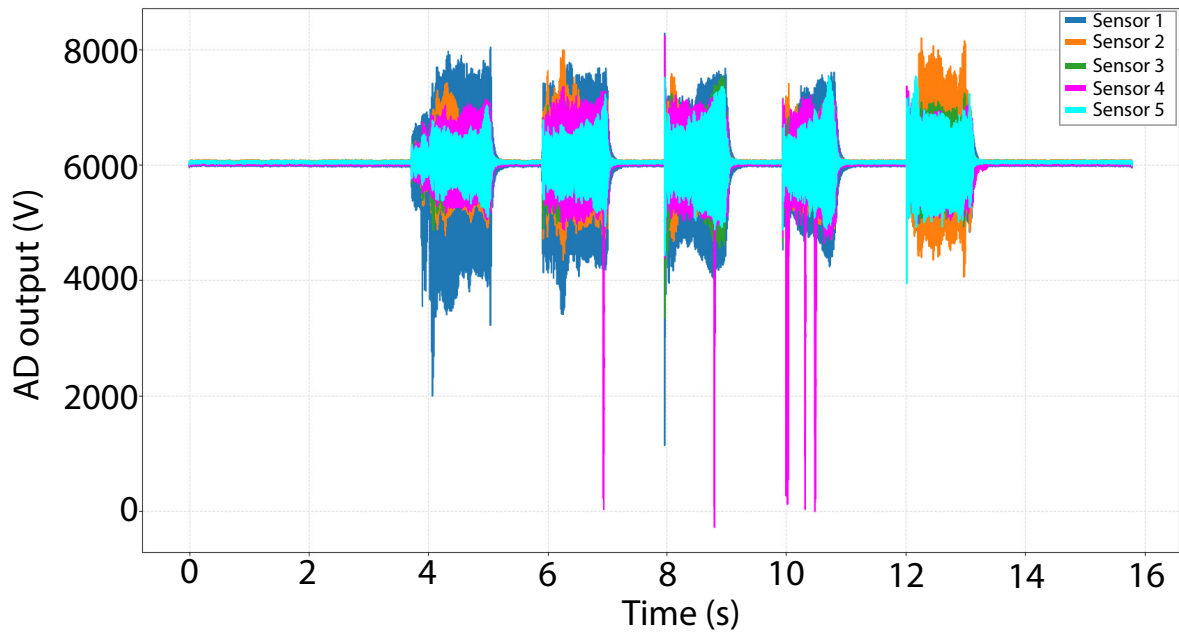


Figure 4.12: Sensing of vibrations through 5 channels using a DAQ board while tapping a plastic pipe with finger. The position of the finger tapping the plastic pipe is changing almost every second from Sensor 1 to Sensor 5 to test the respective sensor readings

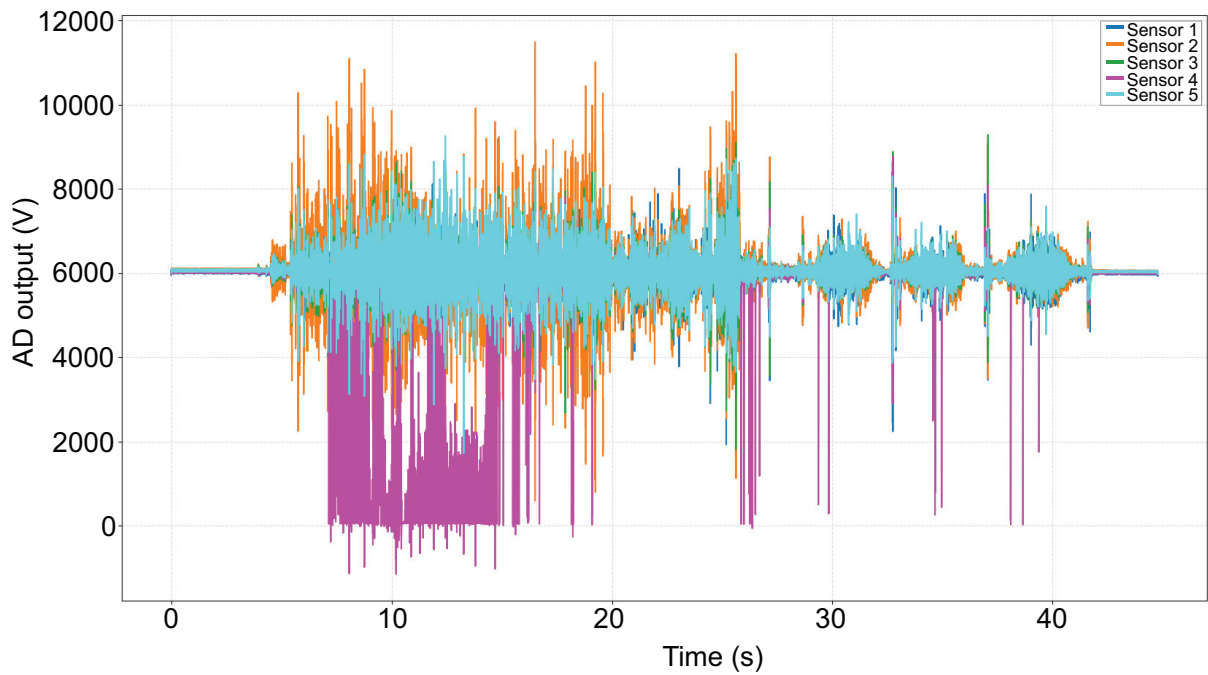


Figure 4.13: Sensing of vibrations while a motor was operating on the plastic pipe using a DAQ board

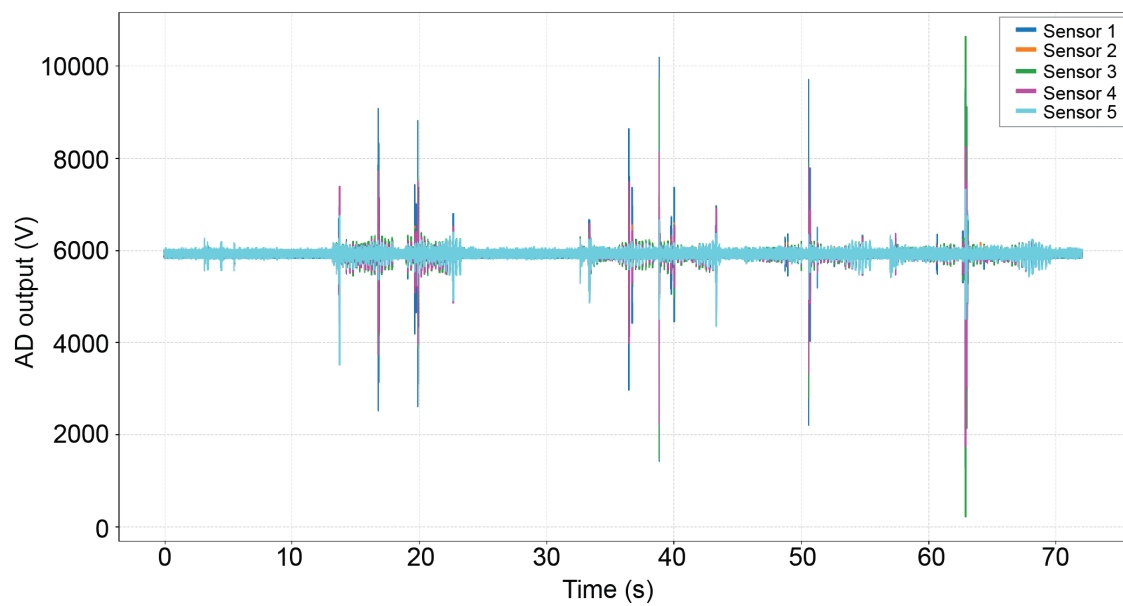


Figure 4.14: Vibration sensors' readings of magnet rotating around its y axis (pitch motion) inside a plastic pipe using a DAQ board

4.5 Discussion

In this chapter we presented our attempt to develop a novel fusion sensor localisation method using three different sensor arrays able to estimate the location of an operating microrobot inside the subject structure and correct the estimation based on additional readings from other sensors. At first we tried a Hall-effect sensor array working as the auxiliary array, having in mind the work by Son et al. [36]. The problem was that the sensors were far away from the microrobots and their magnetisation was weak to detect. Alternatively, we used omnidirectional microphones as sound sensors to locate and correct the estimations of microrobots' position, but not all of the sounds could be captured by the sensors. This led in many sound misses and inaccurate readings. Eventually, we used only vibration sensors, which they also had numerous limitations and problems.

Experimental trials shown that the vibration sensors were sensitive to vibrations near them when tested with thin plastic and paper layers. However, vibrations were not detectable with more solid and thicker objects. Due to manufacturing reasons, the ceramic plates were poorly wired to the sensors' terminals with thin copper wires, and any attempt to solder the broken ones, resulted in breaking pieces of the ceramic plate. This caused misbehaviour of the sensors during use and the need for another calibration since the sensitivity was changing. Handling five sensors altogether on the same array being close to each other was challenging, considering that any non-gentle move would cause a domino effect of the above problems.

Another limitation that we detected when we used the data acquisition board was the fact that vibration waves were travelling through the material causing unwanted readings. For instance we mention the large output of Sensor 2 on Fig. 4.12 when the magnet is located above Sensor 5, even though in previous locations (above Sensors 3 and 4) the readings appeared to be dropping. Finally, we occasionally noticed some disturbances in the readings that we assume they were from the electromagnetic field. These electrical noise to our readings were occurring in particular areas around the electromagnetic coil system we used for our experimental trials, or even when we were touching the microcontroller during actuation, which made us doubt the validity of them in general.

4.6 Conclusion

In this chapter we presented a novel localisation method that uses vibration sensors array to detect the presence of our fabricated microrobots inside a structure that we want to polish.

This research shown the problems that hold in this approach, but the results show also that it is possible to detect sufficiently heavy microrobots operating inside the subject structure. Our method managed to accurately locate a vibrating motor moving on an aluminium sheet from point A to point B being 10cm away. Also, a data acquisition board shown that if sensors are properly calibrated they have a potential to estimate the 1D position of a magnet pitching inside a plastic pipe, but additional sensing is required to correct wave pulse noises that lead to false readings. Moreover, using electromagnetic actuation with a coil system we managed to remotely actuate our microrobots presented in Chapter 3. The results shown that our microrobots with permanent magnets can yaw around their z axis with an average rotational speed of at least 14.2rad/s and pitch (rotate around their y axis) speed of up to 16.6mm/s , while our magnetised soft microrobots can rotate around their z axis with angular velocity of 10rad/s and pitch around their y axis to move with an average speed of 9mm/s .

Discussions and future work

” *The day science begins to study non-physical phenomena, it will make more progress in one decade than in all the previous centuries of its existence.*

– Nikola Tesla –

5.1	Discussions	70
5.1.1	Magnetically actuated lapper	70
5.1.2	Polishing microrobots	71
5.1.3	Localisation method.	74
5.2	Future work	76

5.1 Discussions

Regarding the work that we presented in the previous chapters, we mostly discussed the drawbacks of our methods, the problems we faced and the methods we developed and implemented to overcome them. We also presented alternatives to existing limitations in microfabrication technologies. In this section, we emphasise more on these limitations and challenges that our work addressed and we discuss the ones related to each approach of this project in a separate subsection here.

5.1.1 Magnetically actuated lapper

In this method we used a fixed case with a motor driver carrying a shaft on its tip rotating as the motor was powered. A disc with magnets that was screwed to the edge of the shaft and an identical disc with magnets and polishing features could be magnetically coupled, while having an acrylic plate between them. This method provided high speed polishing of the acrylic plate, removing the unwanted material from its surface, but also acrylic particles creating circular patterns on it (see Fig. 5.1).



Figure 5.1: Circular patterns of the polished acrylic surface by actuating the lapper on it for 1 min.

The limitations of this method were the following:

- (i) The coupling distance between the magnets (or the coupler-lapper distance) needed to be found and set after numerous experimental trials, so the decoupling effect occurring frequency can be reduced. What should be considered is that if distance was too small (magnets close to each other) the friction could not be overcome easily and the polishing was becoming aggressive and the polished area had more scratches and

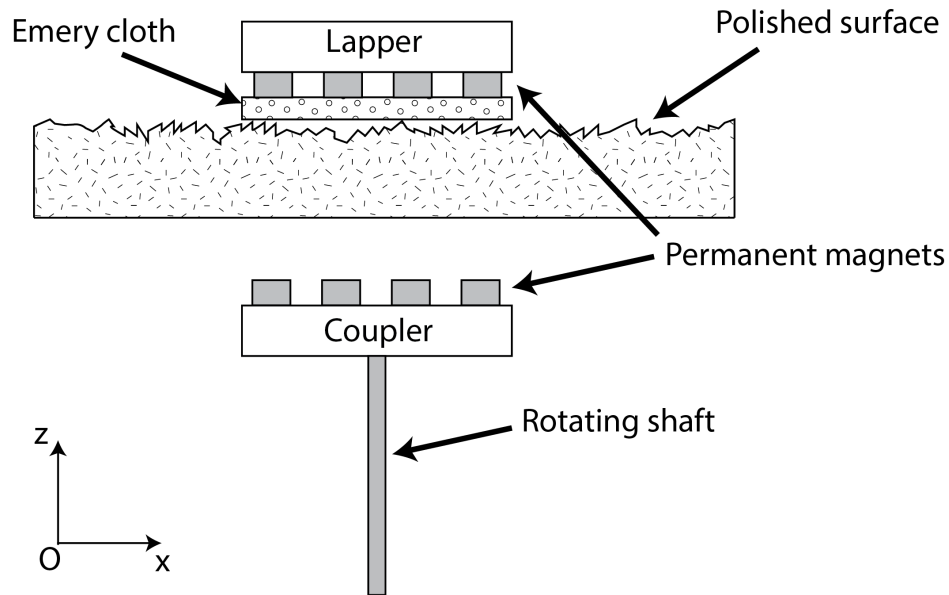


Figure 5.2: Schematic showing how the polishing process of the whole surface area is limited by the lapper's area of polishing.

visible patterns than a smooth surface result. Increasing the grit size of emery cloth could deal with the majority of the scratches and uneven areas, but still limited by the size of the polished area and the area of the emery cloth (see Fig. 5.2).

- (ii) The polishing area was fixed since the coupler was rotating under the acrylic surface on a fixed position. This means that the method required someone to adjust the location of the acrylic plate during the polishing process. To make it be an automated process and improve the results of surface condition (surface roughness) and material removal, we could create a frame of extruded aluminium v-rail profiles to build a moving bed for the polished surface or/and the DC motor (similar to a 3D printer operation).
- (iii) The dimensions of the polishing system and especially the size of the lapper that makes it unsuitable for the range of applications this project was targeting. In particular, the diameter of lapper is $30mm$, meaning that it cannot be guided through narrow passages (with diameter smaller than $10mm$) or complex geometries. Moreover, the surface area it covers is not applicable to curved surfaces like inner tubes or chambers.

5.1.2 Polishing microrobots

This project mostly focused on designing and fabricating millimetre scale magnetically-actuated microrobots able to pass through narrow spaces of diameter $4 - 10mm$ and access

unreachable areas. In Chapter 3 we presented our methods to design and fabricate microrobots suitable for this task. In this way, we addressed the latter limitation of the previous method that was discussed in Section 5.1.1.

In this method, we designed and fabricated microrobotic prototypes using different microfabrication technologies and methods. The problems mentioned in the literature appeared all during the steps of our microfabrication processes. Some of them were avoided with our alternative solutions when possible and high resolution quality was not absolutely necessary. Following, we summarise the most important of them in every method and the suggested ways to reduce their occurring frequency.

- (i) SU8 photolithography was used to fabricate and assemble layer-by-layer hard microrobots for remote magnetic actuation.
 - a) Dramatic waste of material during the spin-coating phase is known to be one of the main issues in this methodology. We managed to reduce the waste of material from more than 80%, mentioned in literature, to just 15 – 20%. However, it does not guarantee uniform distribution of SU8 on the substrate (glass slide or wafer).
 - b) Warping of SU8 layers during the hard-baking phase is an unwanted effect that may occur during photolithography. Soft-baked parts may not be hard-baked properly and not obtain the properties we want them to (hardness, durability, flatness). In our case, this was avoided from happening only during the first fabrication, while following ones always came with a warping effect and we had to reduce the hard-baking duration and temperature. Our assumption after all the fabrication attempts was that the reason it did not happen in the first time was that the glass slide we used was plasma treated prior to the fabrication process by another member of our lab sharing the facilities and equipment. If that was the case, this incident could actually benefit the whole fabrication process. However, there is no evidence of this hypothesis or any other findings from trials to support it. In general, it is recommended that the soft-baking step should be performed with extreme precision to prepare the material for the following steps.
 - c) Removing SU8 parts from the glass slide was a phase requiring delicate handling and precision with a high risk of breaking the fabricated parts. Our way to detach the parts from the glass slide without breaking them was to use a pair of tweezers to grab them and while aligning the tweezers with the glass slide, to pull straight upwards. Moving your tweezers sideways or even trying to scrape or poke it with a razorblade may break the parts. Fig. 5.3 shows the way that had our SU8 parts

broken, while Fig. 5.4 shows the way we managed to detach them in one-piece.

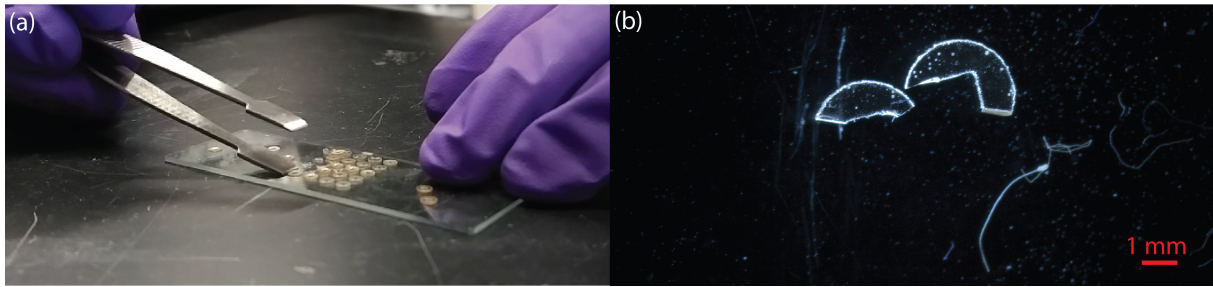


Figure 5.3: (a) Not recommended method to remove SU8 parts by poking them. (b) Microscope image showing broken SU8 part.

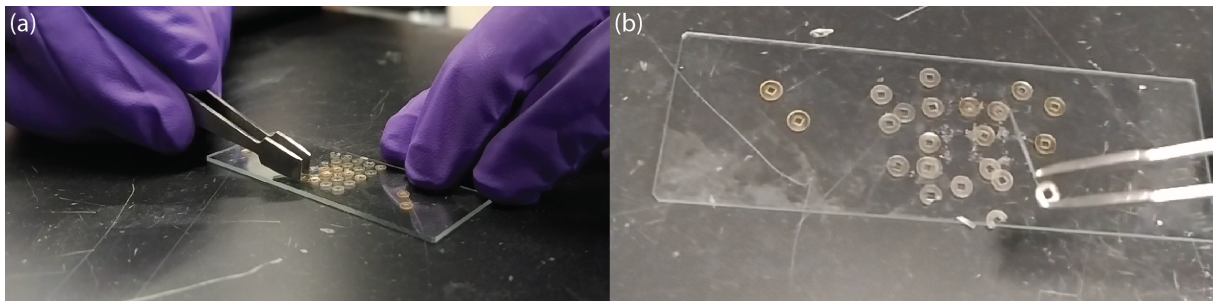


Figure 5.4: (a) Recommended method to remove SU8 parts. (b) Removed part held with the tweezers.

(ii) Soft-lithography was followed to fabricate soft repliche from the SU8 prototype in order to enhance it with the polishing property by adding abrasives, quicken the fabrication process and reduce the chance of failure.

a) The major issues occurred during our fabrication processes when desiccating the mixture of Smooth-Cast 327 and abrasives, because the air coming out of the mould's wells was carrying the abrasive powder with it in the form of foam (bubbles and particles). To prevent this from happening we stopped using the desiccator to remove the trapped air and let the abrasives sink in the wells. This solved the initial problem, but the encased bubbles were creating cavities in our final prototypes (see Fig. 5.5). Alternatively, we could let the powders be at the bottom of the wells and pour Smooth-Cast at the top or have the Smooth-Cast in the wells and sprinkle powders on top of it. Both cases were tried with the first ending having just powder on one side without letting any Smooth-Cast pass through to hold it, and the second having the powder sinking because Smooth-Cast density was not enough to hold it. More specifically, the fabricated prototype in the last case had a layer of Smooth-Cast keeping the abrasives inside it like

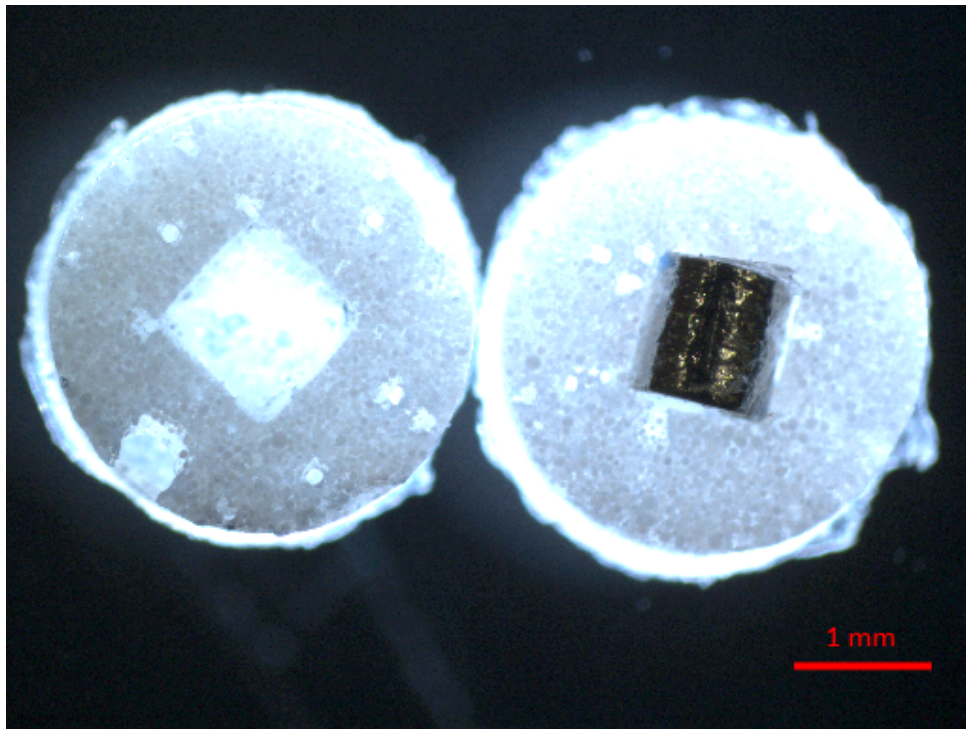


Figure 5.5: Microscope image showing the cavities in the soft repliche.

a protective shell. This led to prototypes without any polishing property on the outer surfaces of their shells.

- b) Fabricating abrasive-bonded magnetised soft repliche provided a customisable magnetisation profile using a permanent magnet to pass through our prototypes. However, both materials used (magnetite or Neodymium) did not provide our prototypes with as strong magnetisation as the permanent magnets offered in previous prototypes. In particular, our prototypes without permanent magnets had to be actuated in soaped water to overcome friction forces between them and the workspace substrate. The friction forces were because of tackiness of Smooth-Cast 327 on acrylic surface.

5.1.3 Localisation method

In Chapter 4 we presented our localisation method using vibration sensors to detect the position of a rolling magnet inside a plastic pipe and navigate it from point A to point B (1D localisation). Although our results shown an accurate response during 1D localisation, some drawbacks of the method still hold and there are aspects like delay and aliasing that have not been explored yet.

- (i) Material geometry and type of polished component: Thick and solid materials prevent vibrations to travel through them and be detected, while thin ones allow waves to travel and falsely trigger nearby sensors.
- (ii) Size of microrobot: Our fabricated microrobots were almost undetectable by the vibration sensors or some small vibrations could be detected from neighbouring sensors in rare cases. Magnets of larger size (3mm cubic and 4mm cylindrical) could be detected during their pitch motion on plastic and aluminium pipe tested in our experimental trials.
- (iii) 2D localisation requires large amount of sensors with high sensitivity, small area of detection to be effective in the fields of application we are interested in, and large data processing online.
- (iv) Delay: During real-time localisation and navigation of a microrobot operating inside a subject structure, there are specific steps that require computations and consequently they are causing delays in actuation. There is the sensing delay, due to the sensors' nature, the reading analysis delay to find the sensor with the highest readings, delay in calculating the actuation input to the microrobot. Each one of these parameters add up a delay component to the process and in a task like micropolishing that requires extreme precision, reaching the exact target area is challenging.
- (v) Temporal resolution: Using a data acquisition board surely improved the sampling rate, because by just using the Arduino serial ports there were missed readings. However, the sensors' readings we obtained might have been the result of aliasing, making them unreliable to use for localisation purposes.
- (vi) Spatial resolution: The resolution cell that each of the sensors covers is important to determine the distance between sensors. At the same time this may be different from sensor to sensor because of variations in vibration sensors due to manufacturing reasons. Using interpolation of sensors' readings was not explored as an option to deal with this limitation. However, we assume that the neighbouring sensors would be affected by the ceramic plates vibrations during operation. Additionally, the sensors are very fragile and to set a configuration for interpolation it is expected to be a challenging task.

5.2 Future work

As sciences evolve and progress through research, errors, challenges, and previously-unthinkable ideas, Microrobotics remains a scientific field that still has many limitations to overcome, but also numerous humanity's problems to solve. Trying to contribute to this effort of progress in the field, we addressed some of the challenges we found in the literature. However, since there is always space for improvement, some related future work could bring us even closer to our aims and to surprisingly beneficial results.

In terms of the lapper-bot polishing system, the hypothesis of remotely actuating coupled microrobots could actually be tested to explore if shear stress can be increased thanks to magnetic pull forces exerted between permanent magnets. The same principle could be used in complex geometries internally when the targeted area is farther away from the magnetic field to actuate a potential lapper microrobot, but a coupling component is still inside the field and can be used to actuate the microrobot indirectly.

Addressability of collective behaviour of micropolishers has not been explored, but it would be of great interest to investigate how shear stress would be increased when a swarm of microrobots was controlled remotely. For instance, the series of actions for microrobots to be navigated through narrow spaces, reach the desired location, be assembled to obtain the necessary shear stress, then be disassembled to navigate them back out, could be a futuristic sci-fi scenario.

To assist localisation with other sensor arrays, we could try an approach like the one by Yun et al in [79] implementing a stethoscope and microphone to detect the position of our microrobot since its size and mass make it almost undetectable.

Conclusion

” *I seem to have been only like a boy playing on the seashore, and diverting myself in now and then finding a smoother pebble or a prettier shell than ordinary, whilst the great ocean of truth lay all undiscovered before me.*

– Isaac Newton –

In this research project we attempted to deal with the challenging problem of internal surface finishing of complex structures produced with modern additive manufacturing technologies and have numerous applications in aerospace and automotive industry.

We have developed a lapping robot that uses magnetic coupling for remote actuation and can rotate about its z-axis an average angular velocity of 16.5 rad/s. Experimental trials shown that it can remove unwanted material from acrylic plates in high speeds although its size and the actuation constraints due to magnetic attraction limit the range of applications. Additionally, we have designed, fabricated and tested magnetically actuated microrobots using microfabrication technologies. In particular, we used SU8 photolithography to fabricate prototypes with a diameter of $\varnothing 3\text{mm}$ and thickness of 1mm , able to pass through narrow passages and be actuated inside structures with diameter smaller than 10mm. We also used soft lithography to fabricate replicas of the SU8 prototypes for quicker fabrication and to enhance them with polishing property. Finally, we developed a novel fabrication method to bond abrasives and magnetic particles in a soft replica microrobot that can be remotely actuated under a magnetic field. In this way we managed to obtain microrobots able to operate inside complicated structures and reach unreachable sites.

With respect to the localisation of our microrobots inside the polished structures, we proposed a novel method that could use vibration sensors to estimate the position of the microrobot inside the structure we want to polish. We presented the sensors' readings in specific scenarios that created vibrations on a plastic pipe (finger tapping, motor vibrating, magnet moving). However the small size of microrobots and the low sensitivity of sensors did not offer readings for our prototypes but only for $\varnothing 3-4\text{mm}$ permanent magnets (cubic, cylindrical) moving inside a plastic pipe. Finally, we used an electromagnetic coil system to actuate our microrobot prototypes inside the experimental workspace and managed to obtain an average rotational speed around their z axis of at least 10 rad/s and pitching speed of 9 mm/s.

References

- [1] D. Všíanský, J. Kolá and J. Petík. 'Continuity and changes of manufacturing traditions of Bell Beaker and Bronze Age encrusted pottery in the Morava river catchment (Czech Republic)'. In: *Journal of Archaeological Science* 49 (2014), pp. 414–422 (cit. on p. 2).
- [2] E. Guerra-Doce. 'Exploring the significance of Beaker pottery through residue analyses'. In: *Oxford Journal of Archaeology* 25.3 (2006), pp. 247–259 (cit. on p. 2).
- [3] H. Fokkens, Y. Achterkamp and M. Kuijpers. 'Bracers or Bracelets? About the Functionality and Meaning of Bell Beaker Wrist-guards'. In: *Proceedings of the Prehistoric Society* 74 (Jan. 2008), pp. 109–140 (cit. on p. 2).
- [4] R.J. Wenke. 'The Evolution of Early Egyptian Civilization: Issues and Evidence'. In: *Journal of World Prehistory* 5.3 (1991), pp. 279–329 (cit. on p. 2).
- [5] J. Siudmak. 'The sculpture of India 3000 B.C.—1300 A.D. By Pramod Chandra. pp. 224, illus. in colour and black and white, map. Washington, National Gallery of Art, Cambridge, Mass. and London, Harvard University Press. 1985. £50.95.' In: *Journal of the Royal Asiatic Society of Great Britain & Ireland* 118.2 (1986), pp. 292–293 (cit. on p. 2).
- [6] W. Miller. 'A History of the Akropolis of Athens'. In: *The American Journal of Archaeology and of the History of the Fine Arts* 8.4 (1893), pp. 473–556 (cit. on p. 2).
- [7] M. E. Moran. 'Evolution of robotic arms'. eng. In: *Journal of robotic surgery* 1.2 (2007). 2[PII], pp. 103–111 (cit. on p. 3).
- [8] K. Deshmukh, A. Muzaffar, T. Kováik et al. 'Chapter 17 - Fundamentals and applications of 3D and 4D printing of polymers: Challenges in polymer processing and prospects of future research'. In: *3D and 4D Printing of Polymer Nanocomposite Materials*. Ed.

by Kishor Kumar Sadasivuni, Kalim Deshmukh and Mariam Alali Almaadeed. Elsevier, 2020, pp. 527–560 (cit. on p. 3).

- [9] G. Strano, L. Hao, R. M. Everson and K. E. Evans. 'Surface roughness analysis, modelling and prediction in selective laser melting'. In: *Journal of Materials Processing Technology* 213.4 (2013), pp. 589–597 (cit. on p. 3).
- [10] B. Sun, G. Wood and S. Miyashita. 'Milestones for autonomous in-vivo microrobots in medical applications'. In: *Surgery* (2020) (cit. on p. 3).
- [11] M. Leary. '4 - Surface roughness optimisation for selective laser melting (SLM): Accommodating relevant and irrelevant surfaces'. In: *Laser Additive Manufacturing*. Ed. by Milan Brandt. Woodhead Publishing Series in Electronic and Optical Materials. Woodhead Publishing, 2017, pp. 99–118 (cit. on p. 3).
- [12] H.T. Kim and S.C. Kil. 'Research Trend of Dissimilar Metal Welding Technology'. In: *Computer Applications for Modeling, Simulation, and Automobile*. Berlin, Heidelberg: Springer Berlin Heidelberg, 2012, pp. 199–204 (cit. on p. 3).
- [13] ASTM Standard. *F2792-12a" Terminology for Additive Manufacturing Technologies"*. ASTM International. West Conshohocken, PA, DOI: 10.1520/F2792-12A. 2012 (cit. on p. 4).
- [14] J. Flynn, A. Shokrani, S. Newman and V. Dhokia. 'Hybrid Additive and Subtractive Machine Tools-Research and Industrial Developments'. In: *International Journal of Machine Tools and Manufacture* 101 (Nov. 2015) (cit. on p. 4).
- [15] W.S. Wan Harun, K. Kadirgama, M. Samykano et al. '5 - Mechanical behavior of selective laser melting-produced metallic biomaterials'. In: Woodhead Publishing Series in Biomaterials (2019). Ed. by J. Paulo Davim, pp. 101–116 (cit. on p. 4).
- [16] J. Guo, K.H. Au, C.N. Sun et al. 'Novel rotating-vibrating magnetic abrasive polishing method for double-layered internal surface finishing'. In: *Journal of Materials Processing Technology* 264 (2019), pp. 422–437 (cit. on pp. 4, 6, 10).
- [17] I.D. Marinescu, W.B. Rowe, B. Dimitrov and I. Inasaki. '5 - Forces, Friction, and Energy'. In: *Tribology of Abrasive Machining Processes*. Ed. by I.D. Marinescu, W.B. Rowe, B. Dimitrov and I. Inasaki. Norwich, NY: William Andrew Publishing, 2004, pp. 121–176 (cit. on pp. 4, 7).
- [18] W.B. Rowe. '17 - Mechanics of Abrasion and Wear'. In: *Principles of Modern Grinding Technology (Second Edition)*. Ed. by W.B. Rowe. Second Edition. Oxford: William Andrew Publishing, 2014, pp. 349–379 (cit. on pp. 4, 7).
- [19] M. Barletta. 'A new technology in surface finishing: fluidized bed machining (FBM) of aluminium alloys'. In: *Journal of materials processing technology* 173.2 (2006), pp. 157–165 (cit. on p. 4).

- [20] H. Lee, H. Kasuga, H. Ohmori, H. Lee and H. Jeong. 'Application of electrolytic in-process dressing (ELID) grinding and chemical mechanical polishing (CMP) process for emerging hard-brittle materials used in light-emitting diodes'. In: *Journal of Crystal Growth* 326.1 (2011). Symposium on Wide Bandgap Semiconductors (III-Nitrides, SiC, and Diamond), pp. 140–146 (cit. on p. 4).
- [21] K.L. Tan, S.H. Yeo and C.H. Ong. 'Nontraditional finishing processes for internal surfaces and passages: A review'. In: *Proceedings of the Institution of Mechanical Engineers, Part B: Journal of Engineering Manufacture* 231.13 (2017), pp. 2302–2316. eprint: [10.1177/0954405415626087](https://doi.org/10.1177/0954405415626087) (cit. on pp. 4, 9, 10).
- [22] D.A. Axinte, B. Karpuschewski, M.C. Kong et al. 'High Energy Fluid Jet Machining (HEFJet-Mach): From scientific and technological advances to niche industrial applications'. In: *CIRP Annals* 63.2 (2014), pp. 751–771 (cit. on p. 5).
- [23] R. Seemann, M. Brinkmann, E.J. Kramer, F.F. Lange and R. Lipowsky. 'Wetting morphologies at microstructured surfaces'. In: *Proceedings of the National Academy of Sciences* 102.6 (2005), pp. 1848–1852. eprint: <https://www.pnas.org/content/102/6/1848.full.pdf> (cit. on p. 5).
- [24] B. Gleeson. 'High-Temperature Corrosion of Metallic Alloys and Coatings'. In: Apr. 2008, pp. 173–228 (cit. on p. 5).
- [25] J.W. Brooks and P.J. Bridges. 'Metallurgical Stability of Inconel Alloy 718'. In: Jan. 1988, pp. 33–42 (cit. on p. 5).
- [26] W. Kaplonek, K. Nadolny, K. Rokosz et al. 'Internal Cylindrical Grinding Process of INCONEL® Alloy 600 Using Grinding Wheels with Sol-Gel Alumina and a Synthetic Organosilicon Polymer-Based Impregnate'. eng. In: *Micromachines* 11.2 (Jan. 2020). mi11020115[PII], p. 115 (cit. on p. 5).
- [27] K. Nadolny and D. Herman. 'Effect of vitrified bond microstructure and volume fraction in the grinding wheel on traverse internal cylindrical grinding of Inconel® alloy 600'. In: *The International Journal of Advanced Manufacturing Technology* 81.5 (Nov. 2015), pp. 905–915 (cit. on p. 5).
- [28] W. Song, Z. Peng, P. Li, P. Shi and S. Choi. 'Annular Surface Micromachining of Titanium Tubes Using a Magnetorheological Polishing Technique'. In: *Micromachines* 11 (2020) (cit. on p. 5).
- [29] J. Guo, C.W. Kum, K.H. Au et al. 'New vibration-assisted magnetic abrasive polishing (VAMAP) method for microstructured surface finishing'. In: *Opt. Express* 24.12 (June 2016), pp. 13542–13554 (cit. on pp. 5, 10).

- [30] J. Zhang, J. Hu, H. Wang, A. Kumar and A. Chaudhari. 'A novel magnetically driven polishing technique for internal surface finishing'. In: *Precision Engineering-journal of The International Societies for Precision Engineering and Nanotechnology* 54 (2018), pp. 222–232 (cit. on pp. 6, 9).
- [31] V.K. Jain. 'Magnetic field assisted abrasive based micro-/nano-finishing'. In: *Journal of Materials Processing Technology* 209.20 (2009), pp. 6022–6038 (cit. on p. 6).
- [32] D.K. Singh, V.K. Jain, V. Raghuram and R. Komanduri. 'Analysis of surface texture generated by a flexible magnetic abrasive brush'. In: *Wear* 259.7-12 (2005), pp. 1254–1261 (cit. on p. 6).
- [33] J. Zhang, H. Wang, A. Kumar and M. Jin. 'Experimental and theoretical study of internal finishing by a novel magnetically driven polishing tool'. In: *International Journal of Machine Tools and Manufacture* 153 (2020), p. 103552 (cit. on p. 6).
- [34] J. Kang, A. George and H. Yamaguchi. 'High-speed Internal Finishing of Capillary Tubes by Magnetic Abrasive Finishing'. In: *Procedia CIRP* 1 (2012). Fifth CIRP Conference on High Performance Cutting 2012, pp. 414–418 (cit. on pp. 6, 10).
- [35] N. Ramachandran, S.S. Pande and N. Ramakrishnan. 'The role of deburring in manufacturing: A state-of-the-art survey'. In: *Journal of Materials Processing Technology* 44.1 (1994), pp. 1–13 (cit. on pp. 6, 7).
- [36] D. Son, S. Yim and M. Sitti. 'A 5-D Localization Method for a Magnetically Manipulated Untethered Robot using a 2-D Array of Hall-effect Sensors'. In: *IEEE ASME Trans Mechatron* 21.2 (2016), pp. 708–716 (cit. on pp. 7, 66).
- [37] M. Jackson and J. Morrell. '5 - Tribology in manufacturing'. In: *Tribology for Engineers*. Ed. by J. Paulo Davim. Woodhead Publishing, 2011, pp. 161–241 (cit. on p. 7).
- [38] A.W. Mahoney and J.J. Abbott. 'Managing magnetic force applied to a magnetic device by a rotating dipole field'. In: *Applied Physics Letters* 99.13 (2011), p. 134103 (cit. on p. 7).
- [39] J.J. Abbott, O. Ergeneman, M.P. Kummer, A.M. Hirt and B. J. Nelson. 'Modeling Magnetic Torque and Force for Controlled Manipulation of Soft-Magnetic Bodies'. In: *Trans. Rob.* 23.6 (Dec. 2007), pp. 1247–1252 (cit. on p. 7).
- [40] J. Li, Z. Ma, M. Jiang, Y. Zhang and L. Wan. 'Optimized design of the flow network in the lubrication system for the heavy vehicle transmission'. In: *Advances in Mechanical Engineering* 9.4 (2017), p. 1687814017696414. eprint: <https://doi.org/10.1177/1687814017696414> (cit. on pp. 7, 8).
- [41] G.R. Wlodyga and S.A. Weiner. 'An Overview of Two-Piece Die Cast Aluminum Intake Manifold Joining'. In: *SAE Transactions* 91 (1982), pp. 1515–1524 (cit. on p. 7).

- [42] C. Pawashe, S. Floyd and M. Sitti. 'Magnetic mobile micro-robots'. In: *7eme Journees Nationales de la Recherche en Robotique* (2009) (cit. on p. 8).
- [43] A. Becker, C. Onyuksel, T. Bretl and J. McLurkin. 'Controlling many differential-drive robots with uniform control inputs'. In: *The International Journal of Robotics Research* 33.13 (2014), pp. 1626–1644 (cit. on p. 8).
- [44] H. Xie, M. Sun, X. Fan et al. 'Reconfigurable magnetic microrobot swarm: Multimode transformation, locomotion, and manipulation'. In: *Science Robotics* 4.28 (2019) (cit. on p. 8).
- [45] M. Driscoll, B. Delmotte, M. Youssef et al. 'Unstable fronts and motile structures formed by microrollers'. English (US). In: *Nature Physics* 13.4 (Apr. 2017), pp. 375–379 (cit. on p. 8).
- [46] P. Corradi, O. Scholz, T. Knoll, A. Menciassi and P. Dario. 'An optical system for communication and sensing in millimetre-sized swarming microrobots'. In: *Journal of Micromechanics and Microengineering* 19.1 (Dec. 2008), p. 015022 (cit. on p. 9).
- [47] G.Z. Lum, Zhou Ye, Xiaoguang Dong et al. 'Shape-programmable magnetic soft matter'. In: *Proceedings of the National Academy of Sciences* 113.41 (May 2016), E6007–E6015 (cit. on p. 9).
- [48] E. Diller, J. Giltinan, G.Z. Lum, Z. Ye and M. Sitti. 'Six-degree-of-freedom magnetic actuation for wireless microrobotics'. In: *The International Journal of Robotics Research* 35.1-3 (2016), pp. 114–128. eprint: <https://doi.org/10.1177/0278364915583539> (cit. on p. 9).
- [49] C. Xu, Z. Yang and G. Z. Lum. 'Small-Scale Magnetic Actuators with Optimal Six Degrees-of-Freedom'. In: *Advanced Materials* 33.23 (2021), p. 2100170. eprint: <https://onlinelibrary.wiley.com/doi/pdf/10.1002/adma.202100170> (cit. on p. 9).
- [50] C. Chung and C.H. Yang. 'A 1.5-J/Task Path-Planning Processor for 2-D/3-D Autonomous Navigation of Microrobots'. In: *IEEE Journal of Solid-State Circuits* 56.1 (2021), pp. 112–122 (cit. on p. 9).
- [51] D. Folio and A. Ferreira. 'Two-Dimensional Robust Magnetic Resonance Navigation of a Ferromagnetic Microrobot Using Pareto Optimality'. In: *IEEE Transactions on Robotics* 33.3 (2017), pp. 583–593 (cit. on p. 9).
- [52] M. Abbes, K. Belharet, H. Mekki and G. Poisson. 'Permanent Magnets based Actuator for Microrobots Navigation'. In: *2019 IEEE/RSJ International Conference on Intelligent Robots and Systems (IROS)*. 2019, pp. 7062–7067 (cit. on p. 9).

- [53] L. Yang and L. Zhang. 'Large-Workspace and High-Resolution Magnetic Microrobot Navigation Using Global-Local Path Planning and Eye-in-Hand Visual Servoing'. In: *2020 IEEE 16th International Conference on Automation Science and Engineering (CASE)*. 2020, pp. 876–881 (cit. on p. 9).
- [54] J. Nam, S. Jeon, S. Kim and G. Jang. 'Crawling microrobot actuated by a magnetic navigation system in tubular environments'. In: *Sensors and Actuators A: Physical* 209 (2014), pp. 100–106 (cit. on p. 9).
- [55] D. Li, D. Dong, W. Lam et al. 'Automated In Vivo Navigation of Magnetic-Driven Microrobots Using OCT Imaging Feedback'. In: *IEEE Transactions on Biomedical Engineering* 67.8 (2020), pp. 2349–2358 (cit. on p. 9).
- [56] G. Go, H. Choi, S. Jeong et al. 'Electromagnetic Navigation System Using Simple Coil Structure (4 Coils) for 3-D Locomotive Microrobot'. In: *IEEE Transactions on Magnetics* 51.4 (2015), pp. 1–7 (cit. on p. 9).
- [57] C.H. Wu, C.W. Kum, Y.M. Wan Stephen and A.M. Abu Bakar. 'Numerical and experimental investigation of abrasive flow machining of branching channels'. In: *The International Journal of Advanced Manufacturing Technology* 108.9-10 (June 2020), pp. 2945–2966 (cit. on p. 9).
- [58] F. Taher, J. Vidler and J. Alexander. 'A Characterization of Actuation Techniques for Generating Movement in Shape-Changing Interfaces'. In: *International Journal of Human-Computer Interaction* 33.5 (2017), pp. 385–398. eprint: <https://doi.org/10.1080/10447318.2016.1250372> (cit. on p. 9).
- [59] J. Guo, H.J. Hua Jong, R. Kang and D. Guo. 'Novel localized vibration-assisted magnetic abrasive polishing method using loose abrasives for V-groove and Fresnel optics finishing'. In: *Opt. Express* 26.9 (Apr. 2018), pp. 11608–11619 (cit. on p. 10).
- [60] J. Guo, C. Song, Y. Fu et al. 'Internal Surface Quality Enhancement of Selective Laser Melted Inconel 718 by Abrasive Flow Machining'. In: *Journal of Manufacturing Science and Engineering* 142.10 (June 2020). 101003 (cit. on p. 10).
- [61] S. Han, F. Salvatore, J. Rech and J. Bajolet. 'Abrasive flow machining (AFM) finishing of conformal cooling channels created by selective laser melting (SLM)'. In: *Precision Engineering-journal of The International Societies for Precision Engineering and Nanotechnology* 64 (2020), pp. 20–33 (cit. on p. 10).
- [62] 'Rotating Bodies - Stress'. In: *The Engineering ToolBox (2011)* ([Accessed November 2020]). eprint: https://www.engineeringtoolbox.com/stress-rotation-disc-ring-body-d_1752.html (cit. on p. 23).

- [63] J.J. Abbott, E. Diller and A.J. Petruska. 'Magnetic Methods in Robotics'. In: *Annual Review of Control, Robotics, and Autonomous Systems* 3.1 (2020), pp. 57–90. eprint: <https://doi.org/10.1146/annurev-control-081219-082713> (cit. on p. 23).
- [64] S. Miyashita and R. Pfeifer. 'Attributes of two-dimensional magnetic self-assembly'. In: *Adaptive Behavior* 20.2 (2012), pp. 117–130. eprint: <https://doi.org/10.1177/1059712311423983> (cit. on p. 25).
- [65] G. Kibria and B. Bhattacharyya. '4 - Microelectrical discharge machining of Ti-6Al-4V: Implementation of innovative machining strategies'. In: *Microfabrication and Precision Engineering*. Ed. by J. Paulo Davim. Woodhead Publishing Reviews: Mechanical Engineering Series. Woodhead Publishing, 2017, pp. 99–142 (cit. on p. 26).
- [66] 'HSV Color Range Thresholding'. In: *Learn Code By Gaming* (July 2020). eprint: <https://learncodebygaming.com/blog/hsv-color-range-thresholding> (cit. on p. 27).
- [67] S. Chakraborty and S.K. Mitra. 'Microfluidics and Nanofluidics Handbook: Fabrication, Implementation and Applications'. In: 2012, pp. 231–268 (cit. on p. 36).
- [68] S. Han, J. Derksen and J.H. Chun. 'Extrusion Spin Coating: An Efficient and Deterministic Photoresist Coating Method in Microlithography'. In: *Semiconductor Manufacturing, IEEE Transactions on* 17 (Mar. 2004), pp. 12–21 (cit. on p. 39).
- [69] Marc A. Nabhan, Carlos A. Silvera Batista, David E. Cliffler and G. Kane Jennings. 'Spin Coating Photoactive Photosystem I–PEDOT:PSS Composite Films'. In: *ACS Applied Polymer Materials* 5.5 (2023), pp. 3278–3288. eprint: <https://doi.org/10.1021/acsapm.2c02126> (cit. on p. 39).
- [70] F. Mandoj, S. Nardis, C. Di Natale and R. Paolesse. 'Porphyrinoid Thin Films for Chemical Sensing'. In: *Encyclopedia of Interfacial Chemistry*. Ed. by Klaus Wandelt. Oxford: Elsevier, 2018, pp. 422–443 (cit. on p. 39).
- [71] Y. Xia and G. M. Whitesides. 'Soft Lithography'. In: *Annual Review of Materials Science* 28 (1998). 604, pp. 153–184 (cit. on p. 42).
- [72] N. Safavian, S. K. C. Toh, M. Pani and R. Lee. 'Endoscopic measurement of the size of gastrointestinal polyps using an electromagnetic tracking system and computer vision-based algorithm'. In: *International Journal of Computer Assisted Radiology and Surgery* 19.2 (Feb. 2024), pp. 321–329 (cit. on p. 52).
- [73] I. Umay, B. Fidan and B. Barshan. 'Localization and Tracking of Implantable Biomedical Sensors'. In: *Sensors* 17.3 (Mar. 2017), p. 583 (cit. on p. 52).

- [74] D. Kim, K. Hwang, J. Park, H. Park and S. Ahn. 'Miniaturization of Implantable Micro-Robot Propulsion Using a Wireless Power Transfer System'. In: *Micromachines* 8.9 (Sept. 2017), p. 269 (cit. on pp. 52, 53).
- [75] S. Yim and M. Sitti. '3-D Localization Method for a Magnetically Actuated Soft Capsule Endoscope and Its Applications'. In: *IEEE Transactions on Robotics* 29.5 (Oct. 2013), pp. 1139–1151 (cit. on p. 53).
- [76] L. Mao, J. Chen, Z. Li and D. Zhang. 'Relative Localization Method of Multiple Micro Robots Based on Simple Sensors'. In: *International Journal of Advanced Robotic Systems* 10.2 (Feb. 2013), p. 128 (cit. on p. 53).
- [77] S. Miyashita, S. Guitron, S. Li and D. Rus. 'Robotic metamorphosis by origami exoskeletons'. In: *Science Robotics* 2.10 (2017). eprint: <https://robotics.sciencemag.org/content/2/10/eaao4369.full.pdf> (cit. on p. 54).
- [78] M. J.M. Pelgrom. *Analog-to-Digital Conversion*. 2nd edition. Springer New York, 2013 (cit. on p. 62).
- [79] H. Yun, H. Kim, E. Kim and M. B.G. Jun. 'Development of internal sound sensor using stethoscope and its applications for machine monitoring'. In: *Procedia Manufacturing* 48 (2020), pp. 1072–1078 (cit. on p. 76).

List of Figures

1.1	Split view of Parthenon showing its present and ancient structure. Snapshot was taken from an interactive photo at https://www.visionpubl.com/en/cities/athens/parthenon-facts-history/	2
1.2	Lubrication circuit passage diameter variation where orifices diameters are $D_A = 3.5mm$, $D_B = 2.5mm$, $D_C = 3mm$, $D_D = 1.5mm$, $D_{Main\ front} = 5mm$, $D_{Auxi\ rear} = 2mm$, respectively [40].	8
2.1	(a) Side, and (b) top view of the system setup we used during trials. The appearing arrows are pointing in the direction of rotation during operation.	16
2.2	(a), (b), and (c) Configurations of $\varnothing 2mm \times 1mm$ cylindrical magnets attached to a discoid piece of emery cloth with opposing polarity, (d) side of emery cloth with abrasives for polishing	17
2.3	The assembled components and circuit that we used during the experimental phase	18
2.4	A plastic surface with correction fluid before (left) and after (right) polishing with a discoid emery cloth with hands-applied forces	19
2.5	(a) Physical view of the system configuration used in case (i). (b) A close-up physical view of the system configuration used in case (ii).	20
2.6	Physical designs of (a) the lapper, and (b) the coupler. (c) Transparent model design of the remotely actuated coupler in the case of using bar magnets for torque transmission, and (d) physical design of the bar magnets PLA case.	21
2.7	The shear stress produced at the circumference of rotating disc without friction with respect to the lapper's angular velocity based on Eq. (2.1)	24
2.8	Model of the magnetic pull force between the cylindrical magnets with respect to the distance between them based on Eq. (2.3).	25

2.9	Snapshots from the camera input using the OpenCV algorithm before (left) and during (right) the polishing process.	27
2.10	(a) Angular distance and (b) angular velocity of the rotating disc with respect to time	29
2.11	Polymer plates after polishing with emery cloth of the respective grit size	29
2.12	Percentage of black pixels with respect to the time passed	31
3.1	Illustration of the assembly process of the microrobot SU8 parts and 1mm cylindrical magnet at its centre	37
3.2	Illustration of the process followed for adjusting SU-8 thickness on glass slide	38
3.3	(a) The designed mask pattern for trial UV exposure. The outer diameter of discoids and squares'/triangles' edges have a length of 3mm, while the diameter of the inner circular slot is 1mm. (b) The final mask design taped down onto the glass plate	38
3.4	SU-8 parts (a) before (on glass slide), and (b) after (in Petri dish) removing phase.	39
3.5	(a) Top and (b) side view of the microrobot made of SU-8 parts under the microscope with annotated dimensions.	40
3.6	SU-8 fabricated parts under the microscope (with annotated dimensions), before being removed from the glass slide.	40
3.7	Angled view of the warped SU-8 parts before being removed from the glass slide.	41
3.8	(a) Angled view of the microrobot with assembled SU-8 parts and cylindrical magnet $\varnothing 1mm \times 1mm$ placed in their centre attached to a rod of magnets for presentation purposes. (b) Final prototype microrobot sitting on a human finger.	41
3.9	Schematic view of the assembly process and physical view of the final microrobot under the microscope. Discoid emery cloth parts are shown as they were glued at the top and the bottom of it.	42
3.10	(a) 3D printed mould used for mould-making using soft-lithography.(b) Mold Star Parts A & B prepared to pour into mixing dish placed onto a precision scale	44
3.11	(a) Fabrication process that demonstrates how Mold Star mixture was poured into a 3D printed resin sample mould. (b) Mold Star moulds let to cure, and (c) soft moulds after removed from 3D printed resin moulds.	45

3.12	(a) Soft microrobots' chassis repliche carrying abrasives bonded with Smooth-Cast 327. Parts in the left mould have Silicon Carbide (dark grey abrasive particles), while parts in the right mould have Aluminium Oxide (white abrasive powder). (b) Removed part sitting on a human finger	47
3.13	Replica microrobot made of Smooth-Cast 327 sitting (a) on the right to and (b) below the one made of SU-8 for comparison.	47
4.1	Physical view of the experimental setup used during trials on metal parts . . .	54
4.2	Microscope snapshots of different microrobot variants during operation on metal parts	55
4.3	(a) Top and (b) side view of the setup we used to calibrate the two vibration sensors attached on an aluminium sheet.	56
4.4	Experimental setup with vibration sensors attached to the plastic pipe where a permanent magnet was rolling in	57
4.5	Vibrations sensors placed on a Dura-Lar sheet cut with a pattern to hold the sensors in position	57
4.6	Snapshots of a 4mm cylindrical magnet rolling inside the plastic pipe to calibrate the vibration sensors	58
4.7	(a) Angle and (b) rotational speed of the SU8 triangular microrobot with respect to time	59
4.8	(a) Angle and (b) rotational speed of the abrasive-bonded microrobot around its z axis with respect to time	60
4.9	Position of microrobot on the XY-plane	61
4.10	Displacement of microrobot on the (a) x-axis and (b) y-axis due time	62
4.11	Vibration sensor output (right coordinate) and horizontal position (left coordinate) of vibrating motor with respect to time while moving from point A to point B at different speeds. Coloured areas indicate which sensor is having the highest output in the region	63
4.12	Sensing of vibrations through 5 channels using a DAQ board while tapping a plastic pipe with finger. The position of the finger tapping the plastic pipe is changing almost every second from Sensor 1 to Sensor 5 to test the respective sensor readings	64
4.13	Sensing of vibrations while a motor was operating on the plastic pipe using a DAQ board	64
4.14	Vibration sensors' readings of magnet rotating around its y axis (pitch motion) inside a plastic pipe using a DAQ board	65

5.1	Circular patterns of the polished acrylic surface by actuating the lapper on it for 1 min.	70
5.2	Schematic showing how the polishing process of the whole surface area is limited by the lapper's area of polishing.	71
5.3	(a) Not recommended method to remove SU8 parts by poking them. (b) Microscope image showing broken SU8 part.	73
5.4	(a) Recommended method to remove SU8 parts. (b) Removed part held with the tweezers.	73
5.5	Microscope image showing the cavities in the soft repliche.	74

List of Tables

1.1	Advantages and disadvantages of finishing categories	5
2.1	Parameters and properties of components	23
2.2	Polymer plate weights	29
4.1	Angular velocity and rolling speed of microrobots	59

Appendix


```

22 force2 = zeros(30,3); % Magnetic force vector
23 Nstress = zeros(30,3); % Normal stress
24 A = pi*(30*10^(-3))^2; % Surface area of stress (module area)
25 Ncyl = 10; % Number of cylindrical magnets
26 h = 4*10^(-3); %Thickness in meters
27 R = 2.5*10^(-3); % Cylinder's radius in meters
28 Vcyl = h*pi*R^2; % Cylinder's volume in cubic meters
29 Msat = 1.32; % Magnetic saturation in Teslas
30 mu0 = 4*pi*10^(-7); % Permeability of the free space in Henry
    per meter
31
32 rst = zeros(30,3);
33 mcyl = [0,0,Vcyl*Msat/mu0]; % Magnetic dipole moment of
34 % cylindrical magnet 2mmx1mm in Am^2
35
36 mcylN = Ncyl*mcyl; % Magnetic dipole moment of
37 % cylindrical magnets 2mmx1mm in a row in
    Am^2
38
39
40 %% Vector iterative calculation:
41 for i=1:length(t)
42     r(3)=r(3)+step;
43     factor = 2*dot(r,mcylN)*mcylN+dot(mcylN,mcylN)*r-5*dot(r,
        mcylN)*dot(r,mcylN)*r/norm(r)^2;
44     force(i,:) = 3*mu0*factor/(4*pi*norm(r)^5);
45     force2(i,:) = 3*mu0*dot(mcylN,mcylN)/(2*pi*norm(r)^4);
46     Nstress(i,:) = force2(i,+)/A;
47     rst(i,:)=r;
48 end
49
50 %% Figure printing:
51 figure
52 plot(rst(:,3),force2(:,3),'b','MarkerSize',12)
53 set(gca,'FontSize',11,'fontname','arial')
54 xlabel('Distance (m)')
55 ylabel('Force (N)')

```

```
56 grid on
57 % title('Plot of Magnetic Force related to distance')
58
59 figure
60 plot(rst(:,3),Nstress(:,3),'b','MarkerSize',12)
61 set(gca,'FontSize',11,'fontname','arial')
62 xlabel('Distance (m)')
63 ylabel('Stress (N/m^2)')
64 grid on
65 % title('Plot of normal stress related to distance')
```

```

1 %% Calculation of the torque produced by permanent bar NdFeB
  magnets applied on permanent cylindrical NdFeB magnets:
2
3 %% Parameter initialisation:
4 r = [0,1*10^(-3),0.001]; % Position vector of B-field (
  distance vector from dipole) in meters
5 rhat = r/norm(r); % Unit vector of r (r hat)
6 step = 0.001; % Increasing step for distance
7 D = 3*10^(-2); % Distance of workspace from bar magnets in
  meters
8 t=0.001:step:D; % The matrix of varying distance
9 torque = zeros(30,3); % Magnetic torque vector
10 force = zeros(30,3); % Magnetic force vector
11 force2 = zeros(30,3); % Magnetic force vector
12 Ncyl = 4; % Number of cylindrical magnets
13 Nbar = 6; % Number of bar magnets
14 h = 4*10^(-3); %Thickness in meters
15 R = 2.5*10^(-3); % Cylinder's radius in meters
16 Vcyl = h*pi*R^2; % Cylinder's volume in cubic meters
17 Vbar = 60*10*3*10^(-9); % Bar's volume in cubic meters
18 Msat = 1.32; % Magnetic saturation in Teslas
19 mu0 = 4*pi*10^(-7); % Permeability of the free space in Henry
  per meter
20
21 rst = zeros(30,3);
22 mcyl = [Vcyl*Msat/mu0,Vcyl*Msat/mu0,Vcyl*Msat/mu0]; %
  Magnetic dipole moment of
23 % cylindrical magnet 2mmx1mm in Am^2
24 mbar = [Vbar*Msat/mu0,Vbar*Msat/mu0,Vbar*Msat/mu0]; %
  Magnetic dipole moment of
25 % bar magnet 60mmx10mmx3mm in Am^2
26
27 mcylN = Ncyl*mcyl; % Magnetic dipole moment of
28 % cylindrical magnets 2mmx1mm in a row in
  Am^2
29 mbarN = Nbar*mbar; % Magnetic dipole moment of
30 % bar magnets 60mmx10mmx3mm in a row in Am

```

^2

```
31
32 HbarN = (3*dot(rhat ,mbarN)*rhat -mbarN)/(4*pi*norm(r)^3);
33 BbarN = mu0*HbarN;
34
35 %% Vector iterative calculation:
36 for i=1:length(t)
37     r(3)=r(3)+step;
38     factor = dot(r ,mbarN)*mcyIN+dot(r ,mcyIN)*mbarN+dot(mcyIN ,
39         mbarN)*r-5*dot(r ,mbarN)*dot(r ,mcyIN)*r/norm(r)^2;
40     force(i ,:) = 3*mu0*factor/(4*pi*norm(r)^5);
41     HbarN = (3*dot(rhat ,mbarN)*rhat -mbarN)/(4*pi*norm(r)^3);
42     BbarN = mu0*HbarN;
43     torque(i ,:) = cross(mcyIN ,BbarN);
44     force2(i ,:) = 3*mu0*dot(mbarN ,mcyIN)/(2*pi*norm(r)^4);
45     rst(i ,:)=r;
46
47 %% Figure printing:
48
49 figure
50 plot(rst(:,3),force(:,3),'b','MarkerSize',12)
51 xlabel('Distance (m)')
52 ylabel('Force (N)')
53 %title('Plot of Force related to distance')
54
55 figure
56 plot(rst(:,3),force2(:,3),'b','MarkerSize',12)
57 xlabel('Distance (m)')
58 ylabel('Force (N)')
59 %title('Plot of Force related to distance')
60
61 %% Vector iterative calculation:
62 for j=1:length(t)
63     r(1)=r(1)+step;
64     factor = dot(r ,mbarN)*mcyIN+dot(r ,mcyIN)*mbarN+dot(mcyIN ,
65         mbarN)*r-5*dot(r ,mbarN)*dot(r ,mcyIN)*r/norm(r)^2;
```

```

65     force(j+length(t), :) = 3*mu0*factor/(4*pi*norm(r)^5);
66     HbarN = (3*dot(rhat, mbarN)*rhat - mbarN)/(4*pi*norm(r)^3);
67     BbarN = mu0*HbarN;
68     torque(j+length(t), :) = norm(mcyIN)*norm(BbarN)*sin(55);
69
70     rst(j+length(t), :) = r;
71 end
72
73 figure
74 plot(rst(:,3), torque(:,3), 'g', 'MarkerSize', 10)
75 xlabel('Distance (m)')
76 ylabel('Torque (Nm)')
77 %title('Plot of torque related to distance')

```



```

38 p11(j)=i;
39 p12(j)=percentageBlack(i);
40
41 %%
42 i=70;
43 j=j+1;
44 I3 = imread('110-.png');
45
46 BW3 = imbinarize(I3);
47
48 percentageBlack(i)=(1-nnz(BW3)/numel(BW3))*100;
49
50 p11(j)=i;
51 p12(j)=percentageBlack(i);
52 %%
53 i=98;
54 j=j+1;
55 I4 = imread('138-.png');
56
57 BW4 = imbinarize(I4);
58
59 percentageBlack(i)=(1-nnz(BW4)/numel(BW4))*100;
60
61 p11(j)=i;
62 p12(j)=percentageBlack(i);
63 %% Photo with false percentage due to reflections
64 % Check original data for comparison
65 % i=104;
66 % j=j+1;
67 % I5 = imread('144-.png');
68 %
69 % BW5 = imbinarize(I5);
70 %
71 % percentageBlack(i)=(1-nnz(BW5)/numel(BW5))*100;
72 %
73 % p11(j)=i;
74 % p12(j)=percentageBlack(i);

```

```

75 %%
76 i=126;
77 j=j+1;
78 I6 = imread('206-.png');
79
80 BW6 = imbinarize(I6);
81
82 percentageBlack(i)=(1-nnz(BW6)/numel(BW6))*100;
83
84 p11(j)=i;
85 p12(j)=percentageBlack(i);
86 %% Photo with false percentage due to reflections
87 % Check original data for comparison
88 % i=132;
89 % j=j+1;
90 % I7 = imread('212-.png');
91 %
92 % BW7 = imbinarize(I7);
93 %
94 % percentageBlack(i)=(1-nnz(BW7)/numel(BW7))*100;
95 %
96 % p11(j)=i;
97 % p12(j)=percentageBlack(i);
98 %%
99 i=154;
100 j=j+1;
101 I8 = imread('234-.png');
102
103 BW8 = imbinarize(I8);
104
105 percentageBlack(i)=(1-nnz(BW8)/numel(BW8))*100;
106
107 p11(j)=i;
108 p12(j)=percentageBlack(i);
109 %% Photo with false percentage due to reflections
110 % Check original data for comparison
111 % i=162;

```

```

112 % j=j+1;
113 % I9 = imread('242-.png');
114 %
115 % BW9 = imbinarize(I9);
116 %
117 % percentageBlack(i)=(1-nnz(BW9)/numel(BW9))*100;
118 %
119 % pl1(j)=i;
120 % pl2(j)=percentageBlack(i);
121 %%
122 figure
123 scatter(pl1,pl2,50,'MarkerEdgeColor',[0 .2 .2],'MarkerFaceColor',
    ',[0 .3 .3]','LineWidth',1.5)
124 xlabel('Time (s)')
125 ylabel('Percentage of black pixels (%)')
126 title('Plot of percentage of black pixes due time')
127
128
129 % figure
130 % plot(pl1,pl2,'b','MarkerSize',12)
131 % xlabel('Time (s)')
132 % ylabel('Percentage of black pixels (%)')
133 % title('Plot of percentage of black pixes due time')
134
135 h = 4*10^(-3); % Rotating disc thickness in m
136 mass1 = 2.241*10^(-3); % Rotating disc mass in kg (2.241g)
137 massmag = 10*0.58*10^(-3);
138 mass = mass1 + massmag;
139 r = 30/2*10^(-3); % Rotating disc radius (m)
140 volume = pi*r^2*h; % Rotating disc volume in m^3
141 rho = mass/volume; % Density in kg/m^3
142
143 omega=300:10:700; % Angular velocity (rad/s)
144 sigma = omega.^2*r^2*rho/3; % Shear stress (N/m^2)
145
146 omegae=1030;
147 sigmae = omegae^2*r^2*rho/3;

```

```
148
149 figure
150 plot(omega, sigma, 'b', 'MarkerSize', 12)
151 xlabel('Angular velocity (rad/s)')
152 ylabel('Shear stress (N/m^2)')
153 % title('Shear stress with respect to angular velocity')
154
155 omegaav = 17.7395265; % Average angular velocity in rad/s
156 sigmaexp = omegaav^2*r^2*rho/3; % Shear stress based on average
    angular velocity
157 disp(sigmaexp);
```